Monthly Notices
of the
ROYAL ASTRONOMICAL SOCIETY

MNRAS **440,** 3140–3171 (2014) doi:10.1093/mnras/stu455

Multiple mean motion resonances in the HR 8799 planetary system

Krzysztof Goździewski★ and Cezary Migaszewski★

Centre for Astronomy, Faculty of Physics, Astronomy and Informatics, Nicolaus Copernicus University, Grudziadzka 5, PL-87-100 Toruń, Poland

Accepted 2014 March 4. Received 2014 February 25; in original form 2013 August 29

ABSTRACT

HR 8799 is a nearby star hosting at least four ∼10 $m_{\rm Jup}$ planets in wide orbits up to ∼70 au, detected through the direct, high-contrast infrared imaging. Large companions and debris discs reported interior to ∼10 au, and exterior to ∼100 au indicate massive protoplanetary disc in the past. The dynamical state of the HR 8799 system is not yet fully resolved, due to limited astrometric data covering tiny orbital arcs. We construct a new orbital model of the HR 8799 system, assuming rapid migration of the planets after their formation in wider orbits. We found that the HR 8799 planets are likely involved in double Laplace resonance, 1e:2d:4c:8b MMR. Quasi-circular planetary orbits are coplanar with the stellar equator and inclined by ∼25° to the sky plane. This best-fitting orbital configuration matches astrometry, debris disc models, and mass estimates from cooling models. The multiple mean motion resonance (MMR) is stable for the age of the star ∼160 Myr, for at least 1 Gyr unless significant perturbations to the *N*-body dynamics are present. We predict four configurations with the fifth hypothetical innermost planet HR 8799f in ∼9.7 au, or ∼7.5 au orbit, extending the MMR chain to triple Laplace resonance 1f:2e:4d:8c:16b MMR or to the 1f:3e:6d:12c:24b MMR, respectively. Our findings may establish strong boundary conditions for the system formation and its early history.

Key words: methods: numerical – astrometry – celestial mechanics – planetary systems.

1 INTRODUCTION

Numerous ground-based and space-based surveys of extrasolar planets brought thousands of new detections since the pioneering radial velocity (RV) observations (Walker 2012). Besides the RV method, the most successful observational techniques are transits, micro-lensing, eclipse timing, and direct imaging (Perryman 2011; Bhattacharjee & Clery 2013). The observations revealed a few hundreds of confirmed and well characterized extrasolar planets, exhibiting a rich diversity of orbital architectures, masses, densities, radii, as well as spectral types and evolutionary stages of single and binary parent stars (Howard 2013). Most of the extrasolar planets have been detected within a few astronomical units (au) of their host stars. Only the direct imaging brought a handful detections of massive planets beyond 10 au distance which roughly compares to the orbit of Saturn in the Solar system. This natural but extremely demanding observational technique is called the Holy Grail of exoplanet searching (Bhattacharjee & Clery 2013). The direct imaging may provide information on masses, radii, chemical composition, atmospheres, and orbital architecture (Oppenheimer et al. 2013) resulting in a complete characterization of extrasolar planetary systems. The main limitations are the angular resolution and contrast requirements, reaching more than 20 stellar magnitudes. Therefore, the prime targets are only massive, young and still self-radiating giant planets or brown dwarfs, in orbits beyond a few au of their host stars. A recent survey (Wahhaj 2013) of 57 debris disc stars shows at 95 per cent confidence that <13 per cent of these stars have a $>5m_{\rm Jup}$ planet beyond 80 au, and <21 per cent of debris disc stars have a $>3m_{\rm Jup}$ planet outside of 40 au. The HR 8799 (Marois et al. 2008, 2010) belongs to a rare sample of stars hosting planets discovered by the direct imaging (Konopacky et al. 2011). The HR 8799 system remains truly exceptional as the only *multiple* and dynamically compact configuration of four giant planets in ∼7–10 $m_{\rm Jup}$ mass range.

Since the discovery, the HR 8799 system receives an enormous attention. Tens of papers and proceedings are devoted to the age, companion masses, the orbital architecture of this system and its stability, debris discs, long-term evolution and formation (e.g. Goździewski & Migaszewski 2009; Reidemeister et al. 2009; Su et al. 2009; Fabrycky & Murray-Clay 2010; Marshall, Horner & Carter 2010; Moro-Martín et al. 2010; Bergfors et al. 2011; Currie et al. 2011, 2012; Soummer et al. 2011; Baines et al. 2012; Sudol & Haghighipour 2012; Esposito et al. 2013; Oppenheimer et al. 2013; Marleau & Cumming 2014; Matthews et al. 2014), to mention just a handful of these works. However, two questions seem still opened: what is the dynamical state of the HR 8799 system, and how this system has formed (Marois et al. 2010).

None of simple, analytic criteria of stability apply to the HR 8799 system. The early dynamical analyses (Goździewski &

★E-mail: k.gozdziewski@astri.umk.pl (KG); c.migaszewski@astri.umk.pl (CM)

Migaszewski 2009; Reidemeister et al. 2009; Fabrycky & Murray-Clay 2010) of the three-planet systems announced in the discovery paper (Marois et al. 2008) revealed that apparently circular, wide (∼100 au) orbits are separated by less than 3–4 mutual Hill radii. Such configuration must self-destruct statistically in 100 000 yr time-scale (Chambers, Wetherill & Boss 1996; Chatterjee et al. 2008) unless a protecting mechanism is present. Such a mechanism maintaining the stability for the star lifetime can be the mean motion resonance (MMR). Indeed, three outer planets hosted by the HR 8799 are most likely involved in stable Laplace 1d:2c:4b MMR (Goździewski & Migaszewski 2009; Reidemeister et al. 2009; Fabrycky & Murray-Clay 2010; Marshall et al. 2010; Soummer et al. 2011), similarly to innermost moons of Jupiter (Io, Europa and Callisto). (This is further confirmed in this paper). The orbits are low-eccentric, coplanar and inclined by ∼20°–30° to the sky plane. Companion masses are estimated in 5–7 $m_{\rm Jup}$ for planet b and in 7–10 $m_{\rm Jup}$ for planets c and d, in accord with evolution theories and cooling rates of sub-stellar objects (Baraffe et al. 2003). This early understanding of the HR 8799 system with three outer planets is roughly consistent across the literature.

However, after the discovery of the fourth planet (Marois et al. 2010), there is no unique nor certain orbital model that predicts long-term stable dynamical evolution anymore (Marois et al. 2010; Currie et al. 2011, 2012; Konopacky et al. 2011; Sudol & Haghighipour 2012; Esposito et al. 2013). This problem might be expected. The initial condition of the four-planet system involves almost 30 free parameters (osculating orbital elements and masses). The observational time window of ∼15 yr is very narrow as compared to the orbital periods between ∼50 and ∼500 yr, i.e. only ∼30 to ∼3 per cent of the innermost and outermost orbital arcs, respectively. A small number of ∼60 observations with significant uncertainties (∼1 per cent) results in the ratio of measurements per the degree of freedom close to 4. In contrast, to well characterize planetary orbits by the RV technique, this ratio should be 6–7, provided that data cover roughly 1–2 longest orbital periods. Any determination of the HR 8799 orbits by the common kinematic (Keplerian) or *N*-body (Newtonian) approaches is badly constrained. Actually, it is not clear, whether this young system is dynamically stable at all, and could be disrupted due to strong mutual interactions and dynamical chaos present (e.g., Goździewski & Migaszewski 2009; Sudol & Haghighipour 2012; Esposito et al. 2013).

The second unsolved problem regards close proximity of two inner planets to the parent star, interior to ∼25 au orbit. The present planet formation theories cannot explain creation of all four planets in situ by one mechanism (Marois et al. 2010). Because the spectral studies reveal similar sizes, chemical compounds and age of the planets (Marois et al. 2010), also the birth conditions of all planets likely have been similar. (See however the new results by Oppenheimer et al. 2013). Therefore, if all planets formed relatively far from the star, through gravitational fragmentation and/or the core accretion (see a discussion in Currie et al. 2011), they likely have been moved to their present orbits from wider orbits. This might be possible via the planet–planet scattering (Chatterjee et al. 2008) or the planetary migration. The planet–planet scattering might explain the marginal stability of the system reported in many papers. However, the *Spitzer* and *Herschel* observations (Chen et al. 2006; Su et al. 2009; Matthews et al. 2014) detected two coplanar, massive debris discs and an extended spherical halo around HR 8799. The inner warm disc reminds the asteroid belt, while the outer cold disc is similar to the Kuiper Belt in the Solar system. The presence of at least four giant planets and extended debris features are suggestive for a particularly massive protoplanetary disc. The presence of such a large disc might support and indicate the fragmentation formation and migration scenario. The migration could be rapid in such a presumably massive disc, in accord with estimates of the 100 au migration time-scale as short as 10^4 yr (Baruteau, Meru & Paardekooper 2011).

In this paper, we report a possible solution of both these problems, although focusing mainly on the orbital properties the HR 8799 system and its global dynamics. We derived a long-term stable *N*-body model of the HR 8799 system in accord with astrometric observations and companion mass estimates published to date. This self-consistent model relies on three basic assumptions, which actually reflect the results in the extensive literature: (i) the current HR 8788 planetary system emerged due to joint migration of four (or even more) massive planets that have been formed in wide orbits, (ii) the system is coplanar or almost coplanar, (iii) the system is long-term stable and the stability is maintained by the MMRs. These assumptions lead us to construct a new optimization algorithm for finding such configurations, which are strictly stable and fully consistent with astrometry and astrophysical mass constraints.

Our approach differs from common methods of modelling planetary systems by a crucial aspect. We assume that the orbital elements are *not free nor independent* parameters of the data model. Instead, the orbital elements are constrained by the dynamical evolution governed by planetary migration, hence the orbits are instantly coupled. This component of the optimization might be thought as a generalization of the self-consistent *N*-body fitting (Laughlin & Chambers 2001) constrained by the dynamical stability (e.g. Goździewski, Migaszewski & Musieliński 2008a; Goździewski & Migaszewski 2009) which imply a complex discretization of the parameter space. The method makes use of a heuristic model of migration (Moore & Quillen 2013) and theoretical estimates of the masses varied in prescribed, yet reasonable ranges derived on the grounds of recent cooling models, see the very recent paper by Marleau & Cumming (2014).

This paper is structured as follows. In Section 2, we present a short review of the recent literature devoted mostly to the orbital models of the HR 8799 system. Section 3 presents our new approach of the optimization of astrometric data through constraining it by the planetary migration. We call this method the Migration Constrained Optimization Algorithm (MCOA from hereafter). Section 4 regards the results and details of orbital architectures of the HR 8799 system derived with the MCOA. We re-analyse older data in (Marois et al. 2008) and early models including three outer planets b, c, d as well as the most recent and complete literature data set and the best-fitting four-planet model. A single-epoch characterization of three- and four-planet systems is discussed. We also consider ephemeris of the fifth, hypothetical planet interior to the innermost planet e. Section 5 regards important aspects of the stability analysis. Conclusions are given in Section 6. At the end, we provide a compilation of the observational data (Tables A1–A4) and our ephemeris of the four- and five-planet models (Tables B1–B5) discussed in Section 4.

2 LITERATURE MODELS OF THE HR 8799 SYSTEM

Shortly after the discovery, Fabrycky & Murray-Clay (2010) found that the stability of the three-planet system may be protected by the three-body Laplace 1d:2c:4b MMR. The system locked in this MMR could survive even if the planets have masses as large as ∼20 $m_{\rm Jup}$. Other solutions with large eccentricities and large mutual inclinations also were found. Goździewski & Migaszewski (2009) found very narrow stable zones in the phase space of the system

and a few extreme solutions, like the 1d:1c MMR between two inner planets. Reidemeister et al. (2009) concluded that all companions in the discovery paper (Marois et al. 2008) may be stable in the mass ranges of (5, 7, 7) $m_{\rm Jup}$, (7, 10, 10) $m_{\rm Jup}$ to (11, 13, 13) $m_{\rm Jup}$ provided that the Laplace resonance is present. They also found that the inclination of the orbital plane must be larger than $\sim 20^\circ$. Soummer et al. (2011) extended the observational window by ten years from the analysis of the *Hubble Space Telescope* (*HST*) images of the HR 8799. They confirmed that stable resonances (1d:1c MMR, 1d:2c MMR, or 1d:2c:4b MMR) found in the previous papers are still compatible with the extended astrometric data. They found stable Laplace resonance with low-eccentric orbit of planet d $e_{\rm d} \sim 0.1$ and moderate inclination of the system $\sim 28^\circ$ assuming coplanar configuration with circular orbits of the outermost planets. After releasing these constraints they could limit the inclination to ($27\overset{\circ}{.}3$–$31\overset{\circ}{.}4$) range and $e_{\rm d} < 0.46$. Currie et al. (2012) confirmed these results recently by estimating the inclination of HR 8799 d as $I_{\rm d} > 25^\circ$ and finding all eccentricities smaller than 0.18–0.3, with a strong indication of not face-on orbits. Bergfors et al. (2011) observed the system with NACO and VLT. They found that planet HR 8799 d is inclined with respect to the line of sight, suggesting that its orbit is slightly eccentric or non-coplanar with the outer planets and debris disc.

The very recent works devoted to the dynamical analysis of the four-planet system including HR 8799 e bring sometimes mutually contradicting conclusions. Marois et al. (2010) revisited the stability analysis in (Fabrycky & Murray-Clay 2010). By varying parameters of planet e in the four-planet system with single 1d:2c MMR or double 1d:2c:4b MMR, they found a few solutions surviving 160 Myr in samples of 100 000 trial models, regarding masses in the range of 30 Myr (5,7,7,7) $m_{\rm Jup}$ and 60 Myr (7,10,10,10) $m_{\rm Jup}$ for planets b, c, d, and e, respectively. Semimajor axis of planet e has been changed between 12.5 and 14.5 au. Stability analysis in Marois et al. (2010) suggest a younger age and lower planet masses. Konopacky et al. (2011) determined eccentricity limits to less than 0.4 for all planets. They found that the addition of the fourth planet makes it very difficult to find any stable configuration for masses greater than 7 $m_{\rm Jup}$, also suggesting lower masses in a younger system ($\sim$30 Myr). Currie et al. (2011) combined the results from planet evolution models and the stability analysis to limit the masses of planets HR 8799 b, c, d, e to the ranges of 6–7 $m_{\rm Jup}$, 7–10 $m_{\rm Jup}$, 7–10 $m_{\rm Jup}$, and 7–10 $m_{\rm Jup}$, respectively. Esposito et al. (2013) show that planet e cannot form the 1e:2d:4c MMR if its orbit is circular and coplanar with planets d and c, while such orbits are allowed for the 2e:5d MMR. They found significant stable regions for masses in the 5 $m_{\rm Jup}$ range, below the current estimates based on the stellar age of 30 Myr and astrophysical models of cooling sub-stellar objects. Sudol & Haghighipour (2012) found the system marginally stable, surviving less than $\sim$5 Myr at inclinations in the range of $\sim 10^\circ$ and $\sim$31 Myr at larger inclinations $\sim 30^\circ$. The most stable systems also favour planet e closer to the star than is observed. They conclude that the planetary masses must be less than 7–10–10–10 $m_{\rm Jup}$ and the system is young. Planets b and c could be in eccentric or mutually inclined orbits with respect to planet d.

Baines et al. (2012) estimate HR 8799 mass $\sim 1.51\,{\rm M}_\odot$ and two ages $\sim$30 and $\sim$90 Myr, depending on the evolutionary track contracting towards the zero-age main sequence or expanding from it. These estimates of the HR 8799 age suggest that the companions are indeed planets. The very recent work of Oppenheimer et al. (2013) brings different spectra of the planets suggesting a greater diversity of these objects than previously found. The *Spitzer* and *Herschel* infrared spectra were used to resolve two coplanar debris belts (Chen et al. 2006; Reidemeister et al. 2009; Su et al. 2009; Hughes et al. 2011; Patience et al. 2011; Matthews et al. 2014) divided by the radial gap between $\sim$15–90 au, and an extended dust halo surrounding the whole system. Patience et al. (2011) measured the first spatially resolved map of the HR 8799 disc at 350 μm and detected an arc of emission with a bright clump at a distance consistent with simulations of dust trapped in a 1b:2 MMR with the outermost planet. This result is suggestive for the planets migrated to their current locations and that the eccentricity is low, if the dust is trapped in a resonance (Patience et al. 2011). Su et al. (2009) and Hinkley et al. (2011) report a dust-free hole interior to $\sim$6 au in the inner warm belt. Assuming an age of 30 Myr and adopting the Baraffe et al. (2003) evolutionary models, Hinkley et al. (2011) determined upper limit of a companion mass of 80, 60, and 11 $m_{\rm Jup}$ at projected orbital separations of 0.8 au, 1 au, and 3–10 au, respectively, ruling out a brown dwarf or a small star between 0.8 and 10 au.

3 OPTIMIZATION CONSTRAINED BY MIGRATION

A stable low-order MMR in mutually interacting planetary system is a dynamical state forcing only certain, somehow discrete configurations of the planets. This might be understood and visualized as narrow islands of stable motions in the orbital and physical parameter space (e.g. Goździewski et al. 2008a; Goździewski & Migaszewski 2009). A particular multiple MMR determines orbital periods (and semimajor axes); stability constraints permit only certain ranges of eccentricities; the relative orbital phases are limited by a critical argument of the MMR. Therefore, the best-fitting orbital elements are *not free nor independent* parameters of the data model. The orbital elements must be constrained by the dynamical evolution governed by planetary migration and orbits are instantly coupled. Planets migrate as a whole dissipative dynamical system that synchronizes itself to a certain state (MMR) which is a kind of an equilibrium in the phase space. We then search for those 'equilibria' which fit the observations at some epoch. A crucial aspect of a practical realization of this idea is that a heuristic rather than fully realistic model of the planetary migration (Moore & Quillen 2013) is required to establish a chain of multiple, low-order MMRs. The coupled migration component serves as a kind of implicit constraint of the optimization process. The hard part of this task is that we not know a priori which initial parameters (masses, initial orbits, migration rates) lead to the best-fitting or acceptable configuration.

3.1 A heuristic model of planetary migration

Mechanisms of MMRs formation are widely studied as the result of the planetary migration (see a review by Papaloizou & Terquem 2006, and references therein). Planetary migration is a sophisticated physical process depending subtly on many parameters. Here, we use a simplistic, heuristic two-dimensional model of the migration in Moore & Quillen (2013). In this model, the migration is driven by the drag force in the form of

$$\boldsymbol{F} = -\frac{\boldsymbol{v}}{2\,\tau_{\rm a}} - \frac{\boldsymbol{v}-\boldsymbol{v}_{\rm c}}{\tau_{\rm e}}, \qquad (1)$$

where $\boldsymbol{v}$ is an astrocentric velocity of a planet, $\boldsymbol{v}_{\rm c}$ is the Keplerian velocity of this planet in a circular orbit at a given radius, $\tau_{\rm a}$ and $\tau_{\rm e}$ are the migration and circularization rates of orbits, respectively.

After Moore & Quillen (2013), we assume that $\tau_e = K\tau_a$, where K is a constant between 1 and 100. We assume that τ_a is a function of astrocentric distance r of the planet and time, i.e.

$$\frac{1}{\tau_a} = \frac{1}{\tau_1} + \frac{1}{\tau_2}, \quad \tau_1 = \tau_{1,0}\, r^{\alpha_1}\, \exp(t/T_1), \quad \tau_2 = \tau_{2,0}\, r^{\alpha_2}\, \exp(t/T_2), \tag{2}$$

where α_i, τ_i, and T_i ($i = 1, 2$) are constant factors in wide ranges, i.e. $\tau_{i,0} \in [10^6, 10^8]$ yr, $T_i \in [10^6, 10^8]$ yr, $\alpha_1 \in [-2.0, -0.1]$, $\alpha_2 \in [0.1, 2.0]$. These ranges are sufficient to encompass different types of migration, both convergent and divergent. The first term, with $\alpha_1 < 0$, leads to the convergent migration, while the second term with $\alpha_2 > 0$ accounts for the divergent migration. For $\alpha_1 < -1.0$, the period ratios of pairs of subsequent planets P_{i+1}/P_i (where $P_{i+1} > P_i$) decrease in time, while for $\alpha_1 > -1.0$ the period ratios increase.

The migration resulting from such wide ranges of the parameters may occur on very different time-scales. For instance, for the convergent term, $\alpha_1 = -1.3$ and $\tau_{1,0} = 10^8$ yr, $\tau_1 \approx 0.4$ Myr and $r = 70$ au, which is consistent with the time-scale implied by the type II migration (e.g. Kratter, Murray-Clay & Youdin 2010).

To establish the orbital architecture of a studied system, there is no need to resolve all details of physical processes forcing the migration. We found that the heuristic model is sufficient for the optimization. Although permitted ranges of the migration parameters may seem unreasonably wide, we do not narrow these ranges to avoid too strict assumptions on the time-scales, for instance, on their dependences on r.

3.2 Optimization and migration algorithm in the real world

3.2.1 Parametrization and initial conditions

To initiate a single migration track of the HR 8977 planetary system, we choose at random initial, circular orbits (semimajor axes), planetary masses and the migration parameters. An initial semimajor axis of an nth planet increases exponentially in accord with $a_n = a_1 \exp[\beta(n-1)]$, where $\beta \in [0.2, 1.8]$. Orbital longitudes of the planets are chosen from the $[0^\circ, 360^\circ]$ range. Masses of the planets are constrained through astrophysical cooling models. For instance, Marois et al. (2008) found $m_e = (9 \pm 4)\, m_{\rm Jup}$, $m_d = (10 \pm 3)\, m_{\rm Jup}$, $m_c = (10 \pm 3)\, m_{\rm Jup}$, $m_b = 7^{+3}_{-2}\, m_{\rm Jup}$. The mass estimates depend on the star age, which is a matter of ongoing debate. Ages among 30, 60, 90, 160, and even 1 Gyr are quoted (Baines et al. 2012; Oppenheimer et al. 2013). Because our dynamical model provide independent mass constraints, we considered a relatively smooth mass ranges, roughly within the range [2,13] $m_{\rm Jup}$ for all planets, up to $\sim$20 $m_{\rm Jup}$ in a few experiments. We integrate the N-body equations of motion with the dissipative term (equation 1) added to the right-hand sides, until the migrating system becomes so compact that the orbits cannot be consistent with the observations anymore.

In this way, a given initial condition determines an evolutionary track of the system. The problem is to find the best-fitting parameters ($t_{\rm obs}$, I, Ω, $\omega_{\rm rot}$), where $t_{\rm obs}$ is an arbitrary time interval counted from the beginning of the migration and (Ω, I, $\omega_{\rm rot}$) are 3–1–3 Euler angles. The best-fitting epoch $t_{\rm obs}$ is a particular moment during the migration that corresponds to correct – possibly optimal – sizes of the orbits and relative orbital phases of the planets at these orbits. Three relevant Euler angles (Ω, I, $\omega_{\rm rot}$) are required to describe the orientation of an arbitrary orbital frame w.r.t the sky plane (the observer's frame). This orientation is parametrized naturally through classic 3–1–3 sequence of rotations: I is the inclination of the orbital plane, Ω is the longitude of ascending node, and $\omega_{\rm rot}$ is an angle measured in the orbital plane. We search for systems evolving in such a manner that being observed in a certain epoch from a certain direction, they look like the current HR 8799 system. Such particular epoch and orientation of the orbital frame together with the migration model and its parameters determine the current orbital architecture of the system. Obviously, the migration model, equations (1) and (2), is simplistic and very similar final configurations may be obtained when starting from different initial states. However, we stress that we do not aim to answer the question: *How the HR 8799 looked like at the early stages of its evolution?*. We focus entirely on its observed, geometrical architecture, and present astrometry.

Searching for the best-fitting solutions in a whole possible range of $t_{\rm obs}$ would be unreasonably time and CPU consuming. The actual optimization of the measurements (searching for the minimum of $\sqrt{\chi^2_\nu}$) begins when the migrating system looks roughly similar to the HR 8799. This happens when the semimajor axes of four/five-planet system are confined to the following ranges: $a_e \in [12, 17]$ au, $a_d \in [23, 29]$ au, $a_c \in [37, 48]$ au, $a_b \in [62, 75]$ au, and $a_f \in [5, 12]$ au, respectively. (Note that we also consider five-planet systems with a hypothetical, yet undetected planet HR 8799 f, see Section 4.)

To illustrate these ideas, the left-hand panel of Fig. 1 shows an evolution of an example configuration. The top panel is for the evolution of semimajor axes. The system migrates inwards in relatively short time-scale of the order of 10^5 yr. The time axis of (a_i, t) – graphs ends at a moment at which a_i for all planets reach the upper limits of semimajor axes quoted in the previous paragraph.

The middle left-hand panel in Fig. 1 shows the evolution of the periods ratios of pairs of subsequent planets. The red colour is for P_d/P_e, green colour marks P_c/P_d, while blue colour is for P_b/P_c. Initial periods ratios are $\sim$3, $\sim$5, and $\sim$2 for subsequent pairs of the planets. After a few of 10^4 yr, all subsequent pairs of planets are already locked in 2: 1 MMRs. For each pair of subsequent planets, one of the two-planet critical resonant arguments,

$$\theta_{1:2} = \lambda_1 - 2\,\lambda_2 + \omega_i, \quad i = 1, 2,$$

where $\lambda_{1,2}$ and $\omega_{1,2}$ are the mean longitudes and pericentre arguments, is already librating around 0°. However, the system evolves chaotically and the four-body resonant argument circulates in the whole permitted range of $[-180^\circ, +180^\circ]$. The four-body critical resonant argument is a generalization of the Laplace resonant argument, i.e. $\theta_{1:2:4} \equiv \lambda_1 - 3\,\lambda_2 + 2\,\lambda_3$, where the mean longitudes λ_i, $i = 1, 2, 3$, are ordered from the innermost to the outermost planet. For the three-planet Laplace 1d:2c:4b MMR, there is only one combination of the longitudes forming the critical resonant argument. For a four-planet 1e:2d:4c:8b MMR (actually, this is the most likely orbital configuration of the HR 8799 system found in this paper), there are more critical arguments possible. We chose the following critical argument:

$$\theta_{1:2:4:8} = \lambda_1 - 2\,\lambda_2 - \lambda_3 + 2\,\lambda_4 \equiv \lambda_e - 2\,\lambda_d - \lambda_c + 2\,\lambda_b,$$

which librates around 0° in the four-planet configurations of the HR 8799 system. The bottom left-hand panel of Fig. 1 shows the time evolution of the critical resonance $\theta_{1:2:4:8}$ for some time of typical migration run.

3.2.2 Fine tuning of the migration rates

The orbital evolution of a planetary system occurs in three different time-scales. The shortest time-scale is related to the orbital periods.

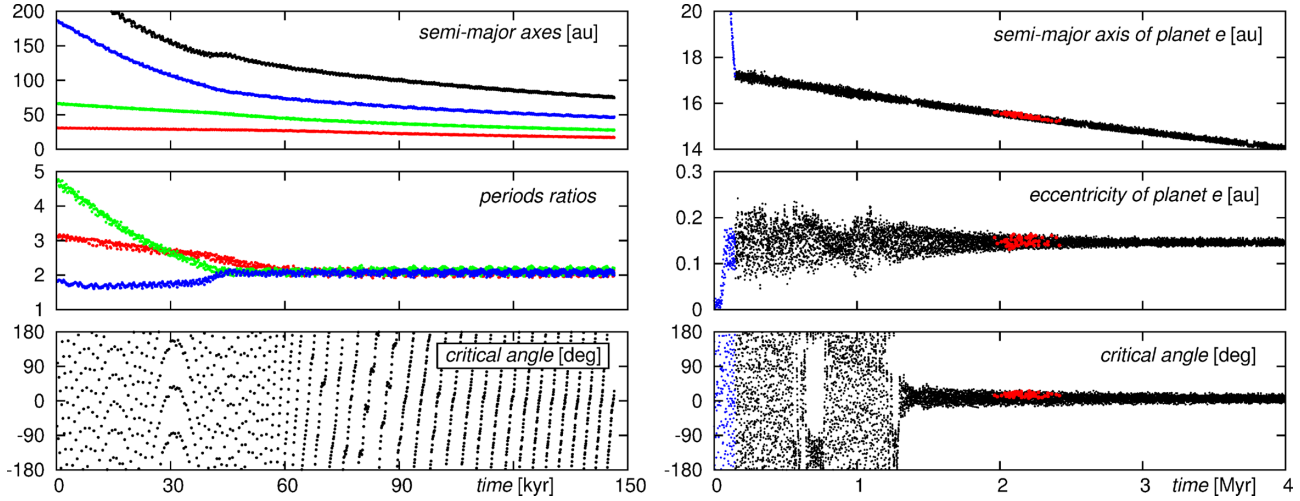

Figure 1. Temporal evolution of a four-planet system and trapping the system into 1e:2d:4c:8b MMR. *Left-hand panel:* evolution of the semimajor axes a_i (i = b, c, d, e), periods ratios and the critical angle of the double Laplace MMR in a fast migration regime. *Right-hand panel:* evolution of a_e, e_e and the critical angle $\theta_{1:2:4:8}$ in a slow migration regime. Red symbols mark orbits well fitting the observations (formal $\sqrt{\chi^2_\nu} < 2$).

The intermediate time-scale is related to the long-term conservative evolution of the system (rotations of periastrons, secular, and resonant modulations of the eccentricities). The longest time-scale corresponds to the migration.

After the system reaches a reasonably accurate configuration, the migration coefficients are changed to slow down the migration substantially. This is being done mostly for technical reasons, to avoid overlooking a proper configuration possibly well with the

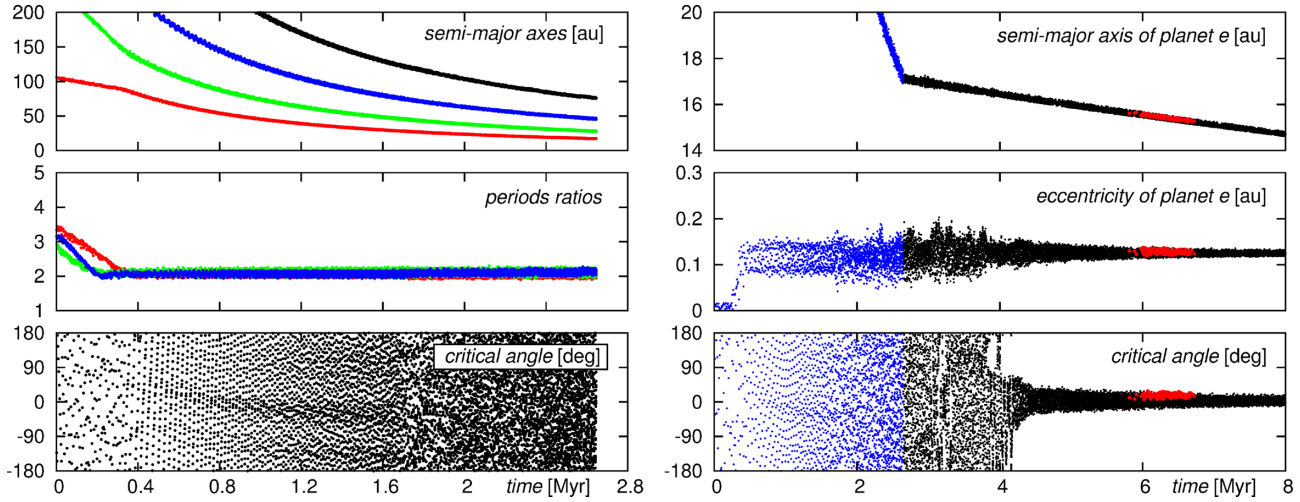

Figure 2. Same as on Fig. 1 but for different initial orbits and evolution parameters (initial conditions).

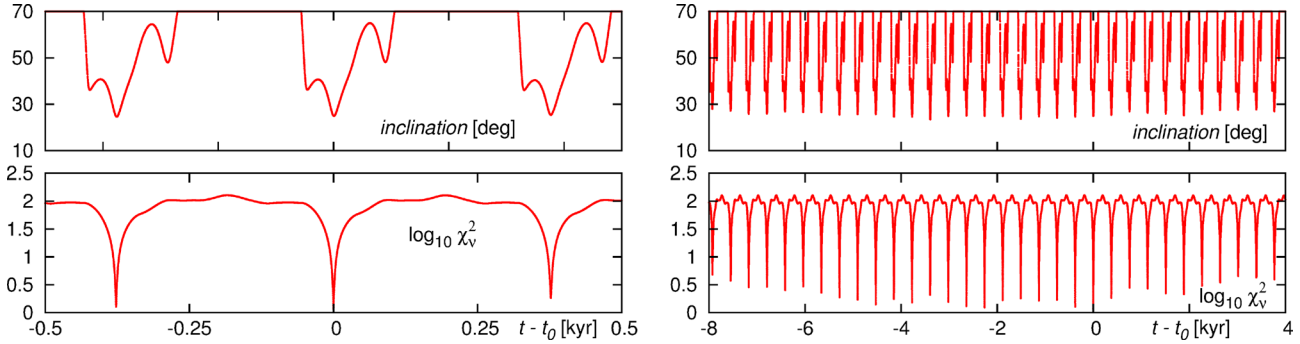

Figure 3. Illustration of the optimization algorithm constrained by planetary migration. Evolution of the best-fitting inclination (*top*) and $\sqrt{\chi^2_\nu}$ (*bottom*) in time around the best-fitting solution.

observations. If the resonant system is observed at certain epoch, its osculating Keplerian elements (semimajor axes, eccentricities, arguments of pericentres, mean longitudes) take some particular values. A configuration which fits the observations consists of appropriate shapes of the orbits, their orientations as well as orbital phases. Due to the MMR lock implying quasi-periodic conjunctions of the planets, such particular quasi-periodic, *relative* orbital setup repeats in space. This repetition may take quite a long time interval. In such a case, too fast migration during the repetition interval may tight the orbits too much and we can skip a correct, optimal configuration. At some instant the planets may be phased correctly by the MMR lock but their orbits are still *too extended* to fit the observations. However, after the next repetition period, appropriate orbital phases might appear when the migrating system is already *too compact* to fit the data. A slower migration increases a chance of fixing proper orbital phases simultaneously with other orbital elements of the planets.

A slow enough migration is crucial because it helps to lock the system into the multiple-body MMR. But the migration cannot be also *too slow* or arbitrarily slow. At the initial stages of migration, the system is strongly chaotic (see Fig. 1) until the four-planet MMR lock appears and the whole system may be 'missed' at all due to a self-disruption. The resonance locking should then occur in a time-scale shorter than a characteristic instability time-scale. An optimal migration rate was chosen after a number of numerical experiments. We must underline that the multiple-body MMRs trapping does not occur always and 'easily'. The MCOA requires much care and a fine tuning in this respect.

The MCOA may be further simplified and optimized for CPU resources. Once the orbital phases and eccentricities are constrained through a resonance, the migration causes the semimajor axes decay. Because the *N*-body dynamics are essentially scale-free, the scale of the system may be a free (fifth) geometrical parameter of the model. We did not explore this approach in this paper, but likely that makes the MCOA run more quickly and find better fits to the observations. (Credits of this improvement go to the reviewer).

3.2.3 *Example evolutionary tracks of migrating systems*

These thoughts and the results of accompanying experiments are illustrated in Fig. 1. The right-hand panels of this figure present the orbital evolution during a slow migration. Subsequent panels, from the top to the bottom are for graphs of $a_e(t)$, $e_e(t)$, and $\theta_{1:2:4:8}(t)$, respectively. The migration rate for planet e is less than $\sim$1 au Myr^{-1}. After $\sim$1 Myr, the systems locks into exact 1e:2d:4c:8b MMR. Amplitudes of eccentricities $e_e(t)$ and critical angle $\theta_{1:2:4:8}$ steadily decrease. After $\sim$2 Myr the simulated configuration looks like the actually observed HR 8799 system. Middle parts of the elements graphs are marked in red indicating reasonably good solutions that provide $\sqrt{\chi^2_\nu} < 2$.

This simulation concerns the actual evolution of the best-fitting four-planet model IVa, which is found rigorously stable (see

Table 1. Orbital osculating elements of the best-fitting solution IVa at the epoch 1998.83. The stellar mass $m_0 = 1.56\,M_\odot$. Note that due to the geometry the Ω angle may take two values that differ by 180°, however the *pericentre longitude* ϖ is preserved after the rotation of the nodal line by 180°.

	$m\,(m_{\rm Jup})$	a (au)	e	I (deg)	Ω (deg)	ϖ (deg)	$\mathcal{M}$ (deg)
HR 8799 e	9 ± 2	15.4 ± 0.2	0.13 ± 0.03			176 ± 6	326 ± 5
HR 8799 d	9 ± 3	25.4 ± 0.3	0.12 ± 0.02	25 ± 3	64 ± 3	91 ± 3	58 ± 3
HR 8799 c	9 ± 3	39.4 ± 0.3	0.05 ± 0.02		(244 ± 3)	151 ± 6	148 ± 6
HR 8799 b	7 ± 2	69.1 ± 0.2	0.020 ± 0.003			95 ± 10	321 ± 10

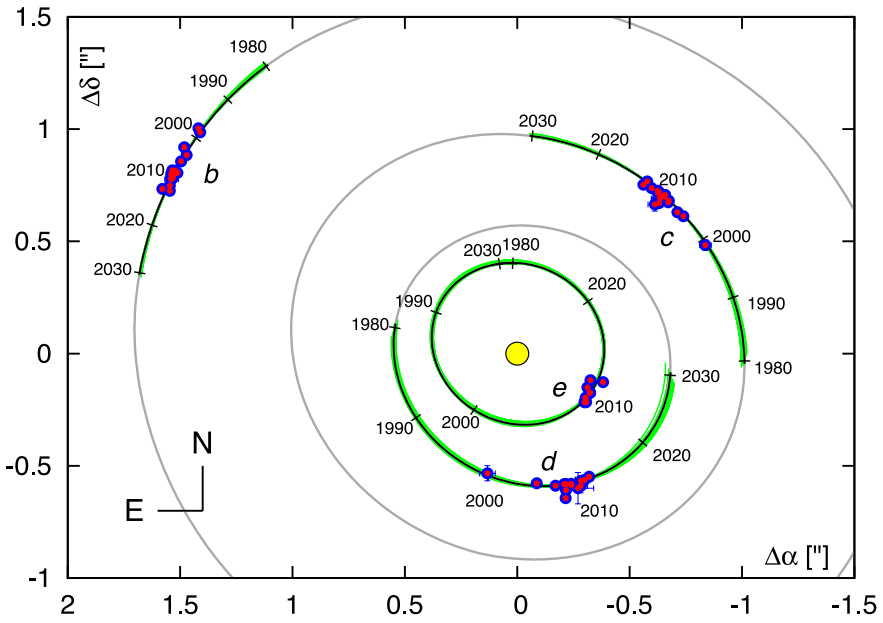

Figure 4. Relative astrometric positions of the planets (red filled circles), orbital arcs for the best-fitting model IVa (black curves), and stable solutions within the 3σ confidence level of the best-fitting model (green curves).

Section 4). However, even very similar configurations can be obtained from quite different initial systems. Indeed, the next Fig. 2 shows the results for a solution with marginally worse $\sqrt{\chi^2_\nu}$. In this case the initial orbits are much more extended. A desired trapping into the 1e:2d:4c:8b MMR takes place ∼2 Myr before the system migrates into the observed configuration.

Fig. 3 presents one-dimensional scans of temporarily best-fitting inclination I and an instant $\sqrt{\chi^2_\nu}$ as functions of $t_{\rm obs}$ during the stage of slow migration. These data are found for the best-fitting configuration with $\sqrt{\chi^2_\nu} \approx 1.15$ and $I \approx 25^\circ$. After each period of ∼400 yr, which is actually the orbital period of planet b, $\sqrt{\chi^2_\nu}$ possesses minima of varying depth. Although the planets have orbital phases close to best-fitting values, other osculating elements might be still not optimal; hence, we should examine a time sequence of such local minima of $\sqrt{\chi^2_\nu}$ to find the best model. If the orbital phases are distinct from their observed values, the temporal best-fitting inclination and the two remaining orientation angles do not take any reasonable values.

3.2.4 *Non-standard features and limitations of the MCOA*

It might be surprising that the MCOA is supposed to constrain much more parameters than the number of observations. We underline here that only four parameters of the migration model are free: three Euler angles describing orientation of the orbital frame w.r.t. the observer frame and the osculating epoch. All remaining orbital elements are self-constrained by the common migration and trapping the planets in a multiple MMR.

By the design and assumptions, our approach can be useful for predicting positions of planets in multiple systems when only a few observational epochs are available (see Section 4). The MCOA might also help to verify if putative candidates are bounded to the star. In principle, the minimal number of required parameters (four) is equal to the number of data provided by two astrometric measurements of two companions. This may be provided by single-epoch detection of two massive, spatially close planets or sub-stellar objects which are presumably involved in a low-order MMR (Section 4).

The MCOA will almost certainly fail if planetary masses are small, and non-resonant configurations are possible. However, we consider here a particular class of planetary systems whose parameters are biased through natural limits of the direct imaging. The MCOA may successfully model such systems by making use of their essential physical and orbital characteristics.

A complete modelling of four- or five-planet HR 8799 configurations involves the optimization and stability analysis, and requires significant computational resources. For this work, we needed roughly ∼100 CPU cores for 2–3 weeks, to sample densely the space of the initial parameters and evolutionary tracks, and to gather possibly large statistics of the best-fitting models. The maximal Lyapunov characteristic exponent (MLCE) criterion (Cincotta & Simó 2000; Cincotta, Giordano & Simó 2003) and direct numerical integrations were used to verify stable models and to reconstruct the MMRs structures (see Section 5 for details). This step of dynamical post-analysis of the best-fitting models is also CPU intensive. We estimate its cost for ∼1000 CPU cores for 2–3 weeks.

4 ARCHITECTURES OF THE HR 8799 SYSTEM

To recover likely and dynamically stable models of the HR 8799 system, we consider a few orbital architectures as well as five distinct sets of observations (see Tables A1–A4). Data set D1 comprises of all astrometric measurements published till 2013 August. This data set *diminished* by observations of planet e is called data set D5. We analyse also data set D2 that consists of astrometric measurements published in the discovery paper (Marois et al. 2008). Data sets D3 and D4 mimic single-image detection of three and four planets. These sets consist of only three and four most accurate single-epoch measurements, selected from the discovery paper (Marois et al. 2008; data set D3, epoch 2008.61) and from a more recent work by Currie et al. (2011; data set D4, epoch 2009.77).

We optimized a few combinations of orbital architectures labelled with Roman numbers III (three planets), IV (four planets), and V (five planets) with data sets D1–D5. In all optimization models, we assumed that masses of the planets are bounded to ∼[2, 13] $m_{\rm Jup}$ range, roughly within limits determined in Marois et al. (2008, 2010), yet in a few experiments we tested also masses up to ∼20 $m_{\rm Jup}$ limit. The masses were randomly varied within these bounds in each single run. The mass of the parent star was fixed to 1.56 solar mass (Marois et al. 2010), very close to the most recent estimate (Baines et al. 2012). The optimization algorithm was run at least $\sim 10^4$–10^5 times for each data set-model combination. Each single run was initiated from random initial orbits and migration parameters (equation 1) which were set in wide, yet reasonable and carefully tested ranges. As the result, we gather a set of initial conditions representing the best-fitting orbital parameters. We consider all solutions within 3σ and 6σ confidence interval of a given, best-fitting *stable* model.

Finally, we investigated the orbital stability of all 6σ models through direct, long-term N-body integrations up to the upper limit of the system age (160 Myr); yet we did a few experiments for 500 Myr and 1 Gyr intervals (Section 5). The results of the

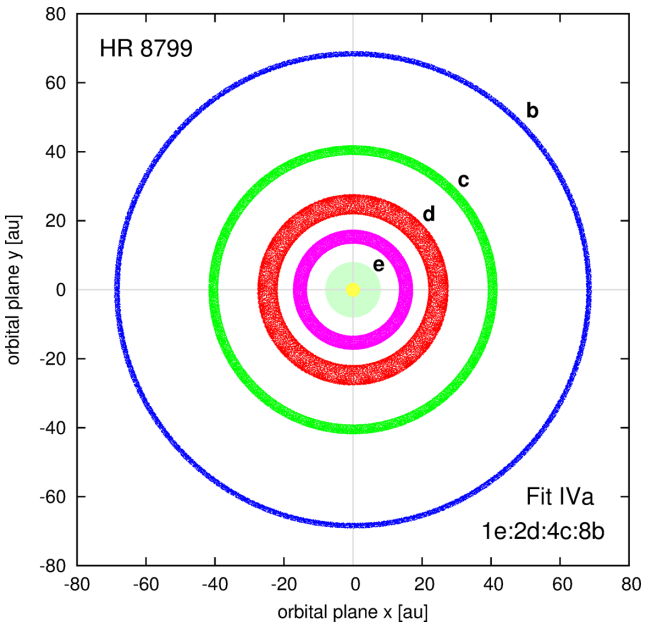

Figure 5. Orbital architecture of the HR 8799 system in accord with the best-fitting four-planet model IVa (Table 1). Temporal positions of HR 8799 planets are shown for 160 Myr in the astrocentric coordinate frame, coplanar with the orbits. The inner shaded circle in the centre has an approximate radius of the last stable orbit of a mass-less particle perturbed by the giant planets. This might correspond to the inner warm disc investigated in a number of papers (e.g. Reidemeister et al. 2009; Su et al. 2009; Moro-Martín et al. 2010; Hinkley et al. 2011).

long-term integrations are interpreted through the event time T_E – an interval of crossing orbits or an ejection of a planet from the system. We also reconstructed the local structure of the phase space (resonances widths) by computing the maximal Lyapunov exponent expressed through the fast indicator MEGNO (Mean Exponential Growth factor of Nearby Orbit; Cincotta et al. 2003). The dynamical maps in selected orbital parameter planes were computed in resolutions up to 720 × 360. All details of the stability experiments and regarding a time-calibration of the fast indicator are given in Section 5.

4.1 The nominal model IVa: four planets, data set D1

Model IVa combines four-planet, coplanar system and data set D1 comprising of all available observations in the literature. The osculating astrocentric Keplerian elements together with their uncertainties are given in Table 1. This model provides $\sqrt{\chi^2_\nu} \approx 1.15$. We did not find any other four-planet configuration consistent equally well with the observations. Fig. 4 shows the best-fitting orbits overplotted on to the sky plane together with the observations. The green curves show very small deviations between all stable orbits in the derived statistics within 3σ confidence level of the best-fitting model. Table B1 displays the (E, N) ephemeris between epochs 1995.0 and 2020.0. Temporal evolution of all orbits for 160 Myr is shown in Fig. 5. This best-fitting, stable, and unique orbital configuration consistent with all astrometric data corresponds to *exact* first-order MMR, double Laplace resonance 1e:2d:4c:8b MMR. The ratios of the orbital periods for subsequent pairs of planets are very close to 2. This might be the first report of such *long-term stable* MMR in the literature, although this type of solution was already investigated (Esposito et al. 2013).

The inclination of coplanar orbits to the sky plane is well constrained $I \approx 25^\circ \pm 3^\circ$. Statistical analysis of the rotational speed of A5 stars imply the inclination ∼23 deg of the HR 8799 equator to the sky plane (Kaye & Strassmeier 1998; Royer, Zorec & Gómez 2007; Wright et al. 2011). In a very recent study of the *Herschel* far-infrared and submilimetre observations of the outer debris disc, Matthews et al. (2014) measured its inclination to $26^\circ \pm 3^\circ$ from face-on and position angle of 64° E of N, closely matching parameters of our model IVa. These results, derived independently on astrometry and on different data and observations, are very suggestive for the planetary system perfectly coplanar with the stellar equator and remnants of the protoplanetary disc.

An extensive stability study reveals that the best-fitting four-planet configuration is strictly quasi-periodic, with the maximal Lyapunov exponent equal to 0. The direct numerical integrations do not show any sign of instability up to 1 Gyr (for details see Section 5). The system is locked deeply in a four-body Laplace MMR. The critical argument $\theta_{1:2:4:8} \equiv \lambda_e - 2\lambda_d - \lambda_c + 2\lambda_b$ librates around 0° with a semi-amplitude less than 20°. The resonance width across the semimajor axes is between 2 au for planet b and ∼0.3 au for the innermost planet e.

Fig. 6 shows the (E, N) sky coordinates determined by the dynamically derived best-fitting solution IVa (black solid curves), as

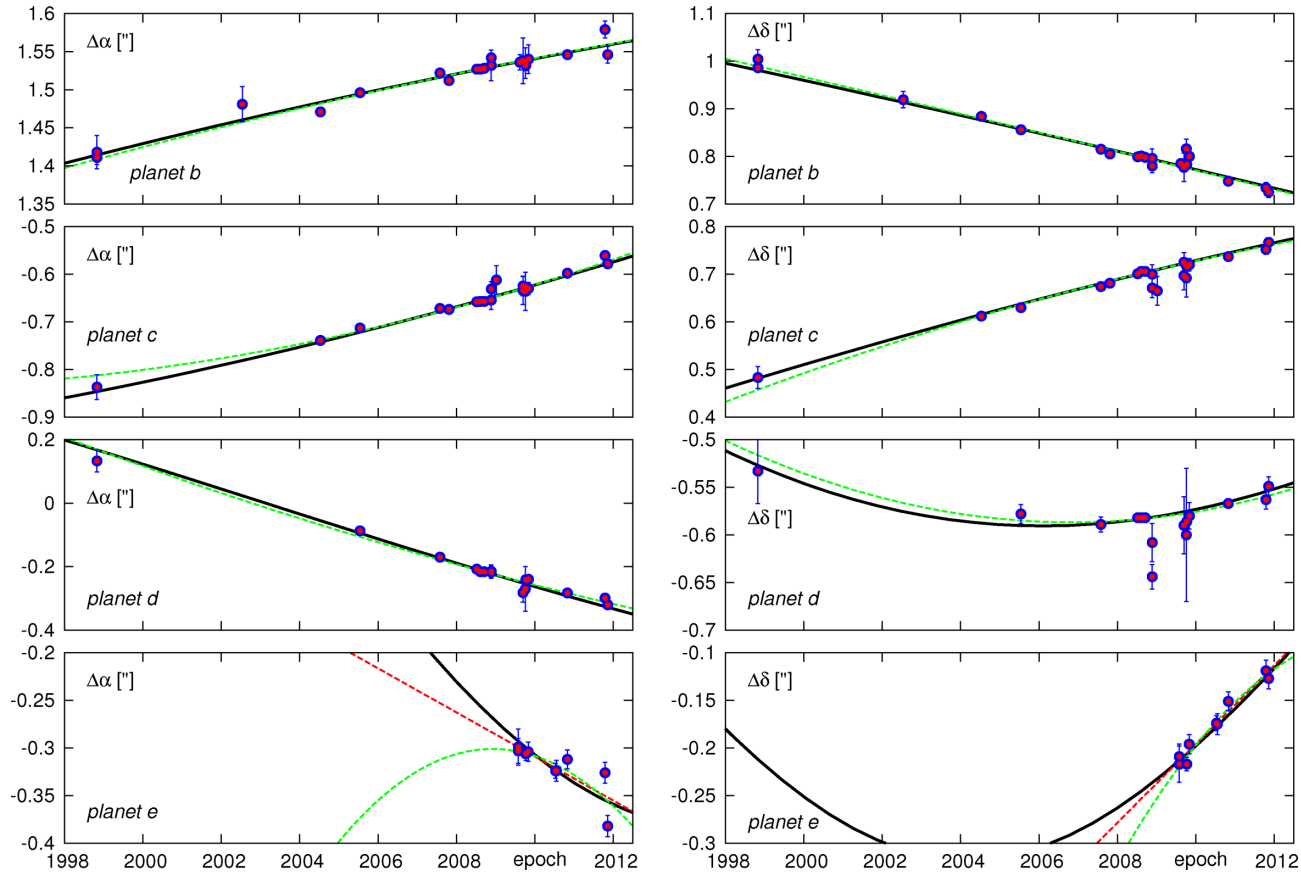

Figure 6. Astrocentric, astrometric sky-plane coordinates $x \equiv \Delta\alpha$ [arcsec] (*left-hand panel*) and $y \equiv \Delta\delta$ [arcsec] (*right-hand panel*) for subsequent planets (red filled circles), and orbital arcs for the best-fitting model IVa (black curves). Dashed curves are for best-fitting quadratic and linear Gibbs series expansion to the measurements (data set D1), respectively.

$x(t) \equiv \Delta\alpha(t)$ and $y(t) \equiv \Delta\delta(t)$, respectively, versus observation epoch t overplotted with data points. Green dashed curves are for the best-fitting quadratic functions of $x(t)$ and $y(t)$, respectively. The number of measurements seems too small to constrain the parabolic model for planet HR 8799 e. The dispersion of data is large, hence we also computed the best-fitting linear model (red dashed lines).

Best-fitting parameters of the linear and parabolic models of the sky coordinates express Keplerian (kinematic) approximations of the astrocentric radius $\boldsymbol{r}(t)$ and orbital velocity $\boldsymbol{v}(t)$ of each planet. These parameters are the first- and second-order terms of the Gibbs series (f, g, $\dot{f}$, $\dot{g}$) in the well-known formulae

$$\boldsymbol{r}(t) = f\boldsymbol{r}_0 + g\boldsymbol{v}_0, \quad \boldsymbol{v}(t) = \dot{f}\boldsymbol{r}_0 + \dot{g}\boldsymbol{v}_0,$$

where $\boldsymbol{r}_0 \equiv \boldsymbol{r}(t_0)$, $\boldsymbol{v}_0 \equiv \boldsymbol{v}(t_0)$ is the initial condition at epoch t_0. The linear model was used in previous works to bound the space of permitted orbital elements (e.g. Goździewski & Migaszewski 2009; Reidemeister et al. 2009; Fabrycky & Murray-Clay 2010). Due to narrow observational window this space is huge and the orbits are kinematically unconstrained. A comparison of the dynamical best-fitting solution IVa found in this work with the linear and parabolic approximations of the data (Fig. 6) shows that this *rigorously stable* initial condition closely matches the kinematic (or geometric) description of the measurements. Moreover, a close inspection of panels in Fig. 6 for planets b, c, and d reveals that the dynamic model fits the measurements *even better* than the first terms of the Gibbs functions, particularly at the earliest *HST* images. This is suggestive for noticeable deviations of the N-body orbits from their first- and second-order Keplerian approximations.

Moreover, the model orbit of planet e (shown in bottom panel of Fig. 6) seems to pass in between three apparently accurate observations. This may indicate underestimated errors of the recent astrometric measurements in (Esposito et al. 2013). These data points are likely responsible for orbital fits implying a large eccentricity of planet e or a significant non-coplanarity (Esposito et al. 2013). Both the linear and quadratic approximations of the Gibbs series are ambiguous that leads to badly constrained initial condition for planet e if kinematic or even plain dynamical models are applied.

Statistics of all models gathered in $\sim 10^5$ runs of MCOA are presented on Figs 7 and 8. Fig. 7 shows projections of the orbital parameters on to (a_i, e_i)-planes where $i =$ e, d, c, b, and marked with grey filled circles. We computed the maximal Lyapunov exponent expressed through the MEGNO indicator (Section 5) for all these initial conditions for 160 Myr. Solutions providing $|\langle Y\rangle - 2| < 0.05$ at the end of the integration time are considered as quasi-periodic and rigorously stable. Blue and red filled circles in Fig. 7 mark such stable (quasi-periodic, regular) models within the $(3\sigma, 6\sigma)$ and 3σ joint confidence levels, respectively. The statistics demonstrate that orbital parameters in model IVa are well constrained. This is also illustrated on Fig. 4. Green curves illustrate geometrically a

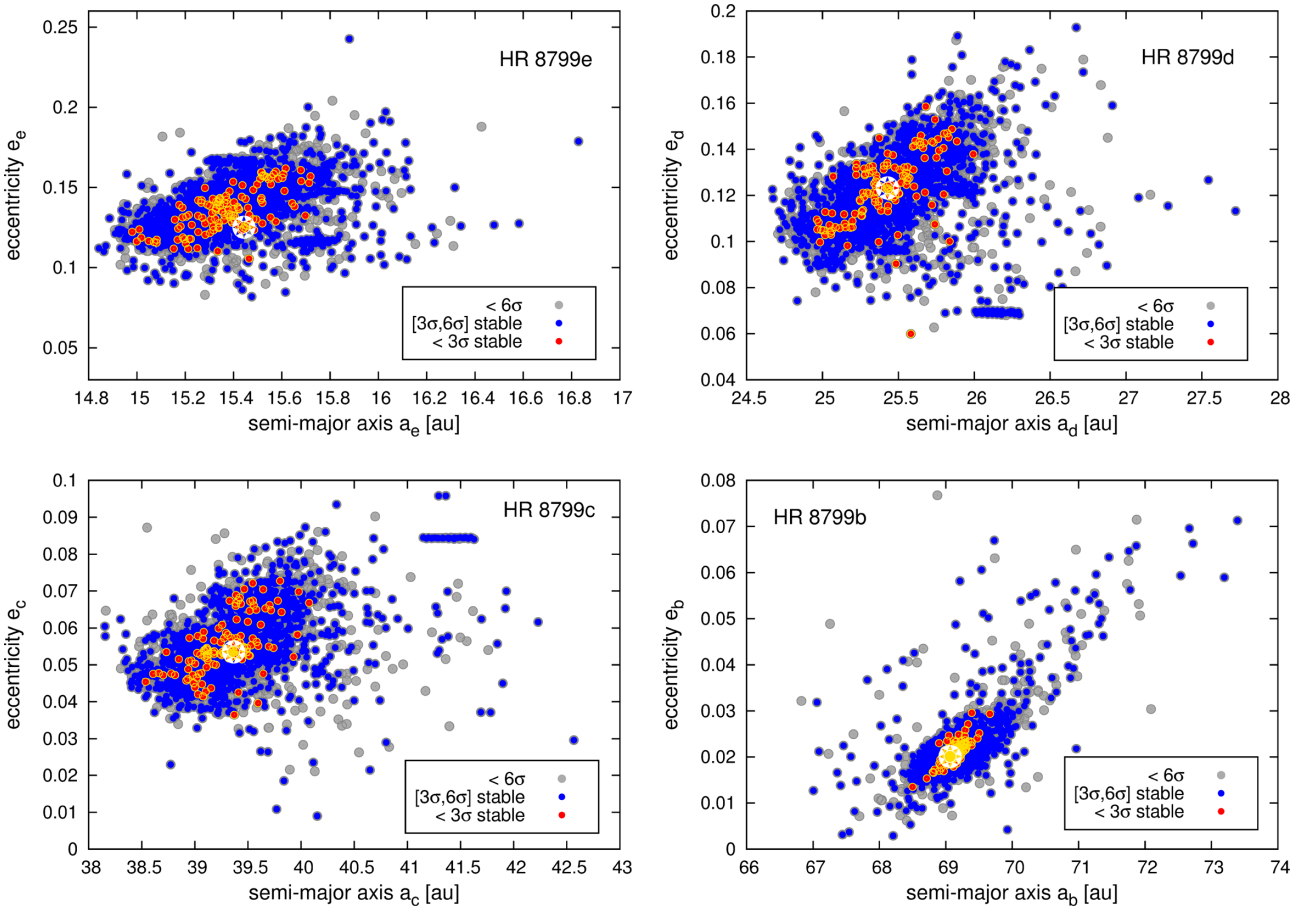

Figure 7. Best-fitting solutions projected on to semimajor axis – eccentricity planes for subsequent planets. The star symbol marks the nominal, best-fitting solution in Table 1. Grey circles are for all solutions within 6σ confidence interval ($\sqrt{\chi^2_\nu} < 1.5$). Blue and red circles are for *rigorously stable* models in the range of $(3\sigma, 6\sigma)$, ($1.2 < \sqrt{\chi^2_\nu} < 1.5$), and within 3σ ($\sqrt{\chi^2_\nu} \leq 1.2$), respectively. Their $|\langle Y\rangle - 2| < 0.05$ for the integration time-span of 160 Myr, covering a few estimates of the HR 8799 lifetime in the literature.

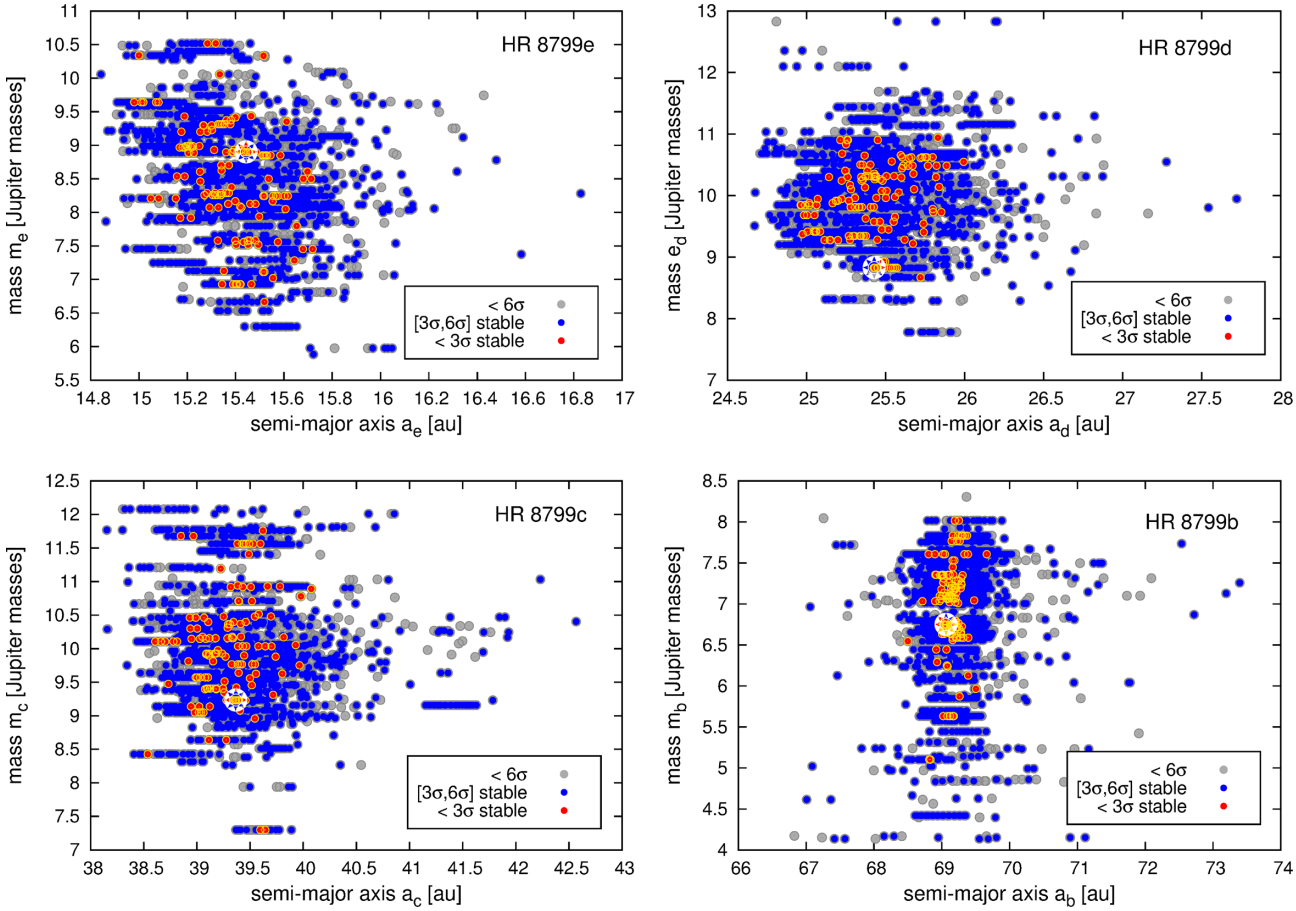

Figure 8. Statistics of the best-fitting solutions to four-planet model IVa and data set D1 illustrated as projections on to semimajor axis – masses planes for subsequent planets. The star symbol marks the nominal, best-fitting solution IVa in Table 1. Grey circles are for all 6σ solutions with $\sqrt{\chi^2_\nu} < 1.5$. Blue and red circles are for *rigorously stable* models in the range of $(3\sigma, 6\sigma)$, $1.2 < \sqrt{\chi^2_\nu} < 1.5$, and within 3σ ($\sqrt{\chi^2_\nu} \leq 1.2$), respectively. Their $|\langle Y\rangle - 2| < 0.05$ for the integration time-span of 160 Myr, covering a few estimates of the HR 8799 lifetime.

dispersion of the orbital arcs of stable solutions within 3σ level around the best-fitting model.

Fig. 8 illustrates best-fitting models projected on to (a_i, m_i)-planes in the same manner as shown in Fig. 7. Nominal masses are (9, 10, 10, 7) $m_{\rm Jup}$ for planets e, d, c, b, respectively. At the beginning of each optimization run, the actual masses were selected from the normal distribution within 2–3 $m_{\rm Jup}$ standard deviations around the nominal masses. The statistics presented in Fig. 8 reveal a relatively extended range of dynamical masses in the 4–12 $m_{\rm Jup}$ range providing stable (quasi-periodic) solutions. This experiment shows that the astrophysical determination of the masses through cooling models is well consistent with dynamical constraints driven by the migration. This somehow contradicts previous studies concluding that the stability of HR 8799 system is possible only when the masses are at the lowest estimates (Sudol & Haghighipour 2012; Esposito et al. 2013).

Finally, we computed dynamical MEGNO maps in the (a_i, e_i)-planes of osculating elements for all planets (see model IVa in Table 2). The results are shown on Fig. 9. The nominal best-fitting model IVa, which is marked with a star symbol, is found in relatively extended zones of stable motions. These islands reveal complex structure of the 1e:2d:4c:8b MMR, demonstrating that solution IVa is deeply locked in this multiple resonance. See also Section 5 for the event time $T_{\rm E}$ maps and the critical argument $\theta_{1:\,2:\,4:\,8}$ in a close neighbourhood of the best-fitting model IVa.

4.1.1 Independent refinement of fit IVa through GAMP

MCOA is a CPU demanding and complex algorithm that requires many trials to derive the best-fitting model. To verify that fit IVa is indeed optimal, and to better characterize this solution statistically, we applied other, independent method of constrained optimization which is called GAMP (acronym of the Genetic Algorithm with the MEGNO Penalty; Goździewski, Breiter & Borczyk 2008b). GAMP relies on penalizing unstable dynamical models by some large value of $\sqrt{\chi^2_\nu}$. In this experiment, the inclinations and masses are free parameters of the model. Masses were searched in the $[4, 20]m_{\rm Jup}$ range, and inclinations in the $[10^\circ, 33^\circ]$ range, respectively. Other parameters are confined to a hypercube around fit IVa bounded by roughly ± 20 per cent deviations from each orbital element in model IVa. At the optimization stage, the penalty term (system stability) is examined through the MEGNO indicator, equivalent to the Lyapunov exponent. This indicator must be evaluated for possibly short time-span 1000–2000 outermost periods of planet b, due to significant CPU overhead. As the result, we gathered $\simeq$3000 stable models with $1.13 < \sqrt{\chi^2_\nu} < 1.15$ computed with 4 degrees of freedom (DOF), in accord with Section 3.2. Each solution in this set is formally better in terms of $\sqrt{\chi^2_\nu}$ than fit IVa, and roughly within 3σ of the best-fitting model found in this independent search with $\sqrt{\chi^2_\nu} \approx 1.5$ for 28 DOF (all orbital elements and masses). For each of these models, we calculated MEGNO for

Table 2. Osculating parameters of the best-fitting four-planet solutions. The stellar mass $m_0 = 1.56\,\mathrm{M}_\odot$. Osculating epoch is 1998.83.

Model	Planet	$\sqrt{\chi^2_\nu}$	$m\,(m_{\rm Jup})$	a (au)	e	I(deg)	Ω(deg)	ω (deg)	$\mathcal{M}_0$ (deg)
	e		8.895 706	15.443 557	0.124 958			112.198 950	325.667 983
IVa	d	1.147	8.825 311	25.428 138	0.123 029	25.337 113	64.180 486	26.598 297	57.901 471
	c		9.231 718	39.366 093	0.053 442			87.154 893	147.870 426
	b		6.748 302	69.063 963	0.020 022			30.350 808	321.261 401
	e		7.957 365	15.675 018	0.159 392			110.340 454	325.747 637
IVb	d	1.172	9.961 193	25.896 792	0.151 664	28.504 826	65.493 989	24.572 894	55.420 303
	c		10.417 128	39.638 907	0.071 622			84.322 520	149.892 256
	b		7.920 258	69.121 225	0.020 655			27.328 258	322.721 614
	e		7.511 610	15.600 838	0.130 436			110.787 818	334.739 478
IVc	d	0.474	8.871 059	25.451 257	0.108 087	27.616 454	56.264 572	29.153 001	63.162 502
	c		8.479 021	39.679 862	0.065 732			103.182 135	137.630 090
	b		8.722 503	68.747 691	0.018 124			42.802 760	317.361 404

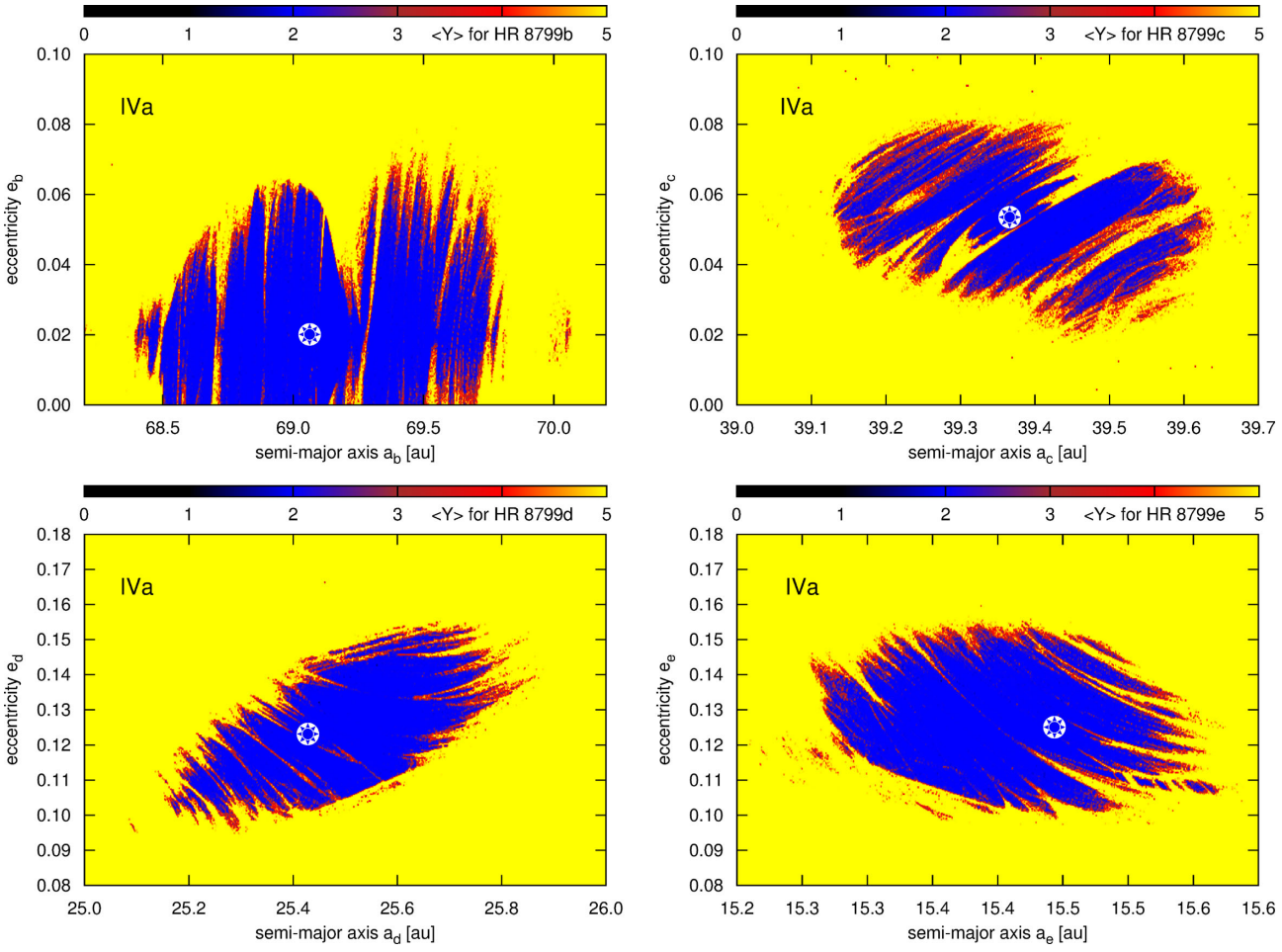

Figure 9. Dynamical maps in terms of the maximal Lyapunov exponent, expressed by the MEGNO fast indicator $\langle Y \rangle$, and shown in the semimajor–eccentricity planes for the four-planet model IVa. The star symbol marks the best-fitting model (Table 1), stable, quasi-periodic solutions are marked in blue. The resolution of each map is 720 × 360 pixels. Integration time for each pixel is ∼20 000 orbital periods of the outermost planet (≃10 Myr).

32 000 periods of planet b (16 Myr). We verified (Section 5) that MEGNO converged to (2 ± 0.05) indicates a solution dynamically stable for at least 10 times longer motion times.

The results (stable solutions in the 1σ range of the best-fitting GAMP model) are shown in panels of Fig. 10, which are projections of the found models on to two parameter planes: the semimajor axis versus eccentricity, and the inclination versus mass. In all cases, the nominal fit is located roughly in the middle of the stable set. All inclinations remain within a few degrees around fit IVa, and masses are found systematically below ∼14 $m_{\rm Jup}$ and ∼18 $m_{\rm Jup}$ for two inner planets, and two outer planets, respectively. The results confirm that fit IVa is robust to relatively large masses, still well

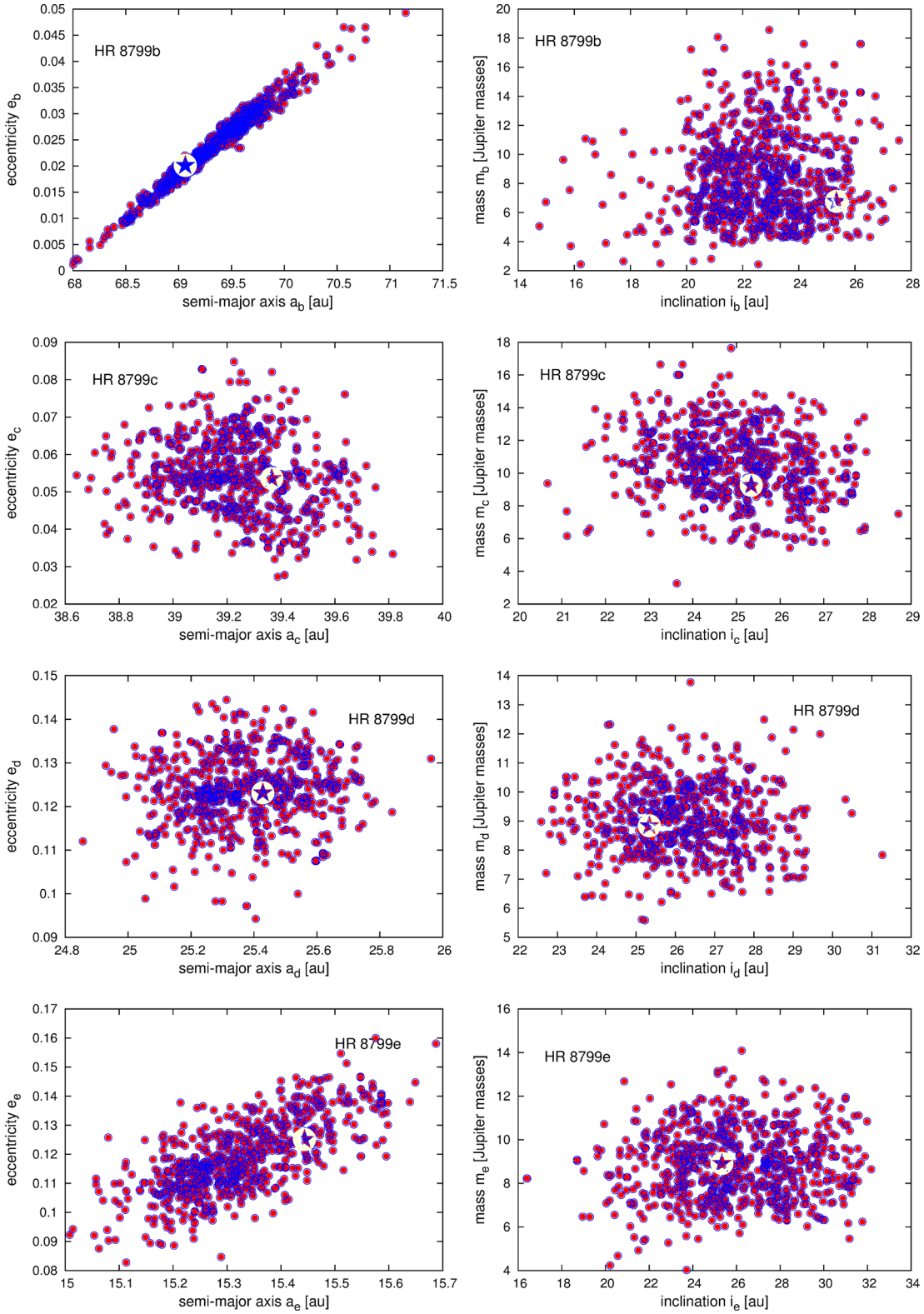

Figure 10. Best-fitting stable solutions derived with the GAMP algorithm (see the text for details) projected on to semimajor axis – eccentricity planes (*left-hand column*), and on to inclination – mass planes (*right-hand column*). The star symbol marks the nominal, best-fitting solution in Table 1. Filled circles are for stable solutions within $\sqrt{\chi^2_\nu} < 1.15$ that corresponds to 1σ of the best-fitting model found in the GAMP search with $\sqrt{\chi^2_\nu} \simeq 1.13$. Their $|\langle Y \rangle - 2| < 0.05$ for the integration time-span of 16 Myr.

consistent with the estimates from cooling models. The spread of individual inclinations may be estimated as $\sim 5^\circ$ around IVa value of $\sim 25^\circ$.

4.2 Statistical study of migration

We used the heuristic model of migration (equation 1) to find how frequently a particular four-planet MMR chain forms, dependent on planetary masses and time-scales of migration. In a first experiment we fixed planetary masses at their nominal values in the HR 8799 system, i.e. 9, 10, 10, 7 $m_{\rm Jup}$ (counting from the innermost to the outermost planet, respectively). Parameters of the migration model were chosen randomly from wide ranges. Using notation in Sections 3.1 and 3.2, these ranges are the following: $\log_{10}\tau_{1,0}({\rm yr}) \in [6, 10]$, $\log_{10}T_1({\rm yr}) \in [6, 10]$, $K \in [1, 100]$, $\alpha_1 \in [-2.0, -0.1]$. The second term $\tau_{2,0}$ was not taken into account. The initial orbits are distributed exponentially, with $a_1 \in [30, 160]$ au and $\beta \in [0.3, 1.8]$. The orbits calculated from the exponential distribution are then shifted randomly with Gaussian distribution ($\sigma = 0.2$ of the nominal values). Initial eccentricities were random within [0, 0.05] range. A given initial system was integrated for 100 Myr.

We found that slightly less than 20 per cent of simulations (18 per cent, 1739 of 9488) ended up as stable resonant configurations. The most frequent chain of MMRs is 3: 1, 2: 1, 2: 1, i.e. 1e: 3d: 6c: 12b MMR. More than a half of stable final systems are of this type. Another solutions 3: 1, 3: 1, 2: 1 (17 per cent) and 4: 1, 3: 1, 2: 1 (14 per cent) are also relatively common in a sample of final configurations. The double Laplace MMR (2: 1, 2: 1, 2: 1 or equivalently 1e: 2d: 4c: 8b MMR) appeared in $\sim$10 per cent of the stable runs. By a resonant four-planet configuration we mean a configuration characterized by its critical argument ϕ librating around a particular libration centre. Table 3 summarizes the results obtained for the nominal masses of the planets, as well as masses 50 per cent higher and 50 per cent lower than these values, respectively.

When masses of the planets are smaller than the nominal values, i.e. 4.5, 5, 5, 3.5 $m_{\rm Jup}$, a fraction of systems that survived the integration time increases to $\sim$29 per cent (2878 of 9960). The number of possible final configurations also increases. Some of MMR chains absent in the previous test appear for smaller masses, e.g. 2: 1, 2: 1, 3: 2 (13 per cent of stable systems). The double Laplace MMR now appears more frequently ($\sim$20 per cent), while 3: 1, 2: 1, 2: 1 appears in $\sim$38 per cent cases, i.e. less frequently when compared to the previous test.

When masses are increased (13.5, 15, 15, 10.5 $m_{\rm Jup}$), only $\sim$12 per cent (1196 of 10235) of systems end up as stable chains of MMRs. Moreover, there are fewer possible final configurations. Particularly, the double Laplace resonance does not appear at all. Three most common chains of MMRs constitute $\sim$92 per cent of stable systems. This test could provide us an upper limit on planetary masses in the HR 8799 system. For planets massive enough, the double Laplace resonance, which best matches the observations, may unlikely form through convergent migration of already formed planets. We would like to warn the reader that the migration model may be too simplistic: for instance, it does not take into account any (possibly substantial) mass increase during the migration. Any definite conclusions should be taken with much caution here.

Because parameters of the migration model were chosen from very wide ranges, planets migrate in different time-scales, from one simulation to another. This leads to different final MMR configurations. Fig. 11 presents the results for four most common MMRs obtained during simulations with the nominal masses. The left-hand part of the diagram shows the time-scales for the double Laplace resonance. The red filled circles present average values of $L \equiv \log_{10}\tau({\rm yr}) \equiv \log_{10} a/\dot{a}$ for two innermost planets just before they are captured into the 2: 1 MMR. The standard deviation of σ_L is depicted by the bars. The planets migrate in average time-scales of $\approx$1 Myr, i.e. $L \approx 6$ (note that the second planet migrates slightly faster), with $\sigma_L \approx 0.5$. Green filled circles present L for the middle pair of planets, while blue filled circles are for the outermost pair. The migration time-scale required to form the double Laplace MMR is of the order of 1 Myr.

The MMRs chain 3: 1, 2: 1, 2: 1 form when the migration occurs slightly slower (2–3 Myr on average). Another two chains 3: 1, 3: 1, 2: 1 and 4: 1, 3: 1, 2: 1 appear for even larger L. The latter MMR

Table 3. Percentage of simulated MMRs for different masses of planets, i.e. the nominal masses of 9, 10, 10, and 7 $m_{\rm Jup}$ from the innermost to the outermost planet, respectively (*middle column*), all masses increased by 50 per cent (*left-hand column*) and decreased by 50 per cent (*right-hand column*), respectively. A notion of '<0.1' means that there was one or at most two solutions of a given type, while '–' means no solution of this type.

MMR chain	Percentage of solutions		
e:d, d:c, c:b	$1.5 \times m$	$1 \times m$	$0.5 \times m$
2: 1, 2: 1, 2: 1	–	10.2	20.3
2: 1, 2: 1, 3: 1	–	–	<0.1
2: 1, 2: 1, 3: 2	–	–	12.9
2: 1, 2: 1, 4: 1	–	0.2	–
2: 1, 5: 3, 2: 1	–	–	2.3
2: 1, 3: 1, 2: 1	–	–	0.3
2: 1, 3: 1, 3: 1	–	–	<0.1
2: 1, 3: 1, 5: 2	–	–	<0.1
2: 1, 3: 2, 2: 1	–	–	<0.1
3: 1, 2: 1, 2: 1	57.5	51.8	37.7
3: 1, 2: 1, 3: 1	–	0.1	0.5
3: 1, 2: 1, 4: 1	–	–	<0.1
3: 1, 2: 1, 3: 2	–	0.1	1.8
3: 1, 3: 1, 2: 1	13.5	17.0	13.1
3: 1, 3: 1, 3: 1	–	0.2	0.2
3: 1, 5: 2, 2: 1	–	0.1	0.3
3: 1, 5: 2, 3: 1	–	–	<0.1
4: 1, 2: 1, 2: 1	6.4	3.1	0.8
4: 1, 2: 1, 3: 1	0.1	0.1	<0.1
4: 1, 3: 1, 2: 1	20.9	14.0	3.6
4: 1, 3: 1, 3: 1	–	0.2	0.5
4: 1, 3: 1, 4: 1	–	0.1	–
4: 1, 3: 1, 5: 2	–	0.1	–
4: 1, 4: 1, 2: 1	0.1	0.2	0.2
4: 1, 4: 1, 4: 1	0.1	0.1	<0.1
4: 1, 4: 1, 5: 2	–	0.1	0.1
4: 1, 5: 2, 4: 1	–	0.1	–
4: 1, 5: 2, 2: 1	–	0.1	<0.1
4: 1, 5: 2, 5: 2	–	–	<0.1
5: 2, 2: 1, 2: 1	1.3	2.5	4.0
5: 2, 2: 1, 3: 2	–	–	0.3
5: 2, 3: 1, 2: 1	–	–	0.4
5: 2, 3: 1, 4: 1	0.1	0.1	–
5: 2, 5: 2, 2: 1	–	–	0.1
5: 2, 5: 2, 4: 1	0.1	–	–
5: 2, 5: 2, 5: 2	–	–	<0.1
3: 2, 2: 1, 2: 1	–	–	0.2
5: 3, 2: 1, 3: 2	–	–	<0.1
Total number of solutions	1196	1739	2872

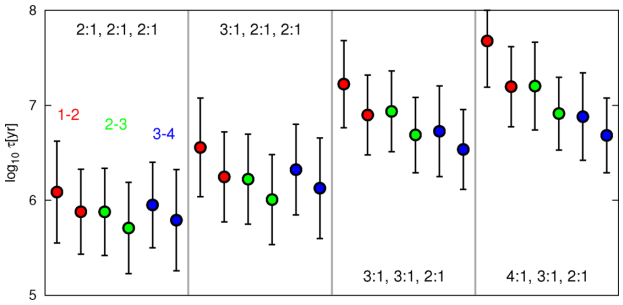

Figure 11. Time-scales of migration $\tau \equiv a/\dot{a}$ for a given planet before MMR capture with a neighbouring planet. Each column is for a different multiple MMR chain. Red colour marks values of τ for the innermost pair (planets numbered as 1 and 2), green colour is for the middle pair (planets 2 and 3), and blue colour is for the outermost pair (planets 3 and 4), respectively.

chain form typically for $L \approx 7$ for a middle pair of planets. The inner pair migrates slower, while the outer pair migrates typically faster. The general conclusion is that the characteristic time-scales of migration leading to a particular chain of MMRs, are different for different chains.

4.3 Model IVb: Could planet HR 8799 e be predicted?

Decades of observations are required to constrain orbital parameters of very long period planets with standard methods. Relying on discrete and in some sense *deterministic* outcomes of the migration algorithm, we may consider different architectures of the resonant systems with even very limited observations. At an extreme case, we may turn back to 2008, when measurements for three outer planets were published in the discovery paper (Marois et al. 2008). Two years later, the fourth planet was detected. Having in mind the multiple MMR model of the four-planet system, we may ask: Could the fourth planet be predicted or found in the present observed place if we did not have even a single data point for this planet?

Following the general idea, we assume that orbits of planets b, c and d, as well as the 'unseen' planet e are outcomes of the migration scenario. The Laplace 1d:2c:4b MMR of the outermost planets found in the early dynamical papers must be not necessarily preserved by the four-planet architecture. Actually, the literature is not consistent about this problem. For instance, due to mutual interactions and complex dissipative evolution, the 1c:2b MMR between planets c and d might be changed to 1c:3b MMR. Many other two-body resonances are possible as well (see Section 4.2). The primary factor that makes it possible to distinguish between these cases are the observations. Assuming that the system as a whole evolves towards certain, discrete, and small number of states

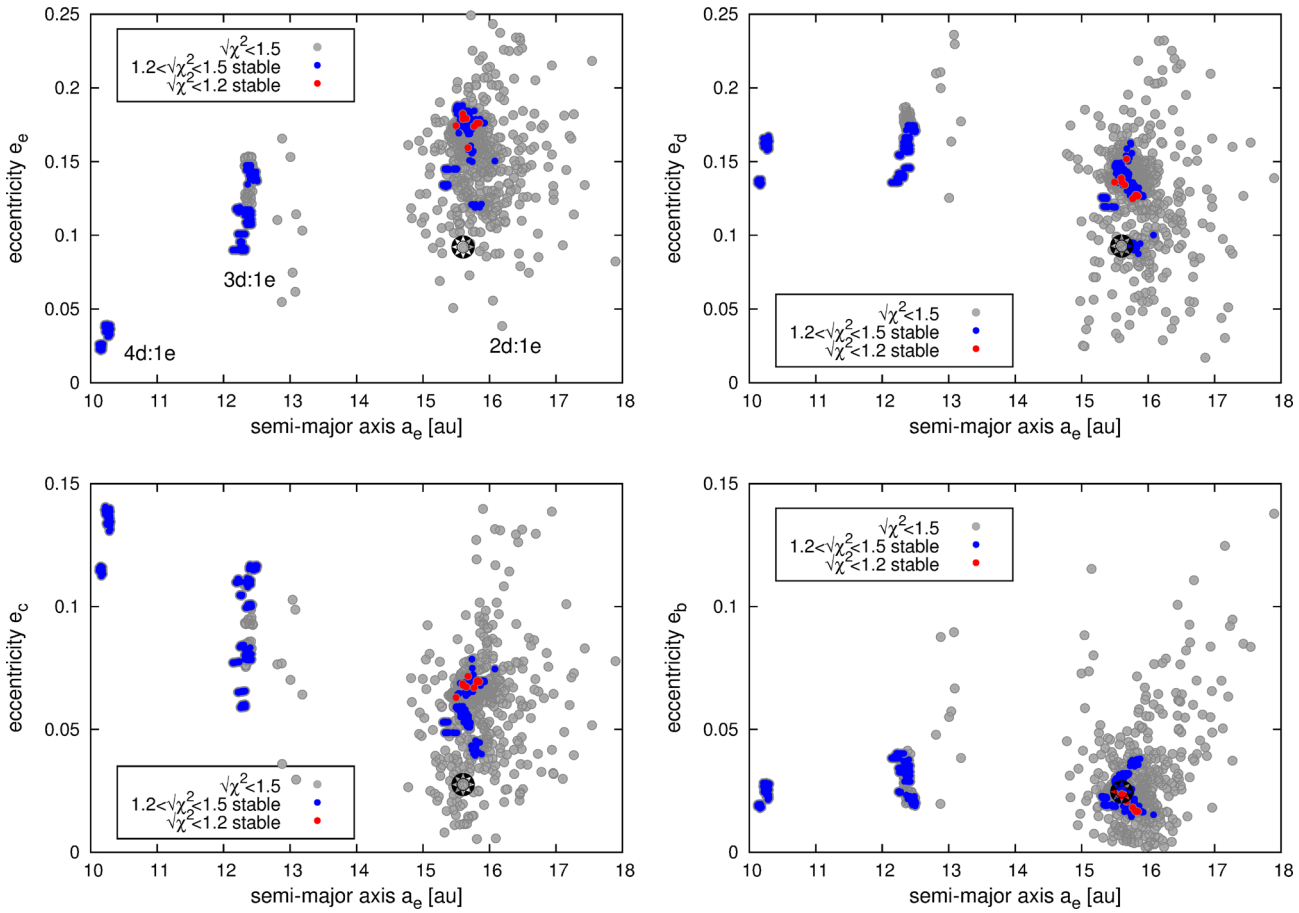

Figure 12. Best-fitting solutions to four-planet model IVb (with 'unseen' planet e) and data set D5 comprising of all observations of three planets b, c, and d, *without data for planet e*, projected on to (a_e, x)-plane, where x is e_e, e_d, e_c, e_b. Grey symbols denote solutions within 6σ confidence interval ($\sqrt{\chi^2_\nu} < 1.5$), blue and red symbols are for stable solutions with (3σ, 6σ), equivalent to $1.2 < \sqrt{\chi^2_\nu} < 1.5$, and for 3σ models ($\sqrt{\chi^2_\nu} < 1.2$), respectively.

(multiple MMRs), the observations 'decide' which configuration is the right one.

We performed a series of simulations concerning the four-planet model and D5 data set to test this idea. In this scenario, the innermost planet e is unseen, and the four-planet model combined with data set D5 is called model IVb. The results of the MCOA search are illustrated in Figs 12–14. Similarly to the model IVa, Fig. 12 illustrates projections of the best-fitting osculating elements

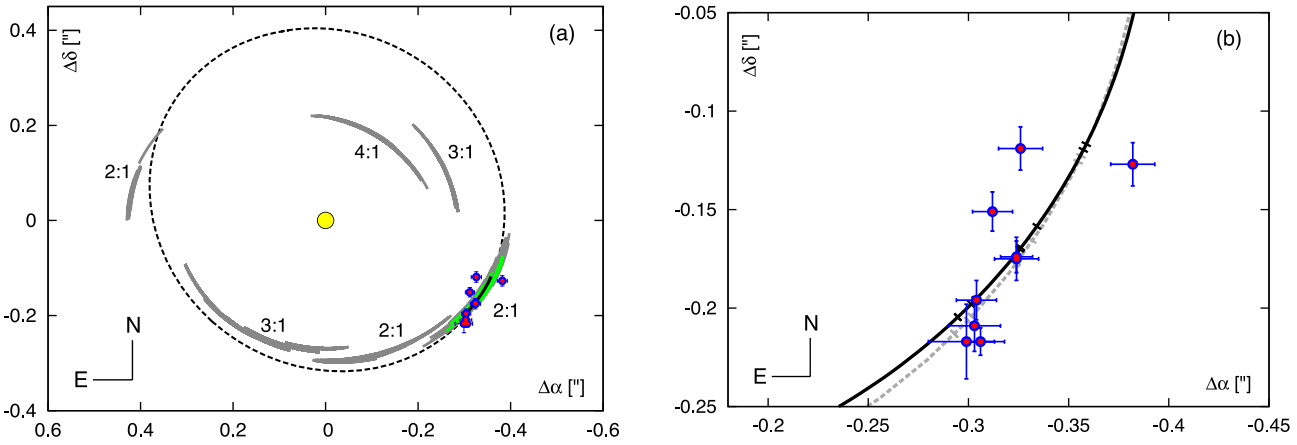

Figure 13. *Left-hand panel:* relative astrometry of planet e (red/blue symbols) with best-fitting four-planet model IVa to all observations (dashed curve). Grey, green, and black curves show arcs of different families of the four-planet model IVb to the most recent observations of planets b, c, and d (data set D5). Black curve is for the best-fitting model, green curves are for 3σ solutions and grey curves are for 6σ models ($\sqrt{\chi^2_\nu} < 1.5$). *Right-hand panel:* a close-up of the left-hand panel. The black curve is for the best-fitting stable solution IVb, grey dashed curve is for the best-fitting nominal, four-planet model IVa.

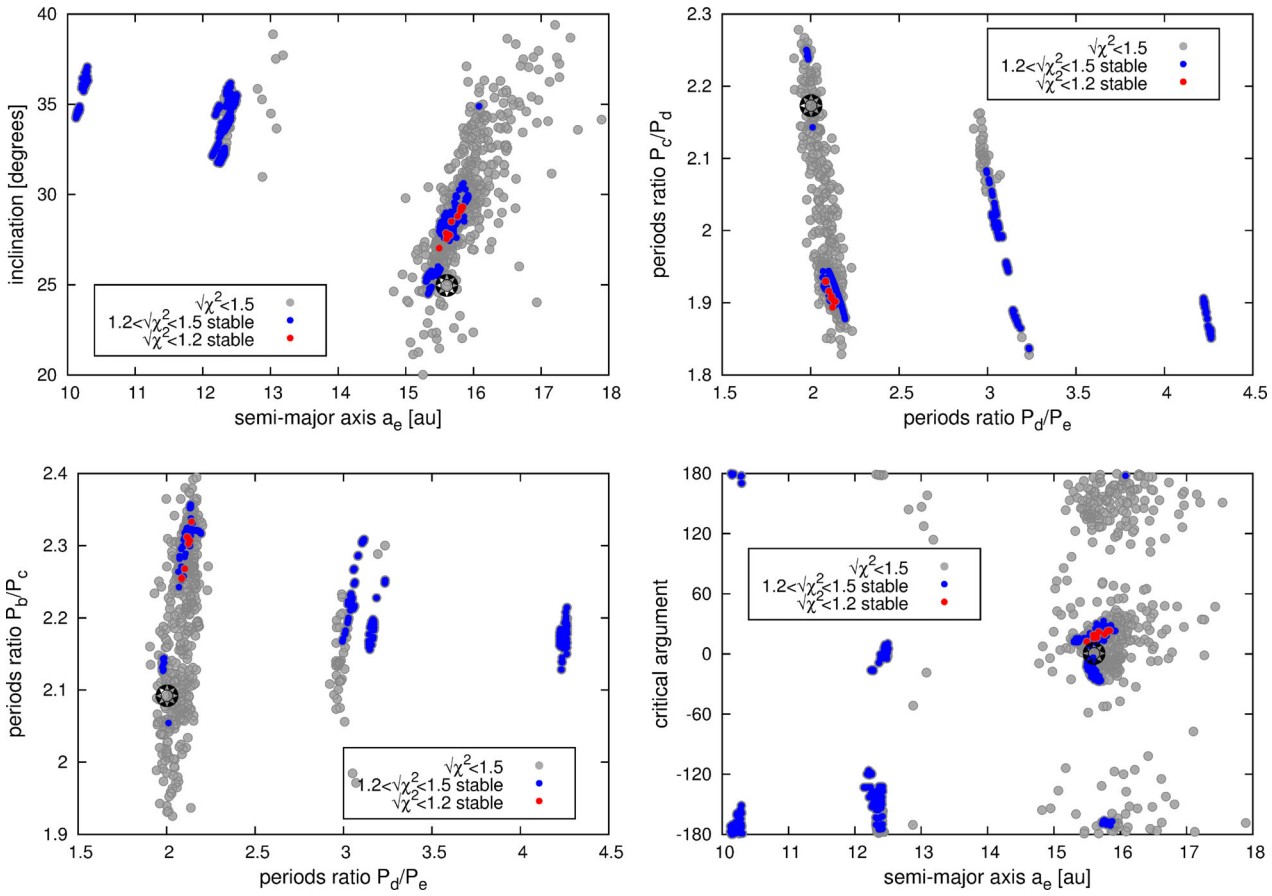

Figure 14. Parameters of the best-fitting model IVb to data set D5 projected on to (a_e, I)-, (P_d/P_e, P_c/P_d)-, (P_d/P_e, P_b/P_c)-, and (a_e, criticalangle)-planes. The star symbol marks the nominal, best-fitting solution. Grey filled circles are for all solutions within 6σ confidence interval, $\sqrt{\chi^2_\nu} < 1.5$. Blue and red filled circles are for *rigorously stable* models in the range of (3σ, 6σ), equivalent to $1.2 < \sqrt{\chi^2_\nu} < 1.5$, and within 3σ confidence level ($\sqrt{\chi^2_\nu} \leq 1.2$), respectively. Stable models are defined by $|\langle Y \rangle - 2| < 0.05$ for the integration time-span of 160 Myr. The critical arguments for 1e:2d:4c:8b MMR, 1e:3d:6c:12b MMR, and 1e:4d:8c:16b MMR are $\theta_{1:\,4:\,8:\,16} = \lambda_e - 2\,\lambda_d - \lambda_c + 2\,\lambda_b$, $\theta_{1:\,3:\,6:\,12} = \lambda_e - 4\,\lambda_d + \lambda_c + 2\,\lambda_b$, and $\theta_{1:\,4:\,8:\,16} = \lambda_e - 3\,\lambda_d - 6\,\lambda_c + 8\,\lambda_b$, respectively.

Table 4. Osculating elements and masses of the best-fitting three-planet models IIIa and IIIb. The stellar mass $m_0 = 1.56\,M_\odot$. The osculating is epoch 1998.83.

Model	Planet	$\sqrt{\chi^2_\nu}$	$m\,(m_{\rm Jup})$	a (au)	e	I(deg)	Ω(deg)	ω (deg)	$\mathcal{M}_0$ (deg)
	d		10.135 136	25.045 527	0.084 720			12.364 179	96.623 071
IIIa	c	1.060	10.018 128	40.370 405	0.047 036	26.566 822	64.680 038	103.509 878	140.603 388
	b		6.953 918	68.047 272	0.002 379			1.1423 28	352.986 933
	d		7.923 625	24.234 342	0.072 091			203.586 910	95.496 437
IIIb	c	0.053	10.656 124	39.482 602	0.019 226	18.867 507	236.887 633	296.672 146	135.283 261
	b		4.587 625	68.108 515	0.002 603			146.618 350	35.666 508

on to different planes. Grey filled circles are for solutions with $\sqrt{\chi^2_\nu}$ within the 6σ confidence level, while red and blue filled circles are for 3σ models. The statistics reveals that configuration involving 1e: 2d MMR describes data set D5 better than two other configurations with 1e: 3d MMR and 1e: 4d MMR.

We should realize here that multiple resonant configurations are determined not only by a_e, but may be also distinguished due to different e_d, e_c, e_b. For instance, the initial conditions for a system involved in the 1e:2d:4c:8b MMR and in the 1e:3d:6c:12b MMR are significantly different. This is clearly seen in the (a_e, e_c)-panel in Fig. 12. Because e_i are different in these two concurrent solutions, also the best-fitting inclinations are different, as shown in the top-left panel of Fig. 14. While the 1e: 2d MMR implies $I \approx 25^\circ$, the best-fitting models with 1e: 3d MMR and 1e: 4e MMR provide much larger inclination, i.e. $I \sim 35^\circ$. The 1e:2d:4d:8b MMR is favoured due to lowest value of $\sqrt{\chi^2_\nu}$ and because its inclination matches closely the inclination of the stellar equator $\sim 25^\circ$.

These results suggest that the optimization of the four-planet model with yet undetected innermost planet might at least help to narrow the search areas for such a putative object and to interpret the speckle images. Fig. 13 shows the actual observations of planet e in data set D1 (let us recall: these data *were not used* in the IVb experiment) with the best-fitting orbits of model IVb overplotted. For a reference, the left-hand panel of Fig. 13 illustrates the best-fitting orbit IVa (dashed curve) and arcs of rigorously stable configurations (solid curves) in model IVb, respectively. Black curve is for the best-fitting model IVb, grey curves are for configurations IVb within 6σ, while green curves illustrate solutions within 3σ confidence levels. Remarkably, the best-fitting stable solutions IVb are consistent with the actual observations as well as with the full model IVa. The right-hand panel of Fig. 13 shows a close-up of the previous plot. The best-fitting orbits IVb (black curve) are plotted together with the best-fitting nominal four-planet model IVa (grey dashed curve). Positions of the planets at the observational epochs are marked with small tics. Clearly, these two orbits almost overlap.

Finally, we carried out a number of simulations to examine whether the four-planet model with unseen planet e might provide better fits than the three-planet model. Both these models appear to match observations in data set D5 equally well.

4.4 Models IIIa, IIIb, and IVc: single-image characterization

The orbital periods of directly imaged planets usually count in tens or hundreds of years. The common optimization techniques require a long period of observations to establish the true orbital architecture. The literature devoted to the HR 8799 system is good evidence of this apparently unavoidable problem. However, if a multiple, resonant configuration is observed, the migration algorithm may be helpful to constrain its orbits even by *one single-epoch* observation. This means basically single-image orbital characterization of the system, although in the real world much longer observational time span is required, for instance, to confirm common proper motion and the same parallax at least two, well-separated epochs are required.

4.4.1 *Model IIIa: the data in Marois et. al (2008) revisited*

Data set D2 in (Marois et al. 2008) serves as a good example of time-limited observations, which were examined by many groups. We performed the migration constrained optimization of these data with three-planet model (IIIa). This example might be also thought as an excellent test-bed of the MCOA.

Osculating elements of best-fitting model IIIa for the epoch $t_0 = 1998.71$ are given in Table 4. Fig. 15 shows the orbital geometry of model IIIa (solid grey curves) compared to model IVa (dashed curves), and overplotted on orbital arcs of stable solutions within 3σ-confidence level (green curves). The three- and four-planet models can be hardly distinguished, suggesting that the Laplace resonance of three outer planets is particularly robust for a perturbation, as large as the inner planet e may introduce.

The statistics of best-fitting models with $\sqrt{\chi^2_\nu}$ within the 6σ confidence interval is shown in Fig. 16. This result confirms and complements the earlier literature data. Similarly to model IVa, we found relatively wide mass ranges of *rigorously stable* solutions (the right-hand column in Fig. 16) which are fully consistent with astrophysical estimates, independent on the geometric model of orbits.

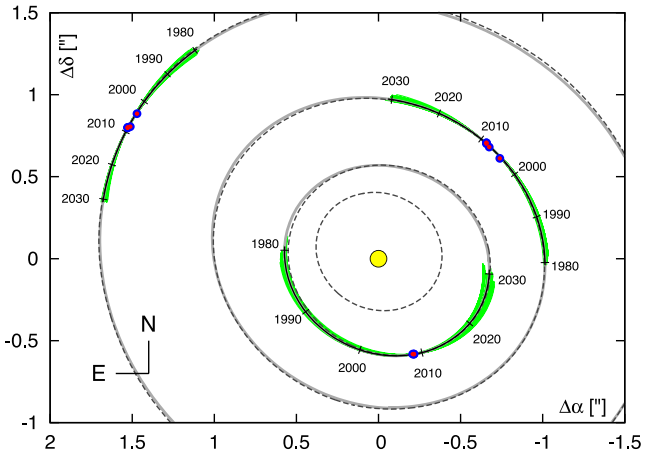

Figure 15. Relative astrometric positions of the HR 8799 planets (red filled circles) and orbital arcs for the best-fitting model IIIa combined with data set D2 in the discovery paper (Marois et al. 2008). Best-fitting orbits of this model are plotted with solid grey curves. For a reference, black, dashed curves are for the best-fitting nominal four-planet model IVa related to the whole available data in the literature (data set D1).

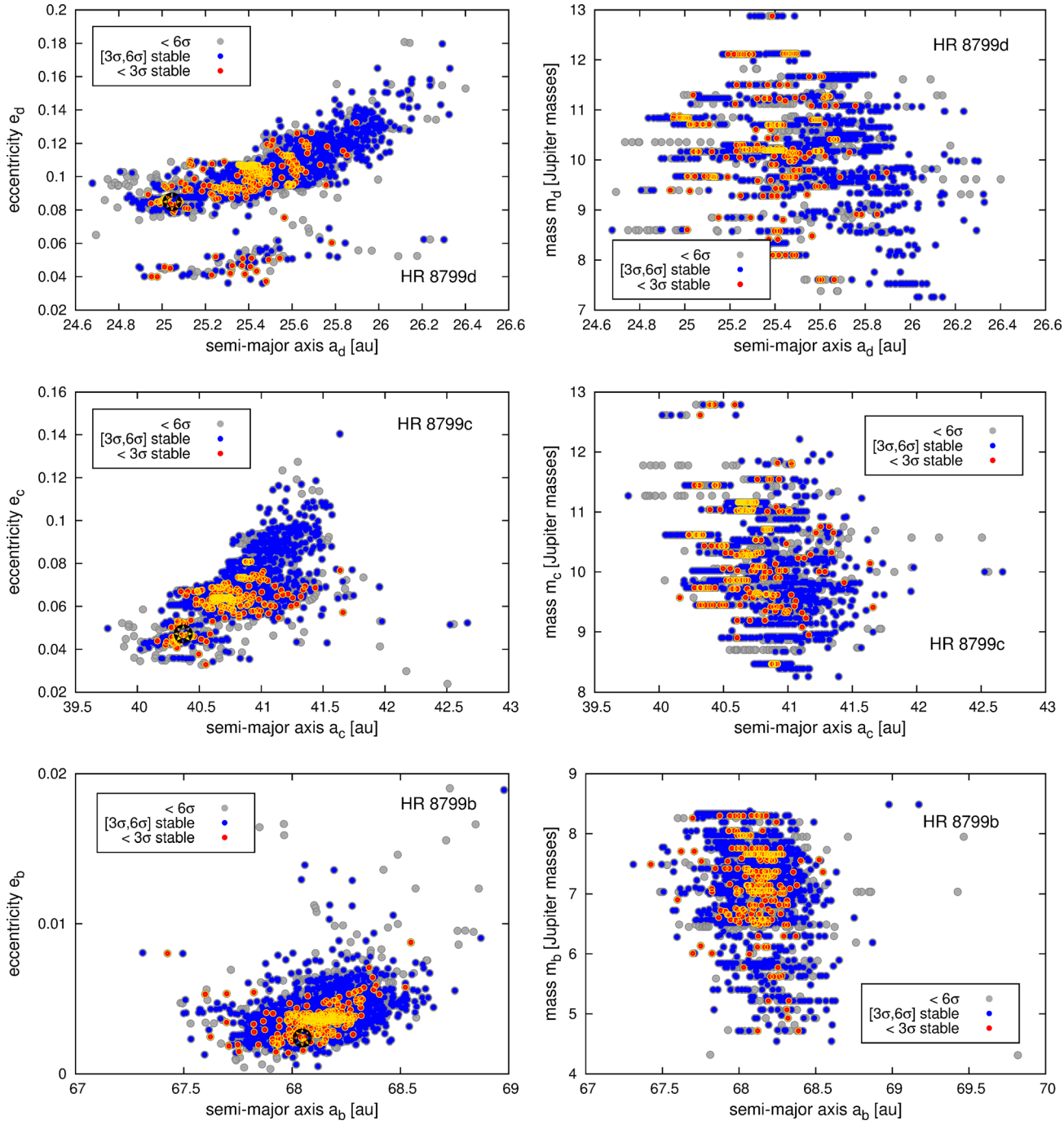

Figure 16. Best-fitting three-planet models IIIa to the data published in the discovery paper (Marois et al. 2008), dataset D2, projected on to planes of the semimajor axis – eccentricity (*left-hand column*) and the semimajor axis – masses (*right-hand column*), respectively, for subsequent planets. The star symbol marks the nominal, best-fitting solution. Grey filled circles are for all solutions within $\sqrt{\chi^2_\nu} < 1.5$ (roughly 6σ confidence level). Blue and red circles are for *rigorously stable* models in the range of $(3\sigma, 6\sigma)$ ($<1.2\sqrt{\chi^2_\nu} < 1.5$), and for the 3σ ($\sqrt{\chi^2_\nu} \leq 1.2$) confidence levels, respectively. Their $|\langle Y\rangle - 2| < 0.05$ for the integration time-span of 160 Myr covering assumed lifetime of HR 8799.

Our stable models cover smoothly both the 10–10–7 $m_{\rm Jup}$ range as well as the 7–7–5 $m_{\rm Jup}$. The statistics of stable models suggests the upper limit of masses $\sim$13 $m_{\rm Jup}$. In spite of many trials with masses extended to $\sim 20 m_{\rm Jup}$, we could not find any stable configurations with masses above this limit which are *consistent with observations* at least at the 6σ confidence level. Such a limitation indicates that the HR 8799 companions are really planets with masses below the deuterium burning limit.

We also computed dynamical maps for the best-fitting model (Fig. 17), which corresponds to three-planet configuration deeply involved in the classic Laplace 1d:2c:4b MMR. The bottom-right panel illustrates the critical argument $\theta_{\rm 1d:\,2c:\,4b} = \lambda_{\rm d} - 3\lambda_{\rm c} + 2\lambda_{\rm b}$ that librates around 90°. The best-fitting configuration is found in the central part which perfectly overlaps with the minimum of the critical angle θ = 1d: 2c: 4b librating with a semi-amplitude $\sim$20°. Remarkably, the system is found long-term stable for at least

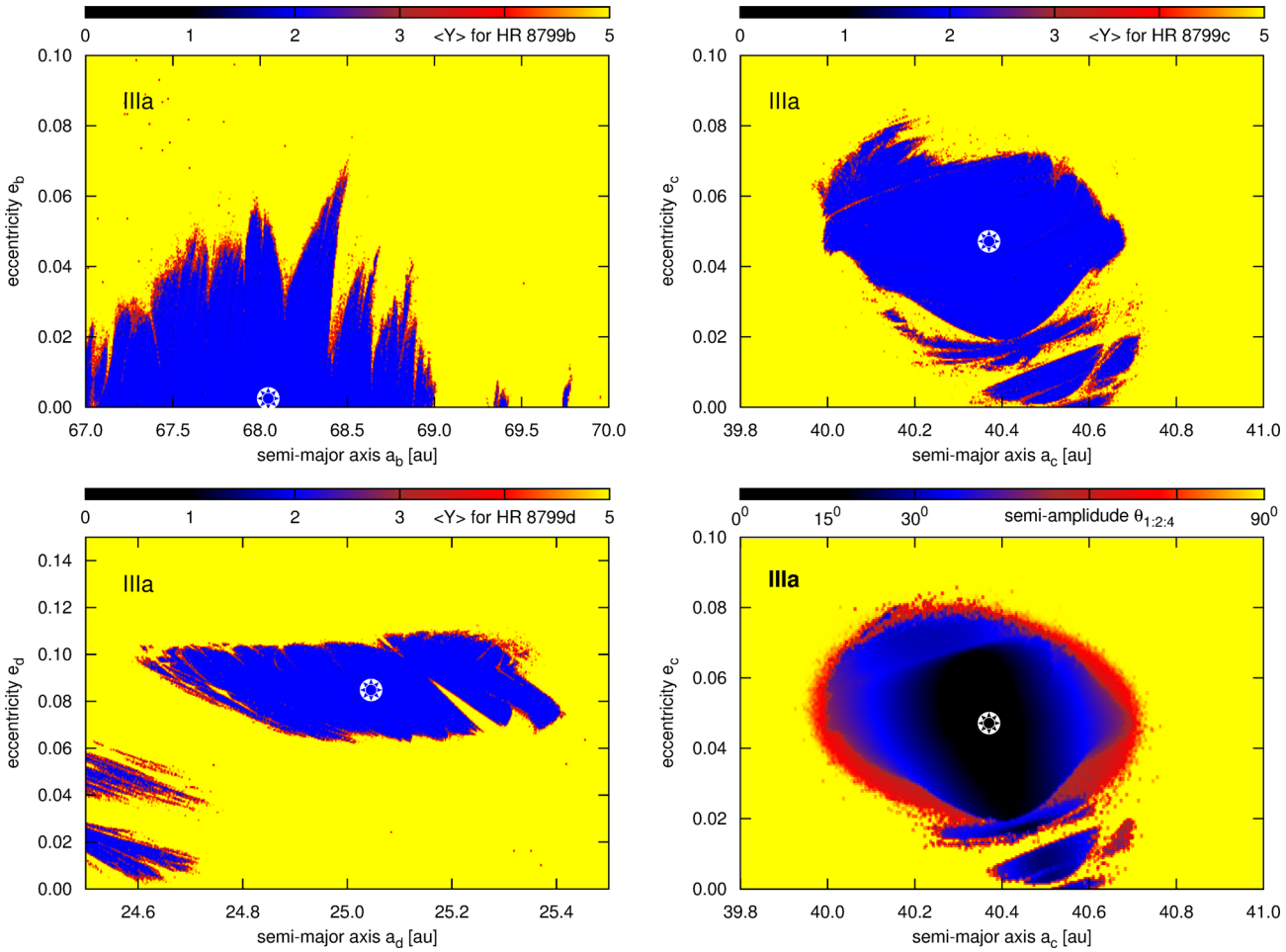

Figure 17. Dynamical maps in terms of the maximal Lyapunov exponent, expressed by the MEGNO fast indicator $\langle Y \rangle$, in the semimajor–eccentricity planes for subsequent planets in the HR 8799 system with three planets. This is the best-fitting model IIIa to astrometric data in the discovery paper (Marois et al. 2008). The bet-fitting configuration is deeply locked in the classic Laplace resonance. The semi-amplitude of this MMR around 90° is shown in the bottom-right panel.

160 Myr in quite an extended area which is much wider than the MEGNO zone of quasi-periodic, stable motions (not shown here).

4.4.2 Single-image characterization of a three-planet model

Going further, to mimic a single-image detection of three outermost planets, we chose only one, single epoch 2008.61 and three measurements for outer planets from the discovery paper (Marois et al. 2008). Epoch 2008.61 refers to the most precise measurement. We optimized a three-planet model (IIIb) with this data set D3. The results are presented on Fig. 18. Red filled circles pointed out with an arrow are for the D3 observations, while yelow/black circles mark all remaining observations (data set D5), as the reference data. The best-fitting orbits of model IIIb are plotted with black solid curves, while the dashed curves are for the best-fitting solution IVa (four-planets, full data set D1). Orbits plotted in grey have $\sqrt{\chi^2_\nu} < 1.0$. Surprisingly, even the single-epoch measurements are sufficient to constrain the orbits. Clearly, both orbital geometries closely overlap.

The stable Laplace MMR island of best-fitting model IIIb is illustrated in dynamical MEGNO map for planet HR 8799 c shown in the left-hand panel of Fig. 19. A quasi-periodic character of this solution assures us that this configuration survives for more than 160 Myr without any sign of instability. In fact, this particular solution IIIb has the MEGNO signature ∼2 after 160 Myr that guarantees its stability for times 1–2 orders of magnitude longer, for 1 Gyr or longer.

4.4.3 Single-image characterization of a four-planet model

We did a similar experiment simulating single-epoch detection of four planets (model IVc). Data set D4 which is optimized consists of most accurate four data points at epoch 2009.77 in Currie et al. (2011). The results are shown on Fig. 20 in the same manner as Fig. 18. Clearly, the best-fitting orbits derived from the full data set D1 and from a single-epoch image D4 agree amazingly well. The best-fitting solution is found in the centre of stable MMR island (the right-hand panel of Fig. 19). The double Laplace MMR lock is so robust and bounded in the orbital parameter-space that even the minimal data are sufficient to constrain its orbital configuration in space.

4.5 Model V: the fifth planet in the HR 8799 system?

The migrating HR 8799 planetary system stabilized by the MMRs might involve more planets orbiting interior to the orbit of planet e. There is a free space up to the distance ∼15 au comprising of a few

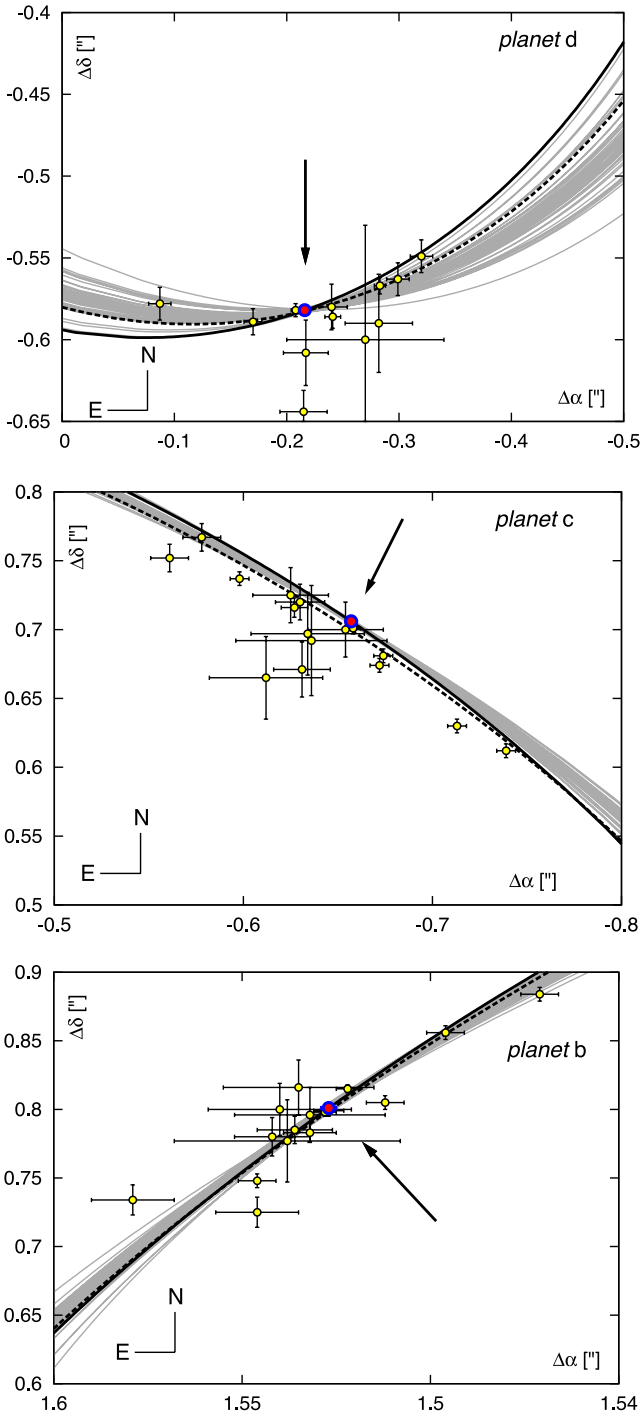

Figure 18. Relative astrometric positions $\Delta\alpha$ [arcsec] versus $\Delta\delta$ [arcsec] of the HR 8799 planets and orbital arcs for the best-fitting four-planet model IVa (black dashed curves), and for the best-fitting, single-epoch model IIIb (black solid curves). Grey curves are for model IIIb and solutions with $\sqrt{\chi^2_\nu} < 1$.

low order MMRs with planet e, like 1f:2e (∼10 au), 1f:3e (∼7.5 au), and 2f:5e (∼8.5 au). A detection of so close objects overshined by the star is certainly very difficult. The contrast requirements and angular resolution are extreme in such a case, at the technical limit of the direct imaging. The negative results of the search for the fifth planet by Skemer et al. (2012) put the upper orbit limit for the hypothetical object to 1f:2e MMR with the innermost planet, provided that this new planet has similar mass to planet e. We may note that the zone inner to ∼8 au orbit suffers from exponential degrading of the contrast (see fig. 3 in Skemer et al. 2012), and, actually, less massive and luminous object might be still present.

The results Hinkley et al. (2011) also do not exclude a low-mass object with the mass below 11 $m_{\rm Jup}$ between 0.8 and 10 au. Moreover, the warm disc gap interior to ∼6 au (Su et al. 2009; Hinkley et al. 2011; Oppenheimer et al. 2013) is incompatible with the results of simulating the lifetimes of mass-less particles in the four-planet system (our model IVa). We integrated ∼1000 probe particles placed at $a_{\rm p} \in [2, 16]$ au with initially random eccentricities $e_{\rm p} \in [0, 0.3]$ and with random orbital phases $\sim[0^\circ, 360^\circ]$. The event time $T_{\rm E}$ graph in Fig. 21 reveals that low-mass objects (large dust particles, colliding asteroids producing that dust) could survive for at least 160 Myr in the innermost zone of the system that ends at ∼6–7 au.

Note that due to random distribution of initial eccentricity, $T_{\rm E}$ cannot be uniquely determined; hence, the plot illustrates a border of stable orbits in statistical sense. To confirm this result for non-zero mass objects, we carried out much more extensive multidimensional scan in the orbital elements space. The probe mass of $\sim 0.001 m_{\rm Jup}$ was placed in orbit interior to planet HR 8799 e, with the semimajor axis $a_f \in [4.5, 10.5]$ au. Next, for each point of the pericentre argument and the mean anomaly at the grid with $3^\circ \times 3^\circ$ resolution and spanning full angle, the initial eccentricity was sampled from uniform distribution $e_f \in [0, 0.3]$. Each orbit was then MEGNO-integrated for 1 Myr. The results are shown in Fig. 22. Each point in this figure marks quasi-periodic (stable) orbit. The tested region of innermost orbits is filled with multiple MMRs. The bottom plot shows that stable MMRs are possible only for particular initial relative phases of the probe mass. Overall, interior to the ∼6–7 au his zone is basically stable, in accord with two orders of magnitude longer, direct integrations illustrated in Fig. 21. The results may be also helpful to determine possible locations of small planets in the system, below the current detection limit.

This experiment also suggest that the presence of a relatively massive object interior to planet e could further clear or sculpt dynamically the innermost debris disc.

Before examining such a hypothesis of less-massive fifth planetary object, we carefully verified that the migration algorithm 'predicts' correctly planet e. We would like to recall that the observational circumstances were easily simulated by optimizing four-planet model to all observations of only three outer planets d, c, and b (data set D5). Indeed, the best-fitting simulated configuration found the 'missing' planet e perfectly in place of the actual detection. Moreover, stability constraints even narrow possible outcomes of MCOA to agree with the best-fitting, nominal four-planet model IVa (see Figs 12–14).

We carried out a similar experiment regarding yet unseen, hypothetical innermost planet f. An extension of model IVb to five planets is quite straightforward. This model V combines the full data set D1 with a five-planet system. The simulated mass range of planet f is assumed similar to planet e, around 6 $m_{\rm Jup}$ with a significant dispersion $\pm 4\ m_{\rm Jup}$.

The results of more than 10^5 single runs of MCOA are illustrated in Figs 23–25. Fig. 23 illustrates the sky-plane geometry of the statistics of solutions within 6σ confidence level. Fig. 24 shows the osculating elements and masses of the hypothetical planet projected on to the planes of the semimajor axis – eccentricity (the left-hand panel) and on to the semimajor axis – mass (the right-hand panel). The measurements are consistent with two MMRs chains resulting in similar $\sqrt{\chi^2_\nu} \sim 1.18$ – the five-planet *triple* Laplace

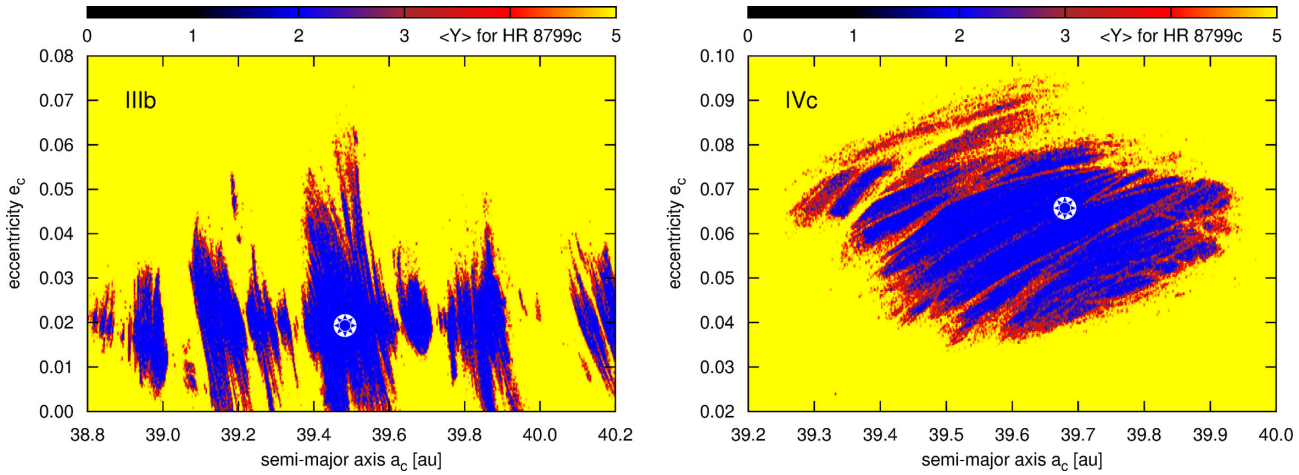

Figure 19. Dynamical maps in terms of the MEGNO $\langle Y \rangle$ in the semimajor axis–eccentricity planes for planet HR 8799 c. *Left-hand* panel illustrates the best-fitting solution IIIc to only *three* data points in the discovery paper (Marois et al. 2008) mimicking a single-image detection of three outer planets. Similarly, *right-hand* panel is for the best-fitting model IVc to *four* data points in (Currie et al. 2011) that might represent a detection of four planets at single image. The star symbol marks the best-fitting model. Resolution of each map is 720 × 360 initial conditions. The integration time for each pixel is ∼10 000 orbital periods of the outermost planet (≃5 Myr).

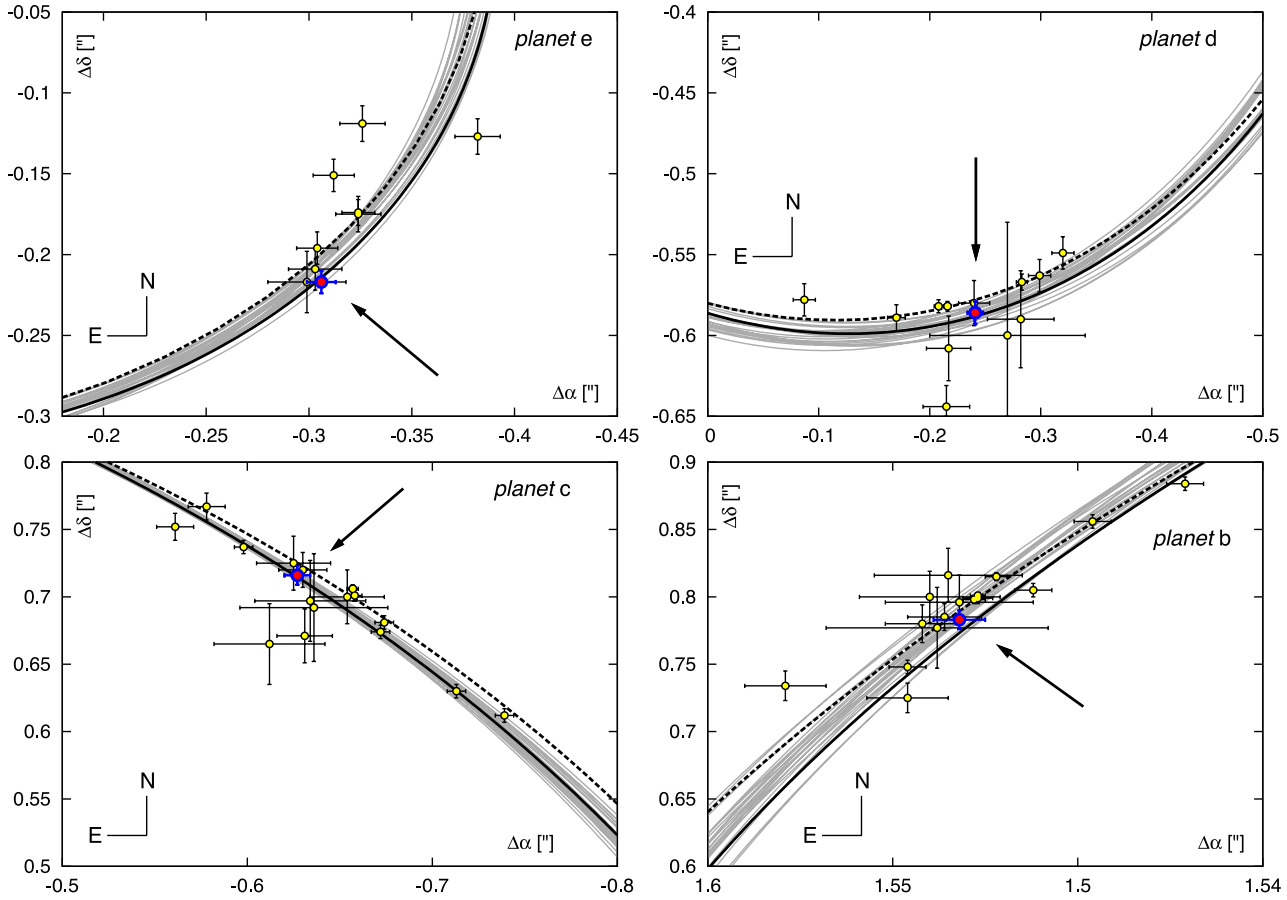

Figure 20. Relative astrometric positions $\Delta\alpha$ [arcsec] versus $\Delta\delta$ [arcsec] of planets and orbital arcs for the best-fitting four-planet models IVa (black dashed curves), and for the best-fitting single-epoch model IVc (black solid curves). Grey curves are for solutions IVc with formal $\sqrt{\chi^2_\nu} < 1$.

resonance, 1f:2e:4d:8c:16b MMR, and the five-planet 1f:3e:6d:12e:24b MMR, which we refer to as the 1f:2e MMR and the 1f:3e MMR for short, respectively. A multiple MMR comprising of the 2f:5e MMR combined with double Laplace MMR of four outer planets is also possible but this solution has significantly larger $\sqrt{\chi^2_\nu} \sim 1.25$.

Each of the two dominant MMRs appears as two well-bounded families of orbits which are differently phase-spaced. These families

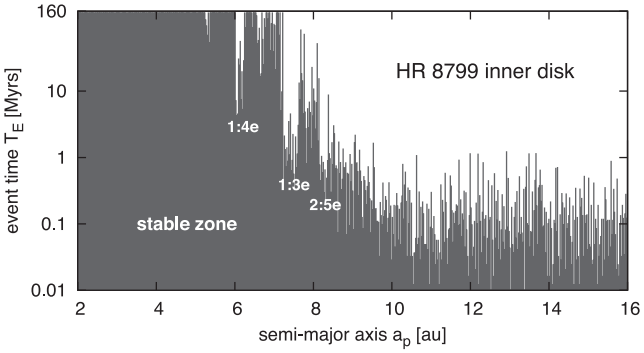

Figure 21. Statistical event times T_E for mass-less particles in the inner zone of the HR 8799 four planet model IVa. Particles placed interior to ∼7 au with random eccentricities $e_p \in [0, 0.5]$ and random orbital phases survive for at least 160 Myr.

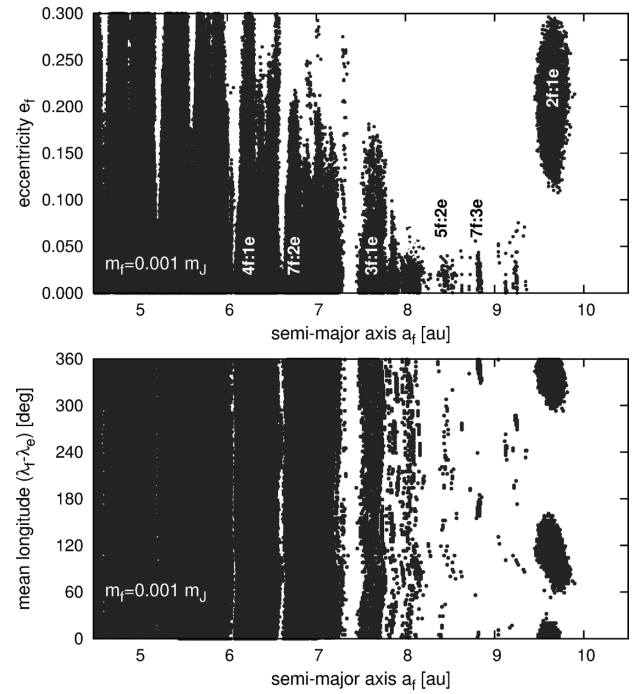

Figure 22. A simulation of stable regions in the semimajor axis versus eccentricity plane (*top*) and in the semimajor versus relative orbital phase plane (*bottom*) for hypothetical massive, Mars-like asteroids ∼0.001m_{Jup}. Low-order two-body MMRs with planet HR 8799 e are labelled. Each dot represent a quasi-periodic, stable orbit for orbital phase illustrated in the bottom panel. The MEGNO integration time of 1 Myr is equal to ∼20 000 orbital periods of planet HR 8799 e. Black filled circles are for stable orbits. See the text for details.

are distinguished by particular critical argument of the MMR. We call them Va (1f:3e MMR with $\sqrt{\chi^2_\nu} \sim 1.176$), Vb (1f:3e MMR with $\sqrt{\chi^2_\nu} \sim 1.177$), Vc (1f:2e MMR with $\sqrt{\chi^2_\nu} \sim 1.169$), and Vd (1f:2e MMR with $\sqrt{\chi^2_\nu} \sim 1.25$) from hereafter (see also Table 5 and ephemeris tables, Tables B2–B5 for all models). We note that the outer planets are always involved in a double Laplace resonance, 1e:2d:4c:8b MMR.

Overall, the best-fitting mass ranges of the putative fifth planet seem well correlated with the MMR type. The triple Laplace MMR favours planets with ∼1–4 m_{Jup}, while stable 1f:3e MMR solutions permits the masses much larger, ∼2–8 m_{Jup} (see the right-hand panel in Fig. 24).

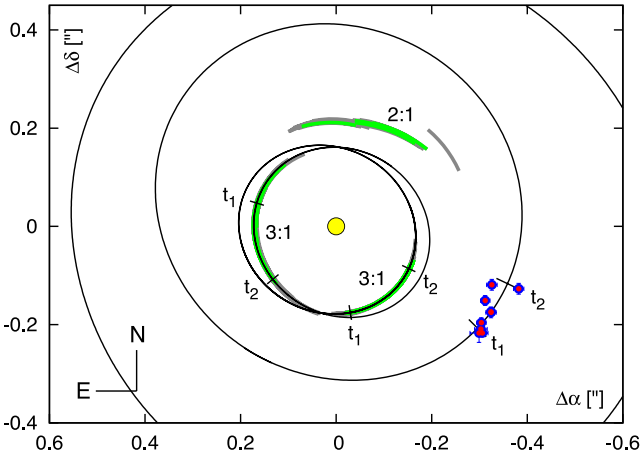

Figure 23. Observations of planet e (red/blue filled circles) overplotted on best-fitting orbits of planets e and f in model Va (black solid curves). Orbital arcs of planet f between epochs 2009.58 and epoch 2011.86 are plotted with solid grey curves ($\sqrt{\chi^2_\nu} < 1.5$, equivalent to 6σ solutions) and with green curves ($\sqrt{\chi^2_\nu} < 1.3$). Arcs of stable orbits within 3σ confidence interval are marked with tics.

We tested the long-term stability of ∼2000 solutions within 6σ confidence interval of the best solutions with $\sqrt{\chi^2_\nu} \sim 1.18$, by integrating MEGNO for 160 Myr. The results of detailed dynamical analysis combined with $\sqrt{\chi^2_\nu}$ seems to narrow the likely positions of planet f to basically four well-bounded locations. The dynamical maps computed for lowest $\sqrt{\chi^2_\nu}$ solutions in each family are illustrated in Fig. 26. Except for the 1f:2e MMR model Vc, these solutions are found in the centres of islands of long-term stable motions. Models Va, Vb, and Vd are long-term stable. For a reference, the orbital architecture of model Va (a family of the 1f:3e MMR) for 160 Myr is illustrated in Fig. 27. This plot marks also the inner, thin disc of the habitable zone extending roughly to ∼4 au, interior to the orbit of planet f. The region inner to orbit of planet e may contain a warm debris disc detected by *Spitzer* (Reidemeister et al. 2009; Su et al. 2009). The dynamical structure of this region is certainly very complex. We postpone its analysis to a future paper.

The Vc solution (1f:2e MMR) is found as marginally stable. This is confirmed by Fig. 28 which illustrates the MEGNO behaviour for this model, as compared to the rigorously stable model Va. The best-fitting configuration disrupts after ∼120 Myr, although is found at the edge of quite extended stability zone (see also the T_E dynamical map in Fig. 30 and a discussion in Section 5).

Our predictions do not contradict a negative result of the search for the fifth planet in Skemer et al. (2012). For instance, the 1f:3e MMR orbits are systematically closer to the star than the 1f:2e MMR orbits (see Fig. 25). At distances ∼8 au the contrast of LBT images drops exponentially, see figs 3 in Skemer et al. (2012) and in Esposito et al. (2013). We also note that the 1f:2e MMR models systematically tend to low masses of ∼2–3 m_{Jup}; hence, the object would have much lower luminosity than Skemer et al. (2012) tested on fake images.

In all examined models, the resonance islands span up to ∼0.1 au, hence are extremely narrow when compared with the overall dimension of the system (∼100 au). This is a clear warning that a search for the fifth planet with the common, 'traditional' optimization methods would be difficult and unlikely possible due to large number of free parameters and narrow observational window. With the help of MCOA, planet f may be 'pre-detected' without

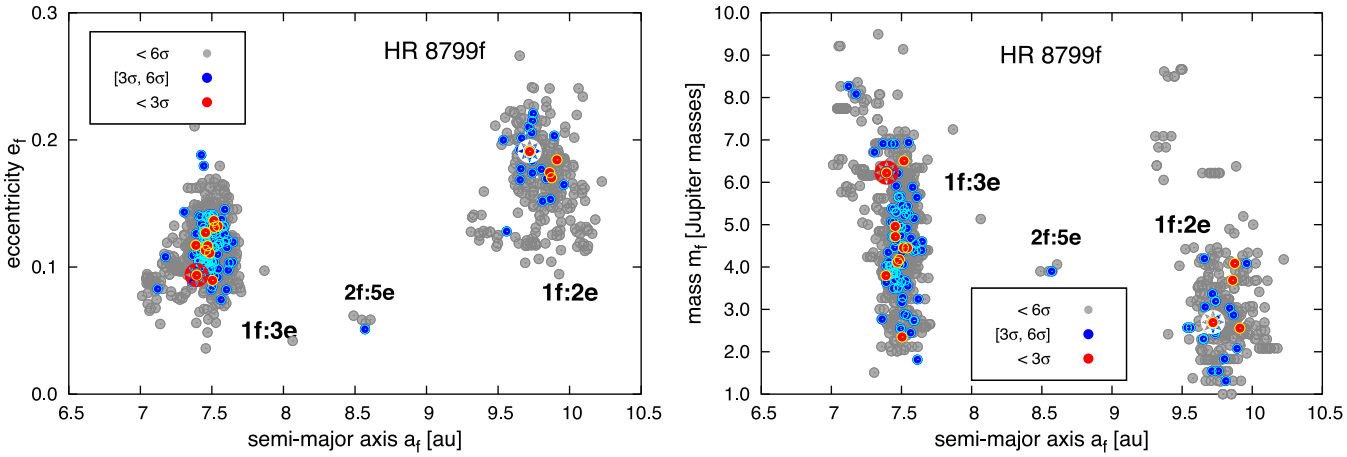

Figure 24. Orbital parameters of the five-planet model V regarding yet unseen, hypothetical planet HR 8799 f. These parameters are projected on to semimajor axis – eccentricity (*left*) and the semimajor axis – mass (*right*) planes of this planet, respectively. The red and white star symbols mark the nominal, best-fitting solutions that correspond to distinct families of these models: the 3f:1e MMR ($\sqrt{\chi^2_\nu} = 1.176$) and 2f:1e MMR ($\sqrt{\chi^2_\nu} = 1.169$), respectively. Grey circles are for all (also unstable) solutions with $\sqrt{\chi^2_\nu} < 1.5$. Compare these results with simulations of the stability of less-massive objects interior to planet e, shown in Fig. 22.

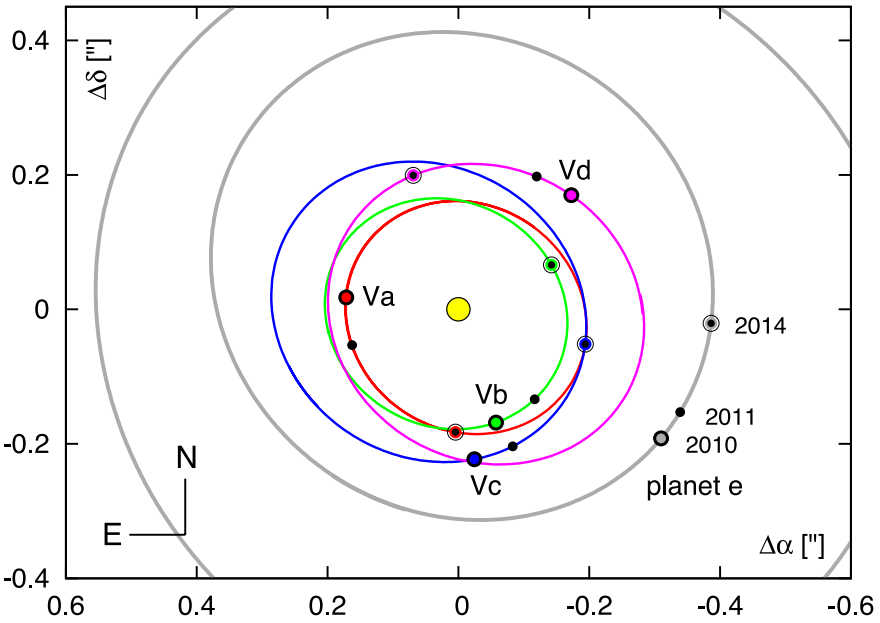

Figure 25. Best-fitting orbits Va (1f:3e MMR), Vb (1f:3e MMR), Vc (1f:2e MMR), and Vd (1f:2e MMR) of planets e and hypothetical planet f. Orbital positions of both planets at epochs 2010.0, 2011.0, and 2014.0 are marked with filled circles and labelled, accordingly. See also ephemeris Tables B2–B5.

even seen it first at the images. The predictions and ephemeris data (Tables B2–B5) might be helpful to confirm or withdraw this intriguing hypothesis.

5 DYNAMICAL STABILITY AND NUMERICAL SETUP

A marginal dynamical stability of HR 8799 system is a common problem highlighted in the literature. Similarly to most papers published so far, we solved numerically the Newtonian, *N*-body equations of motion to track the dynamical evolution of particular best-fitting solutions. The results of stability analysis in the same dynamical framework may be then easily compared with the previous studies.

Planets and the host star in our numerical experiments are approximated by point masses. The estimated system age in the range of [30, 160] Myr (Marois et al. 2010) is equivalent to [6, 32] $\times$ 10^4 orbital periods of the outermost planet. In such time-scales, the short-term dynamics is governed by low-order MMRs. Our dynamical model neglects the general relativity, as well as conservative and dissipative tidal body–body interactions. Such perturbations are scaled with large negative powers of semimajor axes (e.g. Migaszewski 2012, and references therein). We also do not include tidal interactions of the planets with two remnant discs. In the recent paper, Moore & Quillen (2013) show that the outer disc might influence the system stability. However, their *N*-body four-planet model is marginally stable only for a few Myr. We postpone a similar study making use of updated initial conditions of the HR 8799 system to another work.

Table 5. Osculating elements and masses for the best-fitting five-planet models. The stellar mass $m_0 = 1.56\,\mathrm{M}_\odot$. The osculating epoch is 1998.83.

Model	Planet	$\sqrt{\chi^2_\nu}$	$m\,(m_{\rm Jup})$	a (au)	e	I(deg)	Ω(deg)	ω (deg)	$\mathcal{M}_0$ (deg)
	f		6.218 270	7.393 497	0.093 498			162.267 947	143.405 566
	e		7.620 773	15.809 728	0.153 788			290.348 791	328.757 318
Va	d	1.176	7.818 042	26.006 470	0.124 417	25.542 107	243.667 749	215.954 602	49.813 246
	c		8.749 394	39.680 175	0.049 666			272.353 696	142.869 706
	b		4.585 532	68.187 050	0.016 927			253.022 770	279.634 792
	f		4.959 466	7.454 967	0.113 033			51.797 812	23.180 967
	e		7.785 460	15.466 841	0.170 185			290.256 931	322.820 611
Vb	d	1.177	9.496 197	25.529 862	0.125 842	26.869 698	245.474 714	205.284 684	57.312 742
	c		8.852 039	40.465 447	0.037 989			274.813 041	139.910 933
	b		5.169 680	69.434 385	0.020 676			174.060 193	354.774 655
	f		2.691 369	9.720 335	0.190 823			221.621 749	116.829 209
	e		6.887 347	15.804 942	0.183 061			113.782 165	326.274 813
Vc	d	1.169	8.425 855	25.747 574	0.144 288	27.627 645	59.952 718	35.857 501	50.193 242
	c		9.448 184	39.984 360	0.061 401			93.794 336	145.271 020
	b		7.707 015	69.811 606	0.027 531			17.258 200	338.762 294
	f		4.197 927	9.659 082	0.177 303			201.043 842	80.245 495
	e		6.698 260	15.660 910	0.168 239			290.074 917	324.850 32
Vd	d	1.252	7.178 005	25.705 213	0.137 796	25.568 815	243.953 507	213.186 128	50.262 837
	c		11.868 008	39.486 207	0.054 102			269.946 387	145.097 451
	b		6.527 020	68.597 249	0.017 425			217.631 852	314.164 304

The conservative, Newtonian N-body model permits to introduce at least two notions of the dynamical stability. The direct, long term numerical integrations make it possible to investigate the Lagrange or astronomical stability. The astronomical stability may be expressed by the event time $T_{\rm E}$ of a collision between planets (orbits crossing) or an ejection of a body from the system. The direct 160 Myr integrations of the equations of motion for one initial condition of five-planet system require CPU time counted in hours. Such a significant CPU overhead is not suitable to illustrate the global dynamics of the system.

Stability of planetary configurations may be also expressed through the MLCE λ. The MLCE is a fundamental measure of the divergence of initially close trajectories in the phase space. A non-zero value of MLCE indicates a chaotic (unstable) system. Chaotic motions in a regime of strong, low-order MMRs may lead to short event times (e.g. Goździewski et al. 2008b). To compute MLCE, we use an effective algorithm of the MEGNO $\langle Y\rangle$ Cincotta & Simó (2000); Cincotta et al. (2003). A uniform definition of this fast indicator describes two basic classes of motions in the phase space:

$$\lim_{t\to\infty}\langle Y(t)\rangle = \frac{1}{2}\lambda t + d,$$

where for the regular, stable quasi-periodic solutions $\lambda = 0$, $d \simeq 2$, and for chaotic (unstable solutions) $\lambda > 0$ and $d \simeq 0$. MLCE measures the slope of linear function for the chaotic solutions, hence an approximation of MLCE after time t:

$$\lambda(t) \sim 2\frac{\langle Y(t)\rangle}{t}.$$

This technique requires relatively short arcs of the phase space trajectories, equivalent to a few of 10^4 orbital periods of the outermost planet (characteristic periods; let us recall that 10^4 outermost orbital periods of HR 8799 b translates to roughly 5 Myr). This makes it possible to construct high-resolution dynamical maps in selected planes of orbital parameters with much smaller CPU overhead than required by the direct N-body integrations.

There is no simple nor uniform relation between the MLCE and the event time. We performed a number of experiments to calibrate a link between the MEGNO interval and the direct integration time.

To examine the dynamical stability of isolated best-fitting models gathered in Figs 7, 8, 12, 14, and 16, we computed MEGNO for the upper limit of the system age (160 Myr). To conserve the total energy and angular momentum with the relative accuracy $\sim 10^{-9}$, we apply the tangent map algorithm (Goździewski et al. 2008a) that makes use of the fourth-order $\mathcal{SABA}_4$ symplectic integration scheme (Laskar & Robutel 2001). Step sizes of the symplectic tangent mapping are usually 256 or 384 d for the four-planet configurations and 128 or 256 d for the five-planet configurations. We verified these settings with an accurate but 2–3 times less CPU-effective Bulirsh–Stoer–Gragg scheme (the ODEX code; Hairer, Norsett & Wanner 1993).

A typical convergence of MEGNO indicating strictly quasi-periodic best-fitting model IVa is shown in the left-hand panel of Fig. 28. The right-hand panel compares two other solutions corresponding to five-planet models Va and Vc, labelled with 1f:3e and 1f:2e, accordingly (see their orbital geometry in Fig. 25 and elements in Table 5). The MEGNO convergence of the 1f:3e solution Va is similarly perfect for 100 Myr. This is not the case for the 1f:2e MMR solution Vc. After ~15–20 Myr, the indicator starts to grow roughly on a linear rate indicating a weakly chaotic configuration. The direct N-body integration shows that this system disrupts due to crossing orbits after ~120 Myr. This illustrates a well-known instability due to secular interactions in multiple MMRs (e.g. Murray & Holman 2001; Guzzo 2005; Goździewski et al. 2008a; Quillen 2011). A proper choice of the integration time to compute MLCE is a delicate matter (Sussman & Wisdom 1992).

To resolve the structure of the phase space, and to measure the width of MMRs, we computed a number of dynamical MEGNO maps. The MEGNO integration time was set to ~5–12 Myr, which is equivalent to ~10 000–25 000 characteristic periods. We carefully

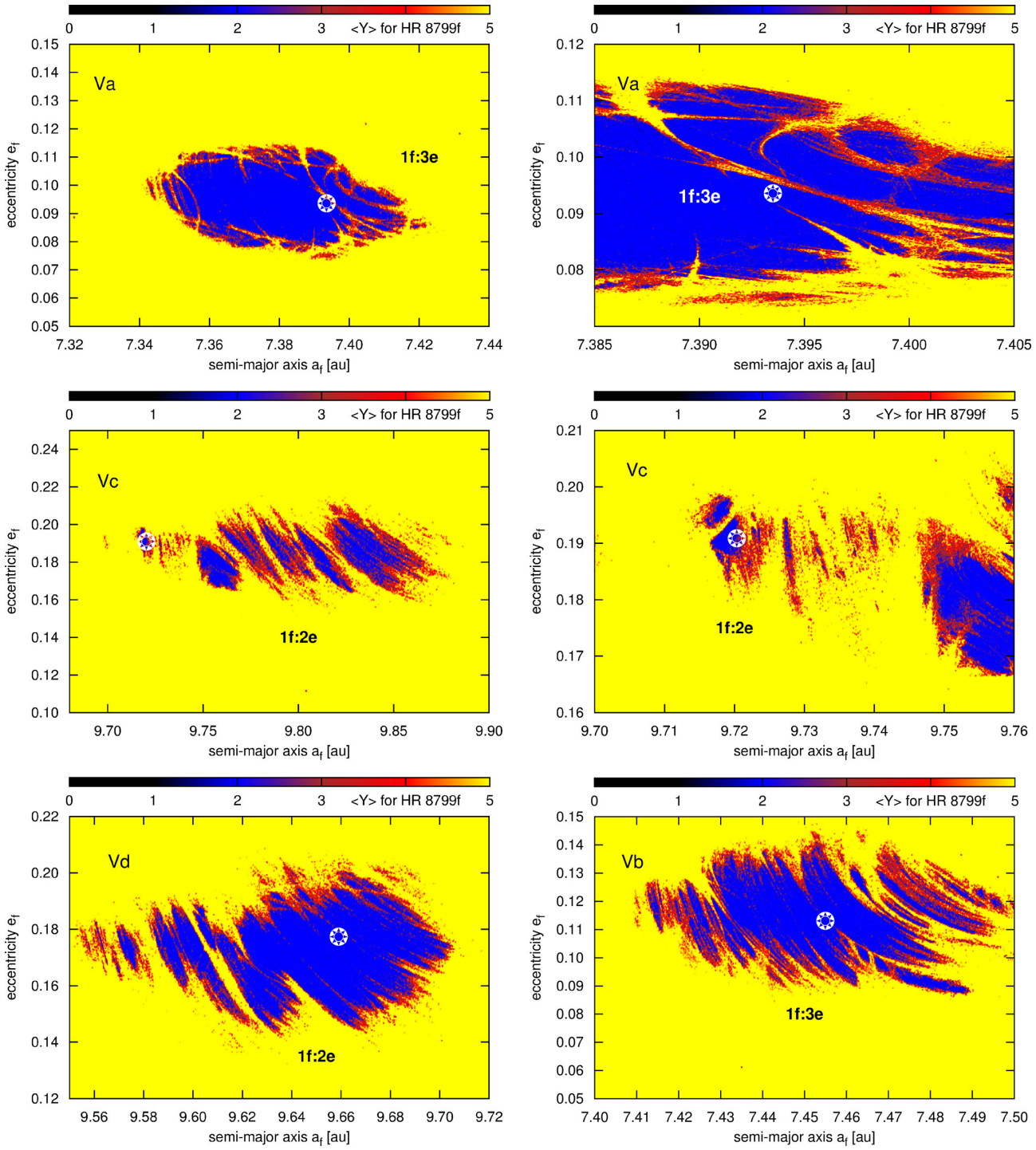

Figure 26. Dynamical maps $\langle Y \rangle$, in the semimajor–eccentricity plane for the best-fitting five-planet models including a hypothetical planet HR 8799 f. This planet might be involved in the 1e:3f MMR, or in the 1f:2e MMR with planet HR 8799 e. The star symbol marks the best-fitting models in Table 5 (subsequent plots are labelled accordingly), see also Fig. 25. Two upper right-hand panels are for close-ups of solutions Va and Vc with smallest $\sqrt{\chi^2_\nu}$. The resolution of all maps is 640 × 320 pixels. The integration time for each pixel is ∼20 000–30 000 orbital periods of the outermost planet (≃10–15 Myr).

validated this choice. The MEGNO maps in the (a_c, e_c)-plane for the best-fitting four-planets model IVa (Fig. 9), and the five-planet models Va and Vc (Fig. 26) were compared with the event time maps in Figs 29 and 30. In the MEGNO maps, similar to all such maps in the text, stable, quasi-periodic solutions with $\langle Y \rangle \simeq 2$ are always marked in blue. Yellow colour encodes strongly unstable (chaotic) models with $\langle Y \rangle \geq 5$, as usually the integrations were stopped if $\langle Y \rangle \geq 5$. Intermediate values of MEGNO between 2 and 5 correspond to chaotic solutions too.

For the event time maps in Fig. 29 (top-left panel) and Fig. 30, the equations of motions were integrated for the maximum time span of 160 Myr. Maps in the top-right and bottom-left panels of Fig. 29

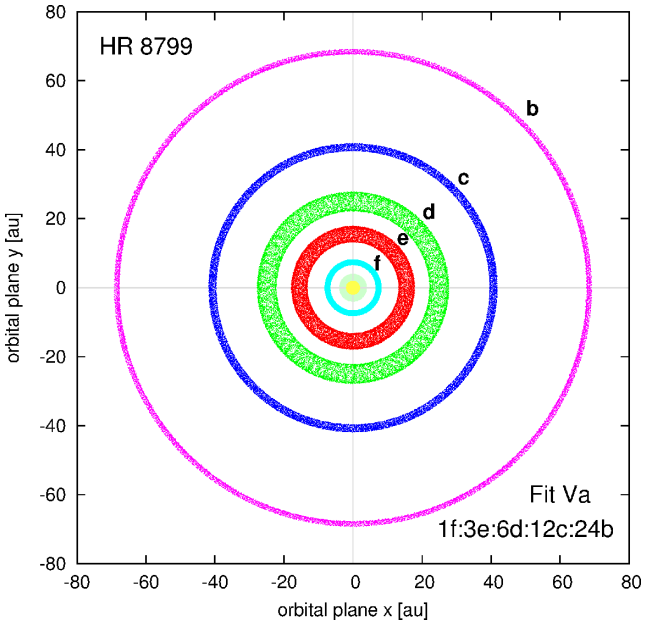

Figure 27. The orbital architecture of the HR 8799 system, in accord with the best-fitting, coplanar, and long-term stable model Va of *five* planets involved in the 1f:3e:6d:12e:24b MMR. This solution results in $\sqrt{\chi^2_\nu} = 1.176$ and its osculating elements are given in Table 5. The new planet would be in the 1e:3f MMR with HR 8799 e. Orbital positions of HR 8799 planets are shown for 160 Myr in the astrocentric coordinate frame, coplanar with the orbits. The innermost green circle in the centre has the radius of ∼4 au and corresponds to the outer edge of the habitable zone in the HR 8799 system.

were integrated for longer intervals. In this way, three subsequent panels in Fig. 29 are for gradually increased limit of the integration time from 160 Myr (top-left panel), to 500 Myr (top-right panel) and 1 Gyr (bottom-left panel). We may observe that the maximal $T_{\rm E}$ zone shrinks with the longer integration times. However, the boundary of $T_{\rm E}$ map for 1 Gyr perfectly matches the boundary of quasi-periodic motions in the MEGNO map (see the top-right panel in Fig. 9). This experiment assures us that initial conditions of four-planet models identified with MEGNO as quasi-periodic for time $T \sim 10$ Myr (typical integration period of MEGNO) may be safely considered as astronomically stable for $\sim 10^2 T$ that translates to ∼1 Gyr interval encompassing all current estimates of the HR 8799 lifetime. This estimate for five-planet systems might be too optimistic; however, the MEGNO maps match at least the $T_{\rm E}$ maps computed for the maximal time of 160 Myr.

Remarkably, a single integration of symplectic MEGNO for ∼10–15 Myr takes roughly up to 10 min of CPU per initial condition, depending on the *N*-body model, integrator, and the mapping step size. Even with such reasonable CPU overhead, a quasi-global analysis of the dynamical stability still requires significant CPU power which is inaccessible on a single workstation. For instance, a single symplectic MEGNO map in the 720 × 360 resolution occupied up to 512 CPU cores for up to 1–2 days of supercomputers `chimera` and `cane` installed in the Poznań Supercomputer Centre PCSS, Poland. To perform massive numerical experiments in this work, we applied our new CPU cluster environment `Mechanic` (Słonina, Goździewski & Migaszewski 2014) and simple codes written with the standard Message Passing Interface (MPI).

6 CONCLUSIONS

The HR 8799 is one of most exotic and intriguing extrasolar planetary systems detected so far. Any definite conclusion on its current state suffers from ambiguities concerning its formation history, age and companion masses. The astrometric data still cover only tiny arcs of the orbits and are relatively inaccurate. To overcome this problem, we invented new optimization algorithm constrained through planetary migration (MCOA). This algorithm makes it possible to derive a self-consistent dynamical model of the HR 8799 system perfectly matching all observations and independent mass estimates. This model is rigorously stable for any estimate of the star age, between 30 Myr and 1 Gyr. Our results are suggestive for the formation of all HR 8799 planets in wider orbits that migrated shortly to their observed orbits. Indeed, the signatures of an extremely massive and dense protoplanetary disc revealed by *Spitzer* observations, indicate both a rapid formation of massive planets and their common migration. Moreover, the orbits are locked into an amazingly ordered chain of double Laplace MMR 1e:2d:4c:8de. The mass ranges remain below the brown dwarf limit and confirm dynamically the planetary nature of the HR 8799 companions.

False assumptions may yield correct conclusions. However, we did not find any outcome of the MCOA that contradicts the results

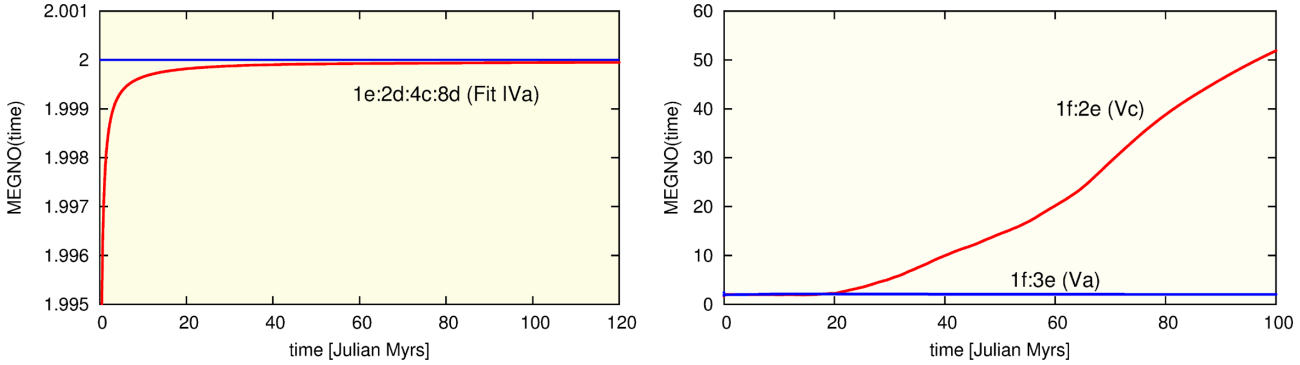

Figure 28. *Left-hand panel*: a typical convergence of the MEGNO fast indicator to 2 for a regular, quasi-periodic configuration. The initial condition corresponds to the best-fitting model IVa with four planets (Table 1). *Right-hand panel*: temporal evolution of MEGNO for the best-fitting five-planet models Va and Vb. See the dynamical maps in Fig. 28 for a reference.

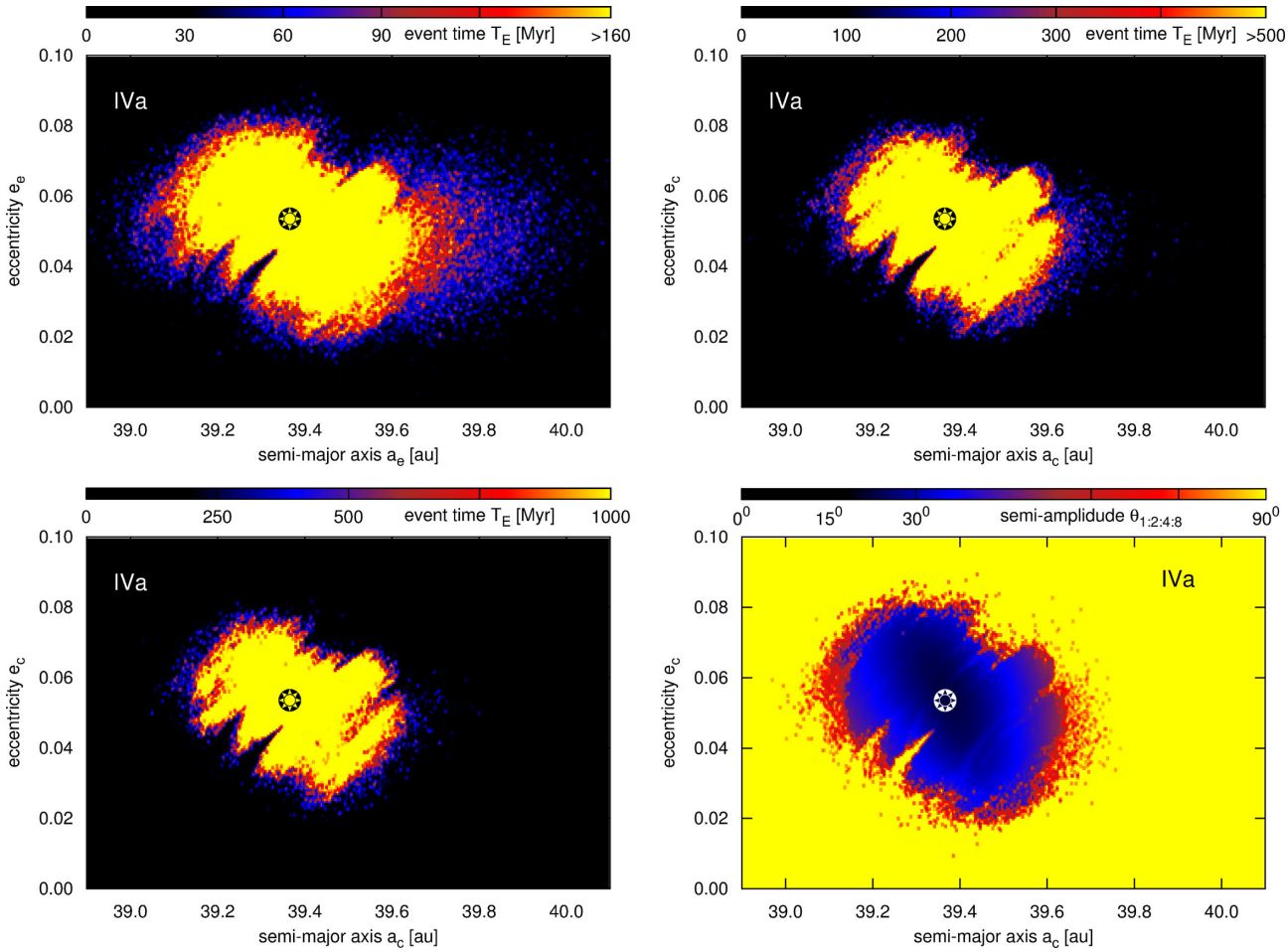

Figure 29. Event time T_E maps in the semimajor–eccentricity plane of planet HR 8799 c in the four-planet model IVa (Table 1). The maps are computed for gradually increased integration time: *top left* – 160 Myr ($\sim 3 \times 10^5$ outermost periods), *top right* – 500 Myr ($\sim 10^6$ outermost periods), *bottom left* – 1 Gyr ($\sim 2 \times 10^6$ outermost periods). The event time corresponds to orbit crossing or ejection a planet from the system and is colour-coded. Yellow colour encodes configurations lifetime is longer than the integration interval. The best-fitting system IVa marked with the star symbol is locked deeply in the 1e:2d:4c:8b MMR. The *bottom-right* panels shows the semi-amplitude of the critical angle librating around 0° in the exact resonance. The resolution of each map is 360×180 pixels.

of independent astrophysical theory. Moreover, our model of the HR 8799 system predicts basically unique ephemeris of the four- and five-planet configurations that might be verified shortly on the observational basis. A re-analysis of earlier data in the discovery paper (Marois et al. 2008) confirms the stability analysis in the literature. We found that the Laplace MMR fully consistent with the astrophysical mass estimates $\sim 10\ m_{\rm Jup}$. The dynamically determined inclination and nodal line of the system orbits closely matches independent determination of the inclination and node of the outer debris disc (Matthews et al. 2014).

We also demonstrate that MCOA is able to derive meaningful orbital characterization of a resonant system on the basis of short-interval data, essentially using a single-image detection. Our method may be useful to characterize long-period, resonant systems with massive planets detected by the direct imaging.

The migration mechanism and resonance trapping is likely responsible, although in quite smaller scale when concerning the orbits and planetary masses, for creating multiple systems of super-Earth planets discovered by the *Kepler* mission (Borucki & Koch 2011; Batalha 2013). A significant sample of *Kepler* systems involving four and more planets are found very close to multiple MMRs which might be also explained by a common, inward migration (Migaszewski, Goździewski & Słonina 2013, and references therein).

The early dynamical models of the three-planet HR 8799 system configurations indicated marginally stable, chaotic system. After the discovery of the fourth planet, these models become apparently even more unstable. In contrast, our new models derived with the migration constraints, and comprising of even five giant planets are suggestive for a completely ordered configuration which could be stable forever, if no significant perturbations are introduced.

ACKNOWLEDGEMENTS

Many thanks to Daniel Fabrycky for a review and comments that improved this manuscript. This work was supported by the Polish Ministry of Science and Higher Education, Grant N/N203/402739. CM is a recipient of the stipend of the Foundation for Polish Science (programme START, editions 2010 and 2011). This research was supported by computational resources provided through the

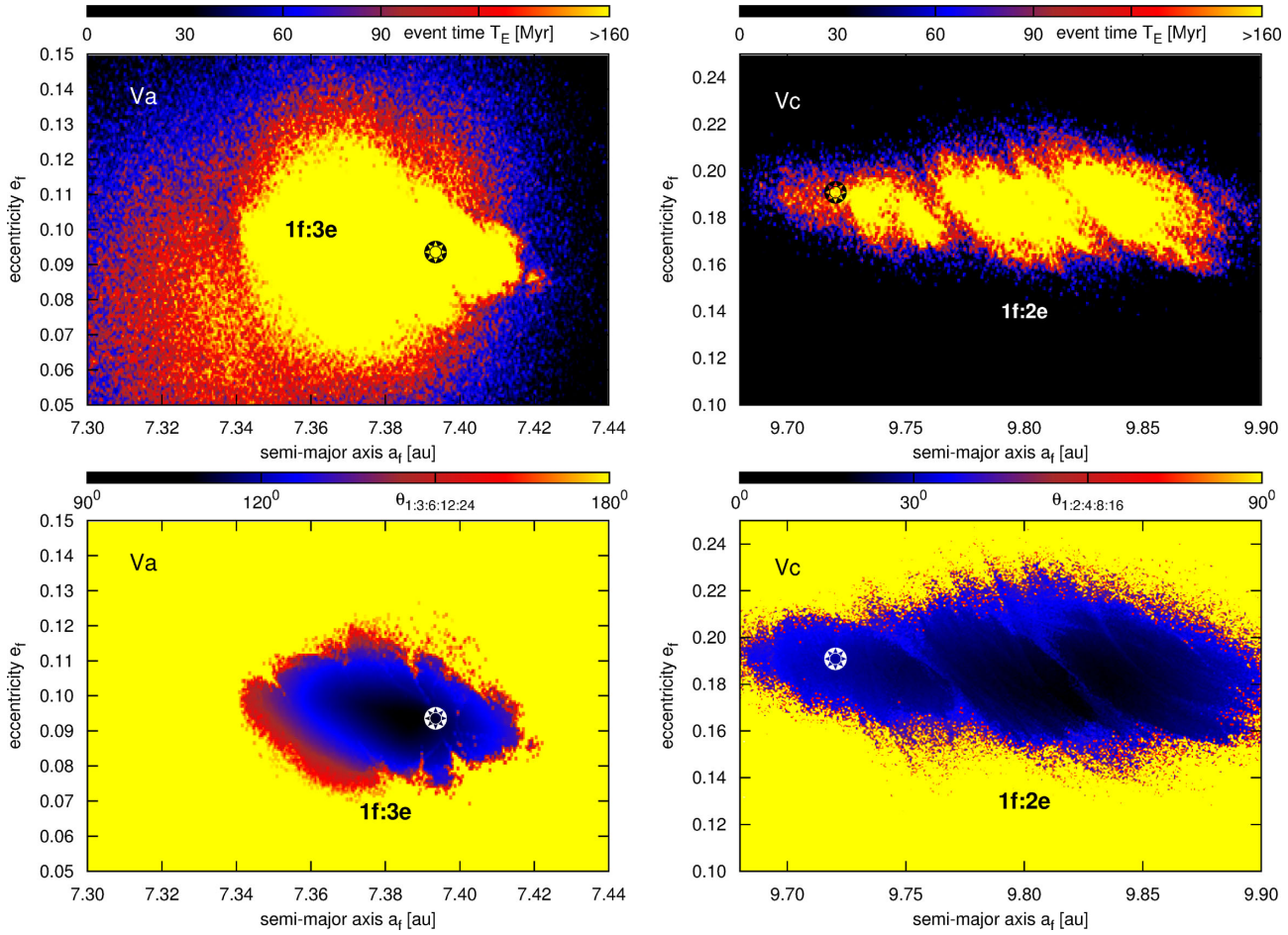

Figure 30. Event time T_E and critical angle θ maps in the semimajor axis–eccentricity plane for planet HR 8799 f in five-planet models Va (*left-hand column*) and Vc (*right-hand column*). *Top row*: the event time corresponds to orbit crossing or ejection a planet from the system and is colour-coded. The resolution of each map is 360 × 180 pixels. The maximal integration time for each pixel is 160 Myr (3.2×10^5 characteristic periods). *Bottom row*: semi-amplitude of the critical angles $\theta_{1:\,3:\,6:\,12:\,24} = \lambda_f - 4\lambda_e + 2\lambda_d - \lambda_c + 2\lambda_b$ (which librates around 90°, *left*) and $\theta_{1:\,3:\,6:\,12:\,24} = \lambda_f - 3\lambda_e + 3\lambda_d - 3\lambda_c + 2\lambda_b$ (which librates around ≈15°, *right*), respectively. The best-fitting systems Va and Vc are marked with the star symbol (see their elements in Table 5).

POWIEW project, co-financed by the European Regional Development Fund under the Innovative Economy Operational Programme (POIG.02.03.00-00-018/08).

REFERENCES

Baines E. K. et al., 2012, ApJ, 761, 57
Baraffe I., Chabrier G., Barman T. S., Allard F., Hauschildt P. H., 2003, A&A, 402, 701
Baruteau C., Meru F., Paardekooper S.-J., 2011, MNRAS, 416, 1971
Batalha N. M. et al., 2013, ApJS, 204, 24
Bergfors C., Brandner W., Janson M., Köhler R., Henning T., 2011, A&A, 528, A134
Bhattacharjee Y., Clery D., 2013, Science, 340, 566
Borucki W. J., Koch D. G., 2011, in Sozzetti A., Lattanzi M. G., Boss A. P., eds, Proc. IAU Symp. 276, The Astrophysics of Planetary Systems: Formation, Structure, and Dynamical Evolution. Cambridge Univ. Press, Cambridge, p. 34
Chambers J. E., Wetherill G. W., Boss A. P., 1996, Icarus, 119, 261
Chatterjee S., Ford E. B., Matsumura S., Rasio F. A., 2008, ApJ, 686, 580
Chen C. H. et al., 2006, ApJS, 166, 351
Cincotta P. M., Simó C., 2000, A&AS, 147, 205
Cincotta P. M., Giordano C. M., Simó C., 2003, Physica D, 182, 151
Currie T. et al., 2011, ApJ, 729, 128
Currie T., Fukagawa M., Thalmann C., Matsumura S., Plavchan P., 2012, ApJ, 755, L34
Esposito S. et al., 2013, A&A, 549, A52
Fabrycky D. C., Murray-Clay R. A., 2010, ApJ, 710, 1408
Fukagawa M., Itoh Y., Tamura M., Oasa Y., Hayashi S. S., Fujita Y., Shibai H., Hayashi M., 2009, ApJ, 696, L1
Galicher R., Marois C., Macintosh B., Barman T., Konopacky Q., 2011, ApJ, 739, L41
Goździewski K., Migaszewski C., 2009, MNRAS, 397, L16
Goździewski K., Migaszewski C., Musieliński A., 2008a, in Sun Y.-S., Ferraz-Mello S., Zhou J.-L., eds, Proc. IAU Symp. 249, Exoplanets: Detection, Formation and Dynamics. Cambridge Univ. Press, Cambridge, p. 447
Goździewski K., Breiter S., Borczyk W., 2008b, MNRAS, 383, 989
Guzzo M., 2005, Icarus, 174, 273
Hairer E., Norsett S. P., Wanner G., 1993, Solving Ordinary Differential Equations I. Nonstiff Problems. Springer-Verlag, Berlin
Hinkley S., Carpenter J. M., Ireland M. J., Kraus A. L., 2011, ApJ, 730, L21
Hinz P. M., Rodigas T. J., Kenworthy M. A., Sivanandam S., Heinze A. N., Mamajek E. E., Meyer M. R., 2010, ApJ, 716, 417
Howard A. W., 2013, Science, 340, 572

Hughes A. M., Wilner D. J., Andrews S. M., Williams J. P., Su K. Y. L., Murray-Clay R. A., Qi C., 2011, ApJ, 740, 38
Kaye A. B., Strassmeier K. G., 1998, MNRAS, 294, L35
Konopacky Q. M., Macintosh B., Fabrycky D., Marois C., Barman T., 2011, in AAS/Division for Extreme Solar Systems Abstracts, Vol. 2, Orbital Properties of the HR 8799 Planetary System. Am. Astron. Soc., Washington, DC, p. 705
Kratter K. M., Murray-Clay R. A., Youdin A. N., 2010, ApJ, 710, 1375
Lafrenière D., Marois C., Doyon R., Barman T., 2009, ApJ, 694, L148
Laskar J., Robutel P., 2001, Celest. Mech. Dyn. Astron., 80, 39
Laughlin G., Chambers J. E., 2001, ApJ, 551, L109
Marleau G.-D., Cumming A., 2014, MNRAS, 437, 1378
Marois C., Macintosh B., Barman T., Zuckerman B., Song I., Patience J., Lafrenière D., Doyon R., 2008, Science, 322, 1348
Marois C., Zuckerman B., Konopacky Q. M., Macintosh B., Barman T., 2010, Nature, 468, 1080
Marshall J., Horner J., Carter A., 2010, Int. J. Astrobiol., 9, 259
Matthews B., Kennedy G., Sibthorpe B., Booth M., Wyatt M., Broekhoven-Fiene H., Macintosh B., Marois C., 2014, ApJ, 780, 97
Metchev S., Marois C., Zuckerman B., 2009, ApJ, 705, L204
Migaszewski C., 2012, Celest. Mech. Dyn. Astron., 113, 169
Migaszewski C., Goździewski K., Słonina M., 2013, MNRAS, 436, L25
Moore A., Quillen A. C., 2013, MNRAS, 430, 320
Moro-Martín A., Malhotra R., Bryden G., Rieke G. H., Su K. Y. L., Beichman C. A., Lawler S. M., 2010, ApJ, 717, 1123
Murray N., Holman M., 2001, Nature, 410, 773
Oppenheimer B. R. et al., 2013, ApJ, 768, 24
Papaloizou J. C. B., Terquem C., 2006, Rep. Prog. Phys., 69, 119
Patience J. et al., 2011, A&A, 531, L17
Perryman M., 2011, The Exoplanet Handbook. Cambridge Univ, Press, Cambridge
Quillen A. C., 2011, MNRAS, 418, 1043
Reidemeister M., Krivov A. V., Schmidt T. O. B., Fiedler S., Müller S., Löhne T., Neuhäuser R., 2009, A&A, 503, 247
Royer F., Zorec J., Gómez A. E., 2007, A&A, 463, 671
Skemer A. J. et al., 2012, ApJ, 753, 14
Słonina M., Goździewski K., Migaszewski C., 2014, preprint (arXiv:1401.6344)
Soummer R., Brendan Hagan J., Pueyo L., Thormann A., Rajan A., Marois C., 2011, ApJ, 741, 55
Su K. Y. L. et al., 2009, ApJ, 705, 314
Sudol J. J., Haghighipour N., 2012, ApJ, 755, 38
Sussman G. J., Wisdom J., 1992, Science, 257, 56
Wahhaj Z. et al., 2013, preprint (arXiv:e-prints)
Walker G. A. H., 2012, New Astron., 56, 9
Wright D. J. et al., 2011, ApJ, 728, L20

APPENDIX A: COMPILATION OF ASTROMETRIC DATA IN THE LITERATURE

Table A1. Astrometric data in the literature for planet HR 8799 b ('s' stands for the arc second).

Epoch	Planet b		Reference	Data set				
	N (s)	E (s)		D1	D2	D3	D4	D5
1998.83	1.411 ± 0.009	0.986 ± 0.009	Lafrenière et al. (2009)	×	–	–	–	×
1998.83	1.418 ± 0.022	1.004 ± 0.020	Soummer et al. (2011)	×	–	–	–	×
2002.54	1.481 ± 0.023	0.919 ± 0.017	Fukagawa et al. (2009)	×	–	–	–	×
2004.53	1.471 ± 0.005	0.884 ± 0.005	Marois et al. (2008)	×	×	–	–	×
2005.54	1.496 ± 0.005	0.856 ± 0.005	Currie et al. (2012)	×	–	–	–	×
2007.58	1.522 ± 0.003	0.815 ± 0.003	Metchev, Marois & Zuckerman (2009)	×	–	–	–	×
2007.81	1.512 ± 0.005	0.805 ± 0.005	Marois et al. (2008)	×	×	–	–	×
2008.52	1.527 ± 0.004	0.799 ± 0.004	Marois et al. (2008)	×	×	–	–	×
2008.61	1.527 ± 0.002	0.801 ± 0.002	Marois et al. (2008)	×	×	×	–	×
2008.71	1.528 ± 0.003	0.798 ± 0.003	Marois et al. (2008)	×	×	–	–	×
2008.89	1.532 ± 0.020	0.796 ± 0.020	Currie et al. (2011)	×	–	–	–	×
2008.89	1.542 ± 0.010	0.780 ± 0.014	Hinz et al. (2010)	×	–	–	–	×
2009.62	1.536 ± 0.010	0.785 ± 0.010	Currie et al. (2011)	×	–	–	–	×
2009.70	1.538 ± 0.030	0.777 ± 0.030	Currie et al. (2011)	×	–	–	–	×
2009.76	1.535 ± 0.020	0.816 ± 0.020	Bergfors et al. (2011)	×	–	–	–	×
2009.77	1.532 ± 0.007	0.783 ± 0.007	Currie et al. (2011)	×	–	–	×	×
2009.84	1.540 ± 0.019	0.800 ± 0.019	Galicher et al. (2011)	×	–	–	–	×
2010.83	1.546 ± 0.005	0.748 ± 0.005	Currie et al. (2012)	×	–	–	–	×
2011.79	1.579 ± 0.011	0.734 ± 0.011	Esposito et al. (2013)	×	–	–	–	×
2011.86	1.546 ± 0.011	0.725 ± 0.011	Esposito et al. (2013)	×	–	–	–	×

Table A2. Astrometric data in the literature for planet HR 8799 c ('s' stands for the arc second).

Epoch	Planet c		Reference	Data set				
	N (s)	E (s)		D1	D2	D3	D4	D5
1998.83	-0.837 ± 0.026	0.483 ± 0.023	Soummer et al. (2011)	×	–	–	–	×
2004.53	-0.739 ± 0.005	0.612 ± 0.005	Marois et al. (2008)	×	×	–	–	×
2005.54	-0.713 ± 0.005	0.630 ± 0.005	Currie et al. (2012)	×	–	–	–	×
2007.58	-0.672 ± 0.005	0.674 ± 0.005	Metchev et al. (2009)	×	–	–	–	×
2007.81	-0.674 ± 0.005	0.681 ± 0.005	Marois et al. (2008)	×	×	–	–	×
2008.52	-0.658 ± 0.004	0.701 ± 0.004	Marois et al. (2008)	×	×	–	–	×
2008.61	-0.657 ± 0.002	0.706 ± 0.002	Marois et al. (2008)	×	×	×	–	×
2008.71	-0.657 ± 0.003	0.706 ± 0.003	Marois et al. (2008)	×	×	–	–	×
2008.89	-0.654 ± 0.020	0.700 ± 0.020	Currie et al. (2011)	×	–	–	–	×
2008.89	-0.631 ± 0.015	0.671 ± 0.020	Hinz et al. (2010)	×	–	–	–	×
2009.02	-0.612 ± 0.030	0.665 ± 0.030	Hinz et al. (2010)	×	–	–	–	×
2009.70	-0.625 ± 0.020	0.725 ± 0.020	Hinz et al. (2010)	×	–	–	–	×
2009.70	-0.634 ± 0.030	0.697 ± 0.030	Currie et al. (2011)	×	–	–	–	×
2009.76	-0.636 ± 0.040	0.692 ± 0.040	Bergfors et al. (2011)	×	–	–	–	×
2009.77	-0.627 ± 0.007	0.716 ± 0.007	Currie et al. (2011)	×	–	–	×	×
2009.84	-0.630 ± 0.013	0.720 ± 0.013	Galicher et al. (2011)	×	–	–	–	×
2010.83	-0.598 ± 0.005	0.737 ± 0.005	Currie et al. (2012)	×	–	–	–	×
2011.79	-0.561 ± 0.010	0.752 ± 0.010	Esposito et al. (2013)	×	–	–	–	×
2011.86	-0.578 ± 0.010	0.767 ± 0.010	Esposito et al. (2013)	×	–	–	–	×

Table A3. Astrometric data in the literature for planet HR 8799 d ('s' stands for the arc second).

Epoch	Planet d		Reference	Data set				
	N (s)	E (s)		D1	D2	D3	D4	D5
1998.83	0.133 ± 0.035	-0.533 ± 0.034	Soummer et al. (2011)	×	–	–	–	×
2005.54	-0.087 ± 0.010	-0.578 ± 0.010	Currie et al. (2012)	×	–	–	–	×
2007.58	-0.170 ± 0.008	-0.589 ± 0.008	Metchev et al. (2009)	×	–	–	–	×
2008.52	-0.208 ± 0.004	-0.582 ± 0.004	Marois et al. (2008)	×	×	–	–	×
2008.61	-0.216 ± 0.002	-0.582 ± 0.002	Marois et al. (2008)	×	×	×	–	×
2008.71	-0.216 ± 0.003	-0.582 ± 0.003	Marois et al. (2008)	×	×	–	–	×
2008.89	-0.217 ± 0.020	-0.608 ± 0.020	Currie et al. (2011)	×	–	–	–	×
2008.89	-0.215 ± 0.021	-0.644 ± 0.013	Hinz et al. (2010)	×	–	–	–	×
2009.70	-0.282 ± 0.030	-0.590 ± 0.030	Hinz et al. (2010)	×	–	–	–	×
2009.76	-0.270 ± 0.070	-0.600 ± 0.070	Bergfors et al. (2011)	×	–	–	–	×
2009.77	-0.241 ± 0.007	-0.586 ± 0.007	Currie et al. (2011)	×	–	–	×	×
2009.84	-0.240 ± 0.014	-0.580 ± 0.014	Galicher et al. (2011)	×	–	–	–	×
2010.83	-0.283 ± 0.005	-0.567 ± 0.005	Currie et al. (2012)	×	–	–	–	×
2011.79	-0.299 ± 0.010	-0.563 ± 0.010	Esposito et al. (2013)	×	–	–	–	×
2011.86	-0.320 ± 0.010	-0.549 ± 0.010	Esposito et al. (2013)	×	–	–	–	×

Table A4. Astrometric data in the literature for planet HR 8799 e ('s' stands for the arc second).

Epoch	Planet e		Reference	Data set				
	N (s)	E (s)		D1	D2	D3	D4	D5
2009.58	-0.299 ± 0.019	-0.217 ± 0.019	Marois et al. (2010)	×	–	–	–	–
2009.58	-0.303 ± 0.013	-0.209 ± 0.013	Marois et al. (2010)	×	–	–	–	–
2009.77	-0.306 ± 0.007	-0.217 ± 0.007	Currie et al. (2011)	×	–	–	×	–
2009.83	-0.304 ± 0.010	-0.196 ± 0.010	Marois et al. (2010)	×	–	–	–	–
2010.53	-0.324 ± 0.008	-0.174 ± 0.008	Marois et al. (2010)	×	–	–	–	–
2010.55	-0.324 ± 0.011	-0.175 ± 0.011	Marois et al. (2010)	×	–	–	–	–
2010.83	-0.312 ± 0.010	-0.151 ± 0.010	Marois et al. (2010)	×	–	–	–	–
2011.79	-0.326 ± 0.011	-0.119 ± 0.011	Esposito et al. (2013)	×	–	–	–	–
2011.86	-0.382 ± 0.011	-0.127 ± 0.011	Esposito et al. (2013)	×	–	–	–	–

APPENDIX B: EPHEMERIS OF THE FOUR- AND FIVE-PLANET MODELS

Table B1. Ephemeris of the best-fitting four-planet model IVa (1e:2d:4c:8b MMR) between epochs 1995.0 and 2020.0. Astrometric data in the [*E*, *N*]-plane ('s' stands for the arc second).

Epoch	Planet e		Planet d		Planet c		Planet b	
	$\Delta\alpha$ (s)	$\Delta\delta$ (s)	$\Delta\alpha$ (s)	$\Delta\delta$ (s)	$\Delta\alpha$ (s)	$\Delta\delta$ (s)	$\Delta\alpha$ (s)	$\Delta\delta$ (s)
1995	0.3598	− 0.0464	0.3055	−0.4425	−0.9031	0.3842	1.3624	1.0481
1996	0.3395	− 0.0931	0.2712	−0.4679	−0.8894	0.4101	1.3764	1.0308
1997	0.3123	− 0.1380	0.2356	−0.4909	−0.8748	0.4356	1.3901	1.0133
1998	0.2785	− 0.1801	0.1989	−0.5117	−0.8596	0.4608	1.4035	0.9956
1999	0.2385	− 0.2181	0.1613	−0.5301	−0.8436	0.4856	1.4166	0.9778
2000	0.1930	− 0.2512	0.1229	−0.5460	−0.8269	0.5100	1.4293	0.9597
2001	0.1430	− 0.2783	0.0840	−0.5596	−0.8094	0.5340	1.4418	0.9416
2002	0.0895	− 0.2988	0.0448	−0.5706	−0.7913	0.5576	1.4539	0.9233
2003	0.0338	− 0.3118	0.0053	−0.5793	−0.7725	0.5807	1.4657	0.9048
2004	− 0.0228	− 0.3172	− 0.0341	−0.5854	−0.7530	0.6034	1.4773	0.8863
2005	− 0.0788	− 0.3147	− 0.0735	−0.5892	−0.7329	0.6256	1.4886	0.8676
2006	− 0.1329	− 0.3045	− 0.1125	−0.5906	−0.7121	0.6473	1.4995	0.8488
2007	− 0.1838	− 0.2871	− 0.1511	−0.5896	−0.6906	0.6685	1.5102	0.8299
2008	− 0.2304	− 0.2630	− 0.1891	−0.5864	−0.6686	0.6892	1.5207	0.8108
2009	− 0.2718	− 0.2330	− 0.2264	−0.5809	−0.6459	0.7092	1.5308	0.7916
2010	− 0.3073	− 0.1980	− 0.2628	−0.5733	−0.6226	0.7287	1.5407	0.7723
2011	− 0.3366	− 0.1589	− 0.2983	−0.5636	−0.5987	0.7476	1.5504	0.7529
2012	− 0.3592	− 0.1168	− 0.3327	−0.5519	−0.5743	0.7659	1.5597	0.7334
2013	− 0.3751	− 0.0724	− 0.3659	−0.5383	−0.5494	0.7835	1.5688	0.7137
2014	− 0.3844	− 0.0268	− 0.3979	−0.5228	−0.5239	0.8005	1.5777	0.6939
2015	− 0.3871	0.0193	− 0.4284	−0.5056	−0.4979	0.8168	1.5862	0.6740
2016	− 0.3837	0.0651	− 0.4576	−0.4866	−0.4715	0.8324	1.5945	0.6539
2017	− 0.3743	0.1098	− 0.4852	−0.4661	−0.4446	0.8472	1.6026	0.6337
2018	− 0.3594	0.1530	− 0.5112	−0.4441	−0.4173	0.8614	1.6103	0.6134
2019	− 0.3393	0.1940	− 0.5356	−0.4207	−0.3896	0.8747	1.6178	0.5929
2020	− 0.3146	0.2323	− 0.5582	−0.3960	−0.3616	0.8874	1.6249	0.5723

Table B2. Ephemeris of the best-fitting five-planet model Va (1f:3e MMR). Epochs between 1995.0 and 2020.0. Astrometric coordinates in the [*E*, *N*]-plane ('s' stands for the arc second).

Epoch	Planet f		Planet e		Planet d		Planet c		Planet b	
	$\Delta\alpha$ (s)	$\Delta\delta$ (s)	$\Delta\alpha$ (s)	$\Delta\delta$ (s)	$\Delta\alpha$ (s)	$\Delta\delta$ (s)	$\Delta\alpha$ (s)	$\Delta\delta$ (s)	$\Delta\alpha$ (s)	$\Delta\delta$ (s)
1995	0.1595	− 0.0585	0.3625	− 0.0384	0.3076	−0.4439	−0.9050	0.3826	1.3646	1.0480
1996	0.1203	− 0.1197	0.3421	− 0.0857	0.2732	−0.4693	−0.8912	0.4083	1.3785	1.0305
1997	0.0625	− 0.1626	0.3148	− 0.1312	0.2373	−0.4925	−0.8767	0.4337	1.3920	1.0129
1998	− 0.0042	− 0.1829	0.2806	− 0.1739	0.2003	−0.5132	−0.8615	0.4589	1.4051	0.9951
1999	− 0.0703	− 0.1798	0.2402	− 0.2126	0.1624	−0.5316	−0.8456	0.4837	1.4179	0.9773
2000	− 0.1281	− 0.1551	0.1941	− 0.2463	0.1238	−0.5474	−0.8289	0.5083	1.4304	0.9595
2001	− 0.1709	− 0.1122	0.1434	− 0.2739	0.0847	−0.5608	−0.8114	0.5325	1.4427	0.9415
2002	− 0.1937	− 0.0563	0.0891	− 0.2946	0.0454	−0.5717	−0.7932	0.5564	1.4548	0.9234
2003	− 0.1931	0.0065	0.0325	− 0.3078	0.0059	−0.5801	−0.7742	0.5798	1.4667	0.9053
2004	− 0.1676	0.0683	− 0.0247	− 0.3131	− 0.0335	−0.5862	−0.7544	0.6027	1.4783	0.8869
2005	− 0.1185	0.1203	− 0.0813	− 0.3104	− 0.0727	−0.5898	−0.7339	0.6251	1.4898	0.8685
2006	− 0.0510	0.1534	− 0.1357	− 0.2998	− 0.1116	−0.5912	−0.7127	0.6470	1.5011	0.8498
2007	0.0251	0.1599	− 0.1867	− 0.2820	− 0.1499	−0.5903	−0.6908	0.6682	1.5121	0.8309
2008	0.0963	0.1361	− 0.2333	− 0.2575	− 0.1877	−0.5873	−0.6682	0.6888	1.5228	0.8117
2009	0.1485	0.0854	− 0.2746	− 0.2272	− 0.2249	−0.5822	−0.6452	0.7087	1.5331	0.7923
2010	0.1714	0.0179	− 0.3099	− 0.1919	− 0.2613	−0.5750	−0.6216	0.7280	1.5431	0.7727
2011	0.1626	− 0.0531	− 0.3389	− 0.1527	− 0.2969	−0.5658	−0.5976	0.7466	1.5527	0.7530
2012	0.1260	− 0.1153	− 0.3613	− 0.1105	− 0.3316	−0.5545	−0.5732	0.7647	1.5619	0.7332
2013	0.0701	− 0.1600	− 0.3771	− 0.0662	− 0.3651	−0.5413	−0.5483	0.7821	1.5708	0.7133
2014	0.0044	− 0.1827	− 0.3863	− 0.0206	− 0.3975	−0.5261	−0.5229	0.7990	1.5794	0.6934
2015	− 0.0619	− 0.1823	− 0.3890	0.0254	− 0.4285	−0.5091	−0.4971	0.8153	1.5877	0.6734
2016	− 0.1210	− 0.1600	− 0.3856	0.0711	− 0.4580	−0.4903	−0.4707	0.8309	1.5957	0.6534
2017	− 0.1659	− 0.1191	− 0.3764	0.1158	− 0.4859	−0.4698	−0.4439	0.8460	1.6035	0.6334
2018	− 0.1915	− 0.0643	− 0.3617	0.1589	− 0.5122	−0.4478	−0.4166	0.8603	1.6111	0.6132
2019	− 0.1939	− 0.0017	− 0.3420	0.1998	− 0.5368	−0.4244	−0.3888	0.8739	1.6185	0.5929
2020	− 0.1713	0.0610	− 0.3178	0.2381	− 0.5596	−0.3996	−0.3605	0.8868	1.6257	0.5726

Table B3. Ephemeris of best-fitting five-planet model Vb (1f:3e MMR) between epochs 1995.0 and 2020.0. Astrocentric coordinates in the [*E*, *N*]-plane ('s' stands for the arc second).

Epoch	Planet f		Planet e		Planet d		Planet c		Planet b	
	$\Delta\alpha$ (s)	$\Delta\delta$ (s)	$\Delta\alpha$ (s)	$\Delta\delta$ (s)	$\Delta\alpha$ (s)	$\Delta\delta$ (s)	$\Delta\alpha$ (s)	$\Delta\delta$ (s)	$\Delta\alpha$ (s)	$\Delta\delta$ (s)
1995	−0.1281	−0.1244	0.3684	0.0086	0.3078	−0.4348	−0.9060	0.3909	1.3609	1.0443
1996	−0.1616	−0.0642	0.3529	−0.0392	0.2733	−0.4601	−0.8920	0.4164	1.3749	1.0275
1997	−0.1645	0.0080	0.3303	−0.0861	0.2376	−0.4832	−0.8772	0.4417	1.3886	1.0105
1998	−0.1339	0.0784	0.3006	−0.1311	0.2009	−0.5040	−0.8615	0.4666	1.4021	0.9933
1999	−0.0754	0.1325	0.2638	−0.1731	0.1633	−0.5225	−0.8451	0.4910	1.4154	0.9759
2000	−0.0017	0.1604	0.2205	−0.2109	0.1251	−0.5388	−0.8279	0.5150	1.4285	0.9583
2001	0.0725	0.1595	0.1714	−0.2432	0.0863	−0.5528	−0.8100	0.5385	1.4412	0.9404
2002	0.1354	0.1333	0.1176	−0.2689	0.0470	−0.5644	−0.7915	0.5615	1.4536	0.9223
2003	0.1796	0.0884	0.0603	−0.2871	0.0076	−0.5738	−0.7724	0.5840	1.4656	0.9041
2004	0.2014	0.0323	0.0013	−0.2971	−0.0320	−0.5807	−0.7527	0.6060	1.4773	0.8856
2005	0.2000	−0.0275	−0.0579	−0.2986	−0.0715	−0.5854	−0.7324	0.6276	1.4886	0.8670
2006	0.1766	−0.0843	−0.1154	−0.2916	−0.1108	−0.5877	−0.7115	0.6487	1.4995	0.8483
2007	0.1340	−0.1320	−0.1699	−0.2767	−0.1497	−0.5877	−0.6901	0.6693	1.5101	0.8295
2008	0.0766	−0.1649	−0.2199	−0.2544	−0.1881	−0.5854	−0.6682	0.6894	1.5204	0.8106
2009	0.0101	−0.1782	−0.2644	−0.2258	−0.2258	−0.5809	−0.6456	0.7090	1.5304	0.7917
2010	−0.0575	−0.1683	−0.3028	−0.1919	−0.2627	−0.5742	−0.6225	0.7281	1.5401	0.7727
2011	−0.1166	−0.1337	−0.3345	−0.1537	−0.2986	−0.5655	−0.5988	0.7468	1.5496	0.7537
2012	−0.1560	−0.0769	−0.3592	−0.1123	−0.3334	−0.5547	−0.5745	0.7649	1.5589	0.7346
2013	−0.1660	−0.0058	−0.3771	−0.0687	−0.3670	−0.5420	−0.5496	0.7824	1.5680	0.7154
2014	−0.1422	0.0662	−0.3881	−0.0239	−0.3993	−0.5274	−0.5241	0.7992	1.5769	0.6961
2015	−0.0889	0.1246	−0.3927	0.0212	−0.4301	−0.5113	−0.4980	0.8154	1.5856	0.6766
2016	−0.0178	0.1583	−0.3912	0.0660	−0.4595	−0.4935	−0.4715	0.8308	1.5942	0.6569
2017	0.0567	0.1637	−0.3840	0.1097	−0.4874	−0.4743	−0.4445	0.8454	1.6024	0.6370
2018	0.1225	0.1431	−0.3715	0.1519	−0.5138	−0.4537	−0.4171	0.8593	1.6103	0.6169
2019	0.1713	0.1023	−0.3543	0.1920	−0.5387	−0.4318	−0.3894	0.8724	1.6179	0.5965
2020	0.1986	0.0486	−0.3328	0.2298	−0.5620	−0.4086	−0.3614	0.8846	1.6251	0.5761

Table B4. Ephemeris for the best-fitting five-planet model Vc (1e:2f MMR) between epochs 1995.0 and 2020.0. Astrocentric coordinates in the [*E*, *N*]-plane ('s' stands for the arc second).

Epoch	Planet f		Planet e		Planet d		Planet c		Planet b	
	$\Delta\alpha$ (s)	$\Delta\delta$ (s)	$\Delta\alpha$ (s)	$\Delta\delta$ (s)	$\Delta\alpha$ (s)	$\Delta\delta$ (s)	$\Delta\alpha$ (s)	$\Delta\delta$ (s)	$\Delta\alpha$ (s)	$\Delta\delta$ (s)
1995	0.0211	0.2113	0.3653	0.0044	0.3072	−0.4169	−0.9002	0.3883	1.3692	1.0467
1996	0.0856	0.2149	0.3483	−0.0436	0.2732	−0.4439	−0.8862	0.4139	1.3828	1.0296
1997	0.1442	0.2034	0.3242	−0.0907	0.2379	−0.4688	−0.8716	0.4390	1.3961	1.0123
1998	0.1942	0.1795	0.2931	−0.1358	0.2013	−0.4913	−0.8562	0.4639	1.4091	0.9948
1999	0.2337	0.1461	0.2552	−0.1778	0.1637	−0.5115	−0.8402	0.4883	1.4217	0.9771
2000	0.2621	0.1056	0.2109	−0.2154	0.1253	−0.5293	−0.8236	0.5123	1.4340	0.9592
2001	0.2788	0.0603	0.1610	−0.2474	0.0864	−0.5447	−0.8063	0.5360	1.4460	0.9412
2002	0.2838	0.0126	0.1068	−0.2727	0.0470	−0.5576	−0.7883	0.5592	1.4577	0.9230
2003	0.2774	−0.0357	0.0496	−0.2904	0.0074	−0.5681	−0.7698	0.5820	1.4690	0.9046
2004	0.2599	−0.0825	−0.0091	−0.2997	−0.0322	−0.5761	−0.7506	0.6044	1.4801	0.8862
2005	0.2319	−0.1260	−0.0675	−0.3006	−0.0717	−0.5818	−0.7308	0.6263	1.4908	0.8676
2006	0.1941	−0.1642	−0.1241	−0.2931	−0.1109	−0.5850	−0.7104	0.6478	1.5012	0.8488
2007	0.1478	−0.1952	−0.1773	−0.2777	−0.1497	−0.5859	−0.6895	0.6688	1.5113	0.8300
2008	0.0945	−0.2167	−0.2258	−0.2550	−0.1879	−0.5845	−0.6680	0.6893	1.5212	0.8111
2009	0.0361	−0.2266	−0.2689	−0.2261	−0.2254	−0.5809	−0.6459	0.7093	1.5307	0.7920
2010	−0.0244	−0.2229	−0.3058	−0.1920	−0.2621	−0.5752	−0.6232	0.7287	1.5400	0.7728
2011	−0.0831	−0.2036	−0.3360	−0.1538	−0.2979	−0.5673	−0.6001	0.7477	1.5490	0.7536
2012	−0.1350	−0.1677	−0.3596	−0.1124	−0.3325	−0.5574	−0.5763	0.7660	1.5578	0.7342
2013	−0.1739	−0.1160	−0.3764	−0.0690	−0.3660	−0.5456	−0.5521	0.7838	1.5663	0.7147
2014	−0.1939	−0.0518	−0.3867	−0.0244	−0.3982	−0.5320	−0.5274	0.8010	1.5745	0.6951
2015	−0.1907	0.0186	−0.3907	0.0206	−0.4291	−0.5166	−0.5022	0.8176	1.5826	0.6754
2016	−0.1641	0.0866	−0.3888	0.0654	−0.4585	−0.4995	−0.4765	0.8335	1.5903	0.6556
2017	−0.1180	0.1445	−0.3813	0.1092	−0.4864	−0.4809	−0.4503	0.8487	1.5978	0.6356
2018	−0.0591	0.1869	−0.3688	0.1515	−0.5128	−0.4609	−0.4238	0.8632	1.6051	0.6155
2019	0.0055	0.2118	−0.3515	0.1919	−0.5376	−0.4394	−0.3968	0.8770	1.6121	0.5952
2020	0.0698	0.2197	−0.3300	0.2300	−0.5608	−0.4167	−0.3696	0.8900	1.6187	0.5747

Table B5. Ephemeris of the best-fitting five-planet model Vd (1f:2e MMR) between epochs 1995.0 and 2020.0. Astrometric coordinates in the [*E*, *N*]-plane ('s' stands for the arc second).

Epoch	Planet f		Planet e		Planet d		Planet c		Planet b	
	$\Delta\alpha$ (s)	$\Delta\delta$ (s)	$\Delta\alpha$ (s)	$\Delta\delta$ (s)	$\Delta\alpha$ (s)	$\Delta\delta$ (s)	$\Delta\alpha$ (s)	$\Delta\delta$ (s)	$\Delta\alpha$ (s)	$\Delta\delta$ (s)
1995	0.1761	− 0.0811	0.3686	0.0002	0.3100	−0.4290	−0.9033	0.3851	1.3574	1.0459
1996	0.1356	− 0.1404	0.3528	− 0.0480	0.2757	−0.4554	−0.8895	0.4109	1.3714	1.0285
1997	0.0812	− 0.1856	0.3297	− 0.0952	0.2399	−0.4795	−0.8750	0.4364	1.3851	1.0110
1998	0.0196	− 0.2145	0.2996	− 0.1404	0.2030	−0.5013	−0.8598	0.4615	1.3984	0.9933
1999	− 0.0436	− 0.2269	0.2625	− 0.1823	0.1650	−0.5205	−0.8438	0.4863	1.4115	0.9755
2000	− 0.1040	− 0.2243	0.2190	− 0.2197	0.1263	−0.5373	−0.8271	0.5108	1.4242	0.9575
2001	− 0.1583	− 0.2085	0.1700	− 0.2515	0.0870	−0.5516	−0.8096	0.5348	1.4367	0.9395
2002	− 0.2044	− 0.1817	0.1164	− 0.2767	0.0474	−0.5634	−0.7915	0.5584	1.4488	0.9212
2003	− 0.2406	− 0.1461	0.0596	− 0.2942	0.0075	−0.5727	−0.7727	0.5817	1.4607	0.9029
2004	− 0.2660	− 0.1039	0.0012	− 0.3036	− 0.0323	−0.5795	−0.7531	0.6044	1.4724	0.8845
2005	− 0.2798	− 0.0573	− 0.0572	− 0.3045	− 0.0720	−0.5838	−0.7329	0.6267	1.4837	0.8659
2006	− 0.2818	− 0.0081	− 0.1141	− 0.2971	− 0.1114	−0.5858	−0.7120	0.6485	1.4948	0.8472
2007	− 0.2718	0.0414	− 0.1678	− 0.2816	− 0.1503	−0.5854	−0.6904	0.6697	1.5057	0.8283
2008	− 0.2499	0.0891	− 0.2172	− 0.2589	− 0.1885	−0.5827	−0.6682	0.6905	1.5163	0.8094
2009	− 0.2166	0.1327	− 0.2612	− 0.2298	− 0.2260	−0.5778	−0.6453	0.7106	1.5267	0.7903
2010	− 0.1727	0.1697	− 0.2991	− 0.1953	− 0.2627	−0.5708	−0.6218	0.7301	1.5368	0.7710
2011	− 0.1195	0.1976	− 0.3303	− 0.1566	− 0.2983	−0.5617	−0.5977	0.7490	1.5466	0.7516
2012	− 0.0591	0.2136	− 0.3547	− 0.1146	− 0.3329	−0.5506	−0.5731	0.7672	1.5562	0.7320
2013	0.0052	0.2150	− 0.3722	− 0.0705	− 0.3663	−0.5377	−0.5479	0.7848	1.5656	0.7122
2014	0.0689	0.1994	− 0.3830	− 0.0251	− 0.3984	−0.5229	−0.5223	0.8016	1.5746	0.6923
2015	0.1263	0.1658	− 0.3872	0.0207	− 0.4291	−0.5064	−0.4961	0.8177	1.5834	0.6722
2016	0.1706	0.1152	− 0.3853	0.0662	− 0.4585	−0.4884	−0.4696	0.8331	1.5918	0.6519
2017	0.1955	0.0516	− 0.3775	0.1106	− 0.4864	−0.4687	−0.4426	0.8477	1.5999	0.6314
2018	0.1972	− 0.0181	− 0.3644	0.1534	− 0.5128	−0.4476	−0.4153	0.8616	1.6077	0.6108
2019	0.1759	− 0.0858	− 0.3464	0.1941	− 0.5376	−0.4251	−0.3877	0.8747	1.6151	0.5901
2020	0.1353	− 0.1442	− 0.3239	0.2323	− 0.5608	−0.4012	−0.3598	0.8871	1.6222	0.5693

This paper has been typeset from a TEX/LATEX file prepared by the author.